Space-time resolved measurements for water waves: time-reversal and wave turbulence.

Adam Przadka

THÈSE DE DOCTORAT
DE L'UNIVERSITÉ PIERRE ET MARIE CURIE

DYNAMIQUE DES FLUIDES ET DES TRANSFERTS

ÉCOLE DOCTORALE 391
Sciences mécaniques, acoustique, électronique & robotique de Paris

Adam PRZĄDKA

MESURES SPATIO-TEMPORELLES D'ONDES À LA SURFACE DE L' EAU : RETOURNEMENT TEMPOREL ET TURBULENCE D'ONDE

SPACE-TIME RESOLVED MEASUREMENTS FOR WATER WAVES:
TIME-REVERSAL AND WAVE TURBULENCE

Thèse dirigée par Agnès MAUREL, Vincent PAGNEUX & Philippe PETITJEANS
Soutenue le 28 septembre 2012

JURY

M. Michel Benoit	Rapporteur
M. Sébastien Guenneau	Rapporteur
M. Christophe Josserand	
M. Jacek Rokicki	
M. Frédéric Moisy	
Mme Agnès Maurel	Co-Directrice de Thèse
M. Vincent Pagneux	Co-Directeur de Thèse
M. Philippe Petitjeans	Directeur de Thèse

Résumé

**Mesures spatio-temporelles d'ondes à la surface de l'eau :
retournement temporel et turbulence d'onde.**

Cette thèse porte sur l'étude expérimentale des ondes à la surface de l'eau et se concentre sur deux sujets : valider la focalisation des ondes de surface par retournement temporel et caractériser la turbulence d'onde par analyse des spectres spatio-temporels.

La problématique commune était la mesure de la déformation de la surface libre. Avec la technique de Profilométrie par Transformée de Fourier utilisée jusqu'à present, la coloration de l'eau par de la peinture usuelle a pour conséquence une atténuation des ondes par résonance d'ondes de films de surface. Une amélioration importante de la méthode permet une analyse fiable des phénomènes d'ondes en surmontant l'effet d'amortissement.

Ce travail apporte ensuite la première preuve expérimentale de focalisation par retournement temporel des ondes de surface. Un unique canal de retournement temporel a suffi pour reconstruire l'onde à sa source initiale dans une cavité. Il a été démontré que la qualité de la focalisation augmente linéairement avec le nombre de canaux de réémission. Une autre partie de cette thèse concerne des expériences de turbulence d'onde effectuées pour deux bandes de fréquence de forçage avec différentes intensités d'onde. Selon la bande de forçage, deux régimes différents ont été observés. La pente de cascade d'énergie s'est révélée être dépendante du forçage, comme observé précédemment, ou indépendante. Dans ce dernier cas, les résultats sont en accord avec la théorie. La thèse traite également de la bathymétrie. En utilisant la "méthode du cercle" cette étude a permis de déterminer la profondeur d'eau par ajustement de la fonction de Bessel appropriée aux données expérimentales.

Les mots clés : ondes de surface, ondes de gravité-capillarité, retournement temporel, turbulence d'onde, bathymétrie, études expérimentales, Profilométrie par Transformée de Fourier.

Cette thèse a été préparée dans le
Laboratoire de Physique et Mécanique des Milieux Hétérogènes (PMMH)
UMR CNRS 7636 - ESPCI - UPMC Univ. Paris 6 - UPD Univ. Paris 7
10, rue Vauquelin
75005 Paris, France

Résumé substantiel

**Mesures spatio-temporelles d'ondes à la surface de l'eau :
retournement temporel et turbulence d'onde.**

Cette thèse porte sur l'étude expérimentale des ondes à la surface de l'eau. Elle comporte un volet «technique» relatif à la technique de mesure résolue en temps et en espace (FTP), qui a consisté à l'identification de particules diffusantes capables de reproduire la même -faible- atténuation que l'eau pure (une étape essentielle pour assurer un long temps de propagation des ondes) et un volet d'étude de problèmes physiques concernant la propagation des ondes à la surface de l'eau en milieux complexes : validation de la focalisation des ondes de surface par retournement temporel, caractérisation de la turbulence d'onde par analyse des spectres spatio-temporels et reconstruction d'une bathymétrie variable par analyse de la propagation d'onde en surface.

Le volet technique de cette thèse est lié à la mesure de la déformation de la surface libre obtenue avec la technique de Profilométrie par Transformée de Fourier (FTP). Cette technique optique s'appuie sur l'analyse de la déformation d'un réseau de franges projetées sur la surface libre d'un liquide. On entend par déformation du réseau la différence entre le réseau déformé par la surface non plane et le réseau de référence sur la surface plane. Cette méthode expérimentale nécessite que la lumière soit diffusée par la surface du liquide, ce qui était obtenu habituellement par addition de pigments blancs. Pendant ma thèse, j'ai montré que la coloration de l'eau par de la peinture usuelle (utilisée jusqu'à présent) produit une forte augmentation de l'atténuation des ondes. En effet, ces peintures contiennent des tensioactifs qui sont facilement adsorbées à l'interface air-eau. Le film de surface résultant modifie les propriétés d'atténuation, à cause de la modification de la tension de surface mais aussi et surtout en raison de l'amortissement due à la résonance des ondes de gravité-capillarité et des ondes de Marangoni. Cette atténuation a été confirmée et caractérisée expérimentalement. Dans un deuxième temps, j'ai réalisé une étude sur les propriétés physico-chimiques de différents pigments, montrant que les particules d'anatase (TiO_2) sont les meilleurs pigments, au sens d'un compromis entre la diffusion qu'ils produisent et la réduction des effets de film de surface. J'ai ainsi montré que ces particules permettent d'obtenir les mêmes propriétés d'atténuation que l'eau pure. Ce développement était nécessaire pour nos expériences menées à l'échelle du laboratoire, notamment en turbulence d'onde et en retournement temporel des ondes à la surface de l'eau. En effet, pour des applications potentielles aux ondes à l'échelle de l'océan, où on sait que l'atténuation est faible, il est crucial de reproduire autant que faire se peut les mêmes conditions de faibles atténuations (c'est-à-dire de long temps de vie de l'onde) que dans l'océan. Ce travail a donné lieu à une publication dans Experiments in Fluids (52(2):519-527, 2012)

Cette étape un peu «technique» étant résolue, je me suis intéressé à trois problèmes concernant les ondes en régime temporel dans un contexte de propagation complexe : le retournement temporel d'ondes à la surface de l'eau, la turbulence d'ondes et plus récemment, la reconstruction de la bathymétrie par analyse des ondes à la surface de l'eau.

Retournement temporel d'ondes à la surface de l'eau : Le retournement temporel s'appuie sur l'invariance de l'équation d'onde par la transformation $t \rightarrow -t$. Ainsi, si on renvoie dans une chronologie inversée les ondes émises par un point source, on s'attend à voir ces ondes retournées temporellement refocaliser - spatialement et temporellement - sur le point d'origine. Si des expériences dans différents contextes d'ondes ont été réalisé dans le passé, il n'y avait jusqu'à aujourd'hui pas de preuve expérimentale de la possibilité de refocaliser des ondes à la surface de l'eau. Ceci était principalement due à la complexité de ces ondes qui sont dispersives, non-linéaires et surtout dissipatives. Les expériences ont été menées dans une cavité pour tirer parti des réflexions multiples sur les bords. Dans une première étape, l'onde émise par une source ponctuelle est enregistrée par FTP. Dans une deuxième étape, les signaux enregistrés en certains points de réception (de 1 point à 6 points) sont renversés temporellement et reémis dans la cavité. Comme attendue dans la théorie et malgré les écarts à cette théorie (dispersion, atténuation, non linéarité), on observe une bonne recompression / refocalisation avec un point de reémission, et la qualité de cette recompression / recfocalisation augmente linéairement avec le nombre de points de reémission. J'ai également vérifié que le rapport signal à bruit, qui mesure quantitativement la qualité de recompression / refocalisation est lié directement aux nombres de modes excités dans la cavité. Ce nombre de modes est limité dans l'expérience à cause de la forte atténuation aux basses et hautes fréquences, ce qui a été vérifié par comparaison avec un calcul numérique. Ainsi, à l'échelle du laboratoire, c'est-à-dire avec des longueurs d'onde centimétriques, la qualité de la refocalisation est limitée par l'atténuation, mais elle n'est pas supprimée. Des simulations numériques correspondant à des ondes à plus grande échelle avec une atténuation négligeable, comme on l'attend à l'échelle océanique, montre une recompression / refocalisation plus efficace, ce qui est très encourageant pour les applications à l'échelle océanique. Ce travail a donné à une publication dans Physical Review Letters (109, 064501 (2012)).

Turbulence d'onde à la surface de l'eau : A la suite des travaux de mon groupe sur l'application de la FTP pour la caractérisation en temps et en espace des déformations de plaques (collaboration avec N. Mordant à l'ENS), je me suis intéressé à la caractérisation spatio-temporelle des ondes à la surface de l'eau en régime turbulent. Nous avons ainsi montré deux résultats importants. Par double transformée de Fourier (en espace et en temps) nous avons vérifié deux hypothèses importantes utilisées dans la théorie de Weak Turbulence (WT) : les ondes sont réparties de façon isotrope, c'est -à-dire que l'énergie des fluctuations ne dépend pas de la direction du vecteur d'onde, également l'énergie se répartit à travers les échelles, c'est-à-dire la norme du vecteur d'onde et la fréquence, sur une courbe proche de la relation de dispersion. Par ailleurs, nous avons obtenu un résultat nouveau en réalisant plusieurs expéri-

ences à bande de fréquences variables. Lorsque la bande de fréquences d'excitation est large (avec une référence que nous n'avons pas encore compris, dans nos expérience [0;4] Hz), nous confirmons les résultats obtenus par d'autres groupes expérimentaux et en contradiction avec les prédictions théoriques, à savoir : l'exposant spectral (pente de la courbe énergie - nombre d'onde en loglog) dépend de la puissance injectée et la loi de puissance n'est pas en accord avec la théorie WT. En revanche, pour une bande d'excitation plus faible (dans nos expériences, [0;1.5] Hz), nous observons une pente spectrale constante en fonction de la puissance injectée et en accord avec la théorie WT, par ailleurs, la dépendance en fonction de la puissance semble en accord avec la WT (ce résultat, moins net que le premier, reste cependant à confirmer). Les résultats de ces premières expériences ont donné lieu à une publication dans Physical Review Letters (107:214503, 2011) et une publication du groupe dans Acta Physica Polonica (120:142-148, 2011) et je présente dans mon mémoire de thèse les résultats d'expériences nouvelles que j'ai réalisées de façon systématique (plus grande variabilité de la bande de fréquence) et dont l'analyse est en cours.

La reconstruction de la bathymétrie par analyse des ondes à la surface de l'eau : Cette étude réalisée en collaboration avec R.K. Ing concerne la possibilité de reconstruire la bathymétrie (profondeur variable typiquement due à la présence d'obstacles sous-marins), par analyse de la forme d'ondes se propageant à la surface de l'eau. La méthode utilise l'ajustement de la fonction de Bessel (attendue pour la dépendance spatiale des ondes) aux données expérimentales mesurées en surface sur une large bande de fréquences (le signal analysé correspond à un paquet d'onde se propageant dans un milieu complexe). Notre étude a permis de quantifier les limitations de cette méthode pour des obstacles profonds (limite des ondes en eau peu profonde) dans le cas des ondes à la surface de l'eau. Un article est en cours de rédaction sur ce sujet.

Abstract

**Space-time resolved measurements for water waves:
time-reversal and wave turbulence.**

This thesis presents an experimental investigation on water waves and concentrates on two current challenges. The first, to validate the time-reversal focusing of surface waves, and the second, to characterize the wave turbulence by joint space-time energy spectra analysis.

The common requirement for each study was the measurement of free-surface deformation. Quantitative data was gathered by Fourier Transform Profilometry. Resonance-type wave damping is shown to be present while using this method with water colored by standard paint. A proper investigation of the wave phenomena is enabled by a crucial improvement to this technique which overcomes the damping effect.

This work provides the first experimental evidence of time-reversal focusing of surface waves. One time-reversal channel was sufficient to reconstruct the wave at the point source in a reverberating cavity. It is also demonstrated that the quality of the refocusing increases linearly with the number of re-emitting channels. This thesis also concerns wave turbulence experiments performed for two forcing frequency ranges with varying wave intensity. Depending on the forcing bandwidth two different regimes were observed. The energy cascade slope was found to be both forcing dependent, as classically observed in laboratory experiments, or forcing independent. In the latter case, the results are in agreement with the theory. The remainder of the thesis focuses on bathymetry. The feasibility of underwater depth reconstruction, by fitting an appropriate Bessel function to the experimental data, is demonstrated using a "circle method".

Key words: surface waves, gravity-capillary waves, time-reversal, wave turbulence, bathymetry, experimental investigations, Fourier Transform Profilometry.

This thesis has been prepared in the
Laboratory of Physics and Mechanics of Heterogeneous Media (PMMH)
UMR CNRS 7636 - ESPCI - UPMC Univ. Paris 6 - UPD Univ. Paris 7
10, rue Vauquelin
75005 Paris, France

CONTENTS

CHAPTER 1

INTRODUCTION

1.1 Motivation

Free-surface waves represent a natural interface between fluid dynamics and wave science and occur in many aspects in everyday life. Due to their industrial applications, they have been of interest for decades for coastal engineers, oceanographers and naval architects. In addition to the engineering communities, a broad society of physicists has been attracted by the wealth of physical phenomena displayed by gravity-capillary surface waves. Such as, they continue to be a fertile field of research today.

In the last fifty years, significant progress has been made in the field of free-surface wave science. Modern scientists have access to the powerful equipment that allows precise measurements. It is, then, very surprising that some theoretical phenomena still remain unsubstantiated by the experimental quantitative or even qualitative results.

Despite the common character of various wave phenomena, water waves reflect properties that can be rarely matched by other kinds of waves. First, they can give a conspicuous display of the nonlinear effects (which is revealed for enough steep waves). In addition, the intrinsic dispersion makes their velocity varies with the wavelength. Moreover, the phase velocity differs from the group velocity and is also dependent on the water depth. Finally, short waves experience strong damping due to the viscous action. Despite the fact that water waves are ubiquitous and easily observable, all these complexities make them one of the most difficult examples of waves to study theoretically, experimentally and numerically.

For instance, the spectacular manifestation of the interactions between dispersion and nonlinear effects has been described by John Scott Russell. He found out that the effect of weak nonlinearity (due to the moderately steep waves propagating in the shallow water) can

be balanced by the dispersion effect. As a result, permanent shape and propagation velocity is kept (no wave focusing, no wave separation).

In the case of deep water, nonlinear evolution of the wave group can result in an appearance of steep waves (called freak or rogue waves). These waves have a huge potential for damage, and thus are interesting for engineers, as well as physicists. They are sporadically present in the open sea/ocean and in the extreme case can eventually lead to a destruction of a ship or construction. Zakharov, in 1968, described that the evolution of the nonlinear wave group can be approximately satisfied by nonlinear Schrödinger equation. This evolution can lead to the creation of steep waves. The huge waves formation has been obtained numerically and experimentally as a result of dispersive wave grouping due to an appropriate phase modulation of initial wave trains. Despite that fact, the exact formation mechanism of the spontaneous rogue wave formation in nature is still not known. Their evolution is not precisely described by any theoretical model, which makes it impossible to numerically study the apparition and physics of rogue waves. In this sense, the experimental investigations of the freak wave phenomenon could shed some light into fundamental aspects of its formation.

The occurrence of wave focusing has been extensively studied in other fields of wave physics. Recent efforts concentrate on a unique phenomenon associated with wave physics - refocusing back the energy of the wave to its initial source point. It can be accomplished due to the time-reversal invariance of the wave equation. Indeed, the wave equation in a non-dissipative medium contains only a second-order time-derivative operator. It indicates that if the wave converging from the source is a solution to the problem, then the diverging wave propagating in the reverse direction and undertaking the same scattering, reflections and refraction is also a solution to that problem. It constitutes the principle of time-reversal phenomenon and is one of the most striking and important results in recent wave science. The wave time-reversal is related to the freak waves because of the amplitude focusing they undergo, however, the underlying physics differs significantly.

In the standard time-reversal experiments, a wave is generated at the source and recorded on a surrounding surface. This signal is time reversed and re-emitted to the system. It propagates back through the same medium as though the wave was being played backwards and focuses on the source. It was later observed that if the system is closed in a chaotic cavity, only a single source/receiver is required to focus back energy on the initial source. The time-reversal phenomenon was originally found for ultrasounds in the 1990s, and has been recently extended to microwaves, electromagnetism and elastic waves. Despite the considerable advances of time-reversal applications in almost all wave science domains, it has never been validated experimentally for water waves, perhaps due to the complexities the water waves display. Moreover, it has never been tested for any strongly damped nor naturally dispersive waves. An experimental study on time-reversal water waves could give an insight into the influence of these complexities on time-reversal phenomenon.

As it was stated, nonlinear effects can have important influence in the wave phenomena. Among others, the nonlinear mutual interactions between surface waves are of particular importance for the scientific communities and has enjoyed unceasing interest in the last

decades.

If a system allows nonlinear interactions (weaker than the linear ones) it possesses a natural asymptotic closure and can be solved mathematically. This state of nonlinear out-of-equilibrium wave process is called wave turbulence. The power of wave turbulence comes from the fact that the analytical solution of the kinetic equation, by which it is described, leads to the familiar solution with fully developed turbulence; the power law scaling of the energy density spectrum predicted by Kolmogorov. It predicts that the energy is transfered through different wavelengths from the injection scale to the scale where it is dissipated. The most common example is that of ocean surface wave stirred by the wind or generated by the current, but, in principle, it is present in a various wave aspects, such as music of vibrations on elastic sheets, Alfvén waves in solar winds or waves in nonlinear optics.

At a fundamental level, the study of this interdisciplinary subject aims at understanding the underlying physics of the energy cascade. Though, since its conception in 1960s, there have been many notable theoretical developments, there are still some limitations. Furthermore, few experimental measurements have been performed and they reveal some inconsistencies with the developed theory. In addition, the laboratory experiments are mainly local in space, while the theory predictions concern Fourier space.

In the case of surface waves, the only experimental study in a 3D Fourier space (x,y,t) did not confirm the premise of weak turbulence - the distribution of the energy was found to be concentrated not only on the vicinity of the linear dispersion relation. In this context, further space-time measurements are necessary to better understand the fundamental processes of wave turbulence.

The investigations of wave turbulence on the ocean are also encouraging in the case of renewable energy. In recent wave turbulence experiments, the negative energy flux has been observed, however, current weak turbulence theory does not support energy flux fluctuations. The nonlinear wave interactions can lead also to high-amplitude wave-induced motion of submerged bodies. These phenomena could give a possibility to extract energy from ocean waves, thus the wave turbulence should be further studied in terms of alternative energy harnessing.

The study of free-surface deformation can be also attractive since it can reveal the informations about subsurface field. Surfaces can deform due to the interactions with vortices or jets or rising bubbles. It is interesting to understand how the phenomena in the bulk are reflected on the surface. Water depth, amongst other informations encrypted in the surface deformation, can have particularly practical application. For sufficiently shallow water, the propagating wave "feels" the bottom and consequently changes its form (wavelength and height). The regions with shallow water are extremely important for engineers concerned with coastal problems, such as maintenance of navigation routes, port and harbor constructions or dredging. Surprisingly, data collection in shallow water areas by recent industrial solutions is expensive and sometimes extremely difficult, therefore, the study of water depth by free-surface deformation analysis might constitute an alternative to current methods.

In the light of all these challenges, a crucial issue emerges - the appropriate methodology for free-surface measurement. Most of the previous experiments were limited to the analysis of a single point. This method does not supply enough information to progress the understanding of discussed subjects. Advanced research in the laboratory scale requires a technique that allows one to reconstruct, non-intrusively, the 3D surface deformation with high space and time resolution. A Fourier Transform Profilometry (FTP) method corresponds to our needs and was recently adapted for surface waves. Here, a fringe pattern of known characteristic is projected onto the surface. The deformed surface introduces the modulation in the pattern. The topography of the surface is deduced from the phase difference of that recorded pattern between undeformed and deformed surface. Despite the indisputable advantages of this method, it requires the use of the white pigments, which were found to change the physico-chemical properties of water giving rise to the strong damping enhancement. This significantly reduces the possibility of the study of open problems raised above. In that context, the first objective of my thesis was to overcome these limitations and to propose an improvement to the measuring technique.

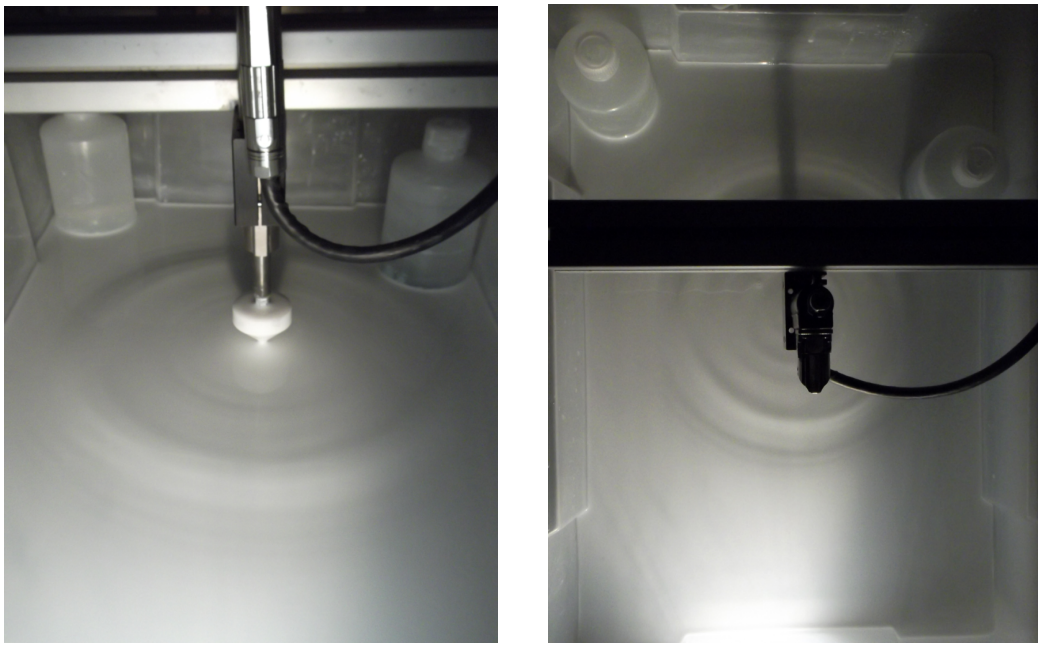

Figure 1.1: Photographs of the free surface deformation short after a pulse injection by the conical wavemaker. The cylindrical wave is diverging from the source. The size of the rectangular tank is 53 x 38 cm^2. Obstacles are placed to break the symmetry. This kind of signal was used in the time-reversal experiments.

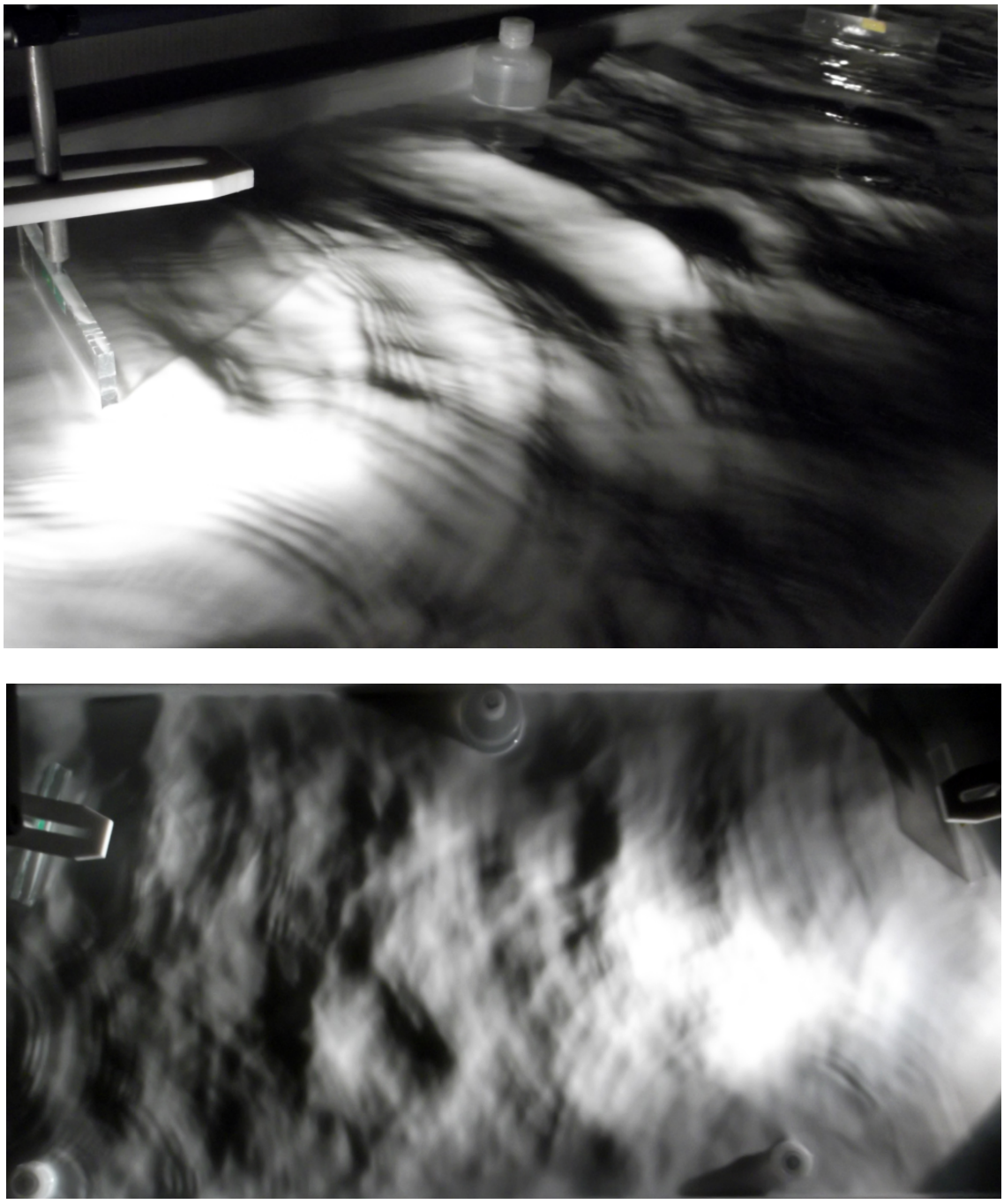

Figure 1.2: Visualization of the free surface deformation during the experiment of the mutual wave-wave interactions. Two piston-type wavemakers are used to inject energy to the system. Observed wavefield is typical for high forcing amplitude experiments. Strong lighting helps the naked eye to distinguish different wavelengths.

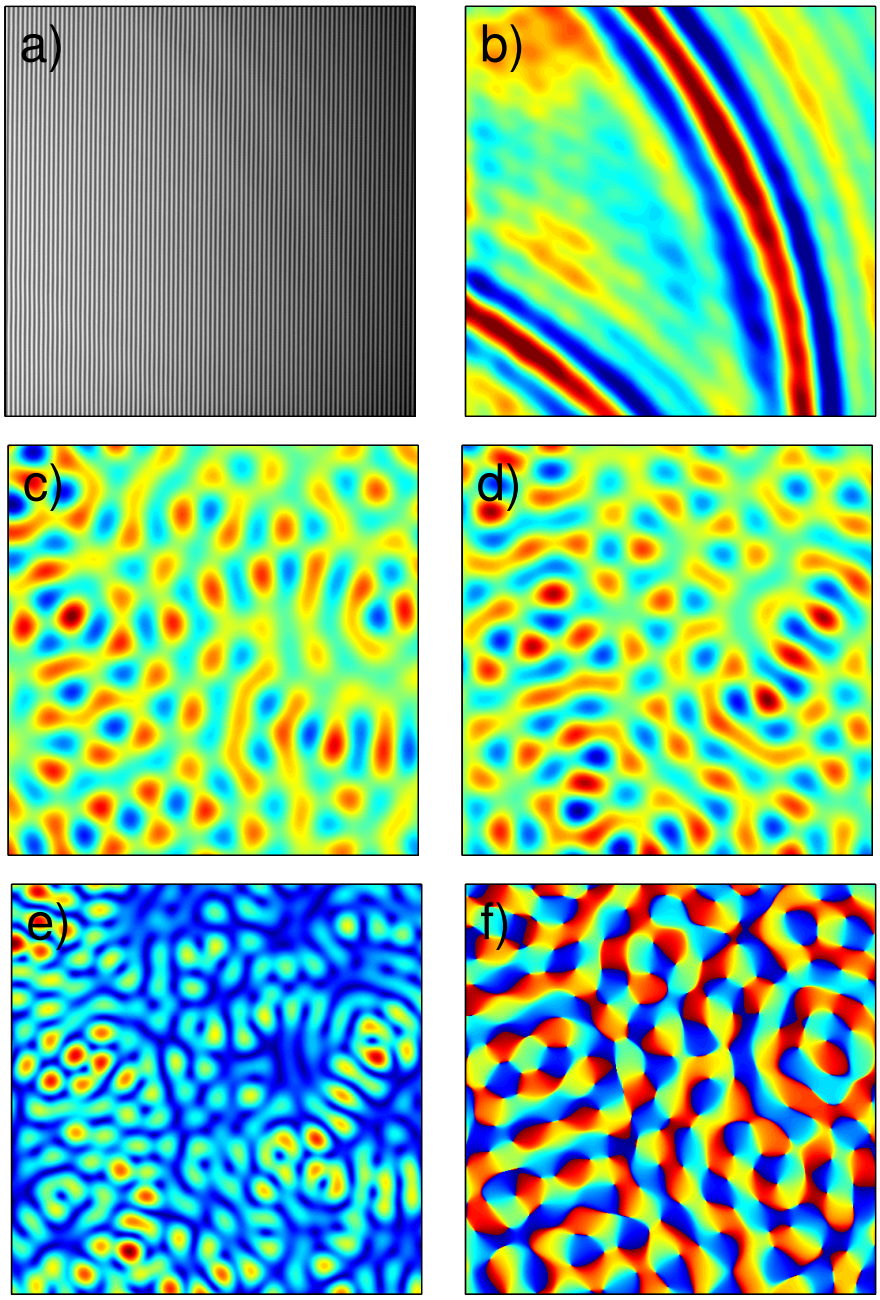

Figure 1.3: A typical fringe pattern recorded by the camera (a) and a corresponding surface elevation (b). Space-time resolved technique gives access to the complex fields obtained by time Fourier transform of the measured transient height. Typical real (c) and imaginary (d) values of the complex field for frequency $f = 8$ Hz are presented. Corresponding absolute and phase values are shown in (e) and (f). All figures are taken from the same data. Physical size of the images is 30 x 30 cm^2 and crest to trough wave height in the image (b) reaches 0.4 mm.

1.2 Linear wave theory

The linear theory of gravity-capillary waves on water will be given in this section. This theory is often called Airy wave theory thanks to the scientist George Biddell Airy who was first to derive, in 1841, the correct mathematical formula describing surface waves. Many monographs and books on wave theory has been written since that time presenting slightly different approaches to the problem. The presented derivation for perfect fluid is based on the one proposed by Lighthill [48].

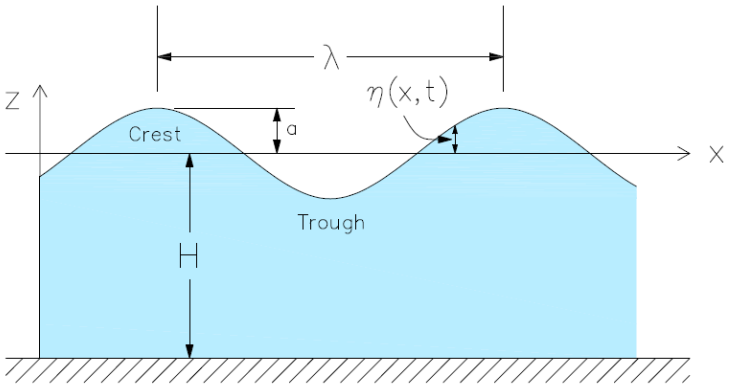

Figure 1.4: Schematic illustration of the system.

In most of the phenomena in nature (as it is also in our case) the compressibility of water can be neglected (constant water density ρ), thus the continuity equation takes a form: $\nabla \cdot \mathbf{u} = 0$, where $\mathbf{u}$ stands for a velocity with components $[u, v, w]$ which correspond to $[x, y, z]$ directions, where z is a direction perpendicular to the water surface measured upwards (Fig. 1.4).

Considering the irrotationality of velocity field, the velocity can be expressed as a gradient of the velocity potential ϕ, therefore the continuity equation reduces to Laplace's equation:

$$\nabla^2 \phi = 0 \tag{1.1}$$

The linearized momentum equation for inviscid fluid can be written as:

$$\rho \frac{\partial \mathbf{u}}{\partial t} = -\nabla p_e, \tag{1.2}$$

where p_e denotes excess pressure. With the hydrostatically distributed undisturbed pressure $p_0 = p_a - \rho g z$, where p_a is an atmospheric pressure, the excess pressure due to a disturbance can be defined as:

$$p_e = p - p_0 \tag{1.3}$$

Then, due to the action of gravity g, the excess pressure on the water surface $z = \eta(x, y, t)$ reaches:

$$p_e = \rho g \eta \tag{1.4}$$

The linearized momentum eq. (1.2) can be associated with the excess pressure field by:

$$p_e = -\rho \frac{\partial \phi}{\partial t}, \tag{1.5}$$

which taking into account eq. (1.4) and linearizing gives a dynamic free-surface boundary condition on the mean water surface:

$$\left[\frac{\partial \phi}{\partial t}\right]_{z=0} = -g\eta \tag{1.6}$$

The second boundary condition (kinematic free-surface boundary condition) connects the vertical component of the velocity field $\nabla\phi$ with the vertical displacement η on the mean water surface. Its linearized version takes the form:

$$\left[\frac{\partial \phi}{\partial z}\right]_{z=0} = \frac{\partial \eta}{\partial t} \tag{1.7}$$

The velocity potential ϕ satisfying the above conditions for sinusoidal wave can be expressed as:

$$\phi = \Phi(z) e^{i(\omega t - kx)}, \tag{1.8}$$

where ω stands for the pulsation, k for wavenumber and $\Phi(z)$ is the amplitude of fluid motion beneath the water surface. The above expression fulfills Laplace's eq. (1.1) if $\Phi(z)$ satisfies the Helmholz equation:

$$\Phi''(z) - k^2\Phi(z) = 0 \tag{1.9}$$

To find a solution to this differential equation we include a third boundary condition - the finite depth of water (impermeable bottom):

$$\left[\frac{\partial \phi}{\partial z}\right]_{z=-H} = 0 \tag{1.10}$$

It can be proved that in that case $\Phi(z) = \Phi_0 cosh[k(z+H)]$, where Φ_0 is a constant value on the water surface (at $z = 0$). The above solution along with the free-surface boundary conditions (1.6) and (1.7) yields to a linear dispersion relation for gravity waves:

$$\omega^2 = gk\tanh(kH) \tag{1.11}$$

Since not only long gravity waves are the subject of our experiments, we also have to consider a surface tension (γ) force which plays a major role in restoring the flatness of the water-air interface for waves with short wavelengths λ (where $k = 2\pi/\lambda$). Then, the excess pressure is enlarged and becomes:

$$p_e = \rho g\eta + \gamma k^2 \eta \tag{1.12}$$

This modifies the boundary condition (1.6) and the capillary-gravity linear dispersion relation finally reaches:

$$\omega^2 = (gk + \frac{\gamma}{\rho}k^3)\tanh(kH) \tag{1.13}$$

1.3 Organization of the manuscript

The manuscript consists of six chapters and is organized as follows:

- **Introduction** (Chapter 1): motivation for the present experimental work with general insights on recent studies on water waves is given. A mathematical description of the linear water wave theory is also formulated.

- **Fourier Transform Profilometry for pure water waves** (Chapter 2): recent profilometry technique to measure surface elevation is described. A strong increase of the water wave attenuation in the standard FTP measurements is detected. The resonance-type-damping is discussed and is shown to be responsible for the enhanced dissipation. This scenario is experimentally validated. The successful development to the technique by appropriate water physico-chemical preparation is proposed and pure water attenuation is achieved.

- **Time-reversal of water waves** (Chapter 3): deals with one of the most important results of this thesis - the time-reversal of water waves closed in the reverberating cavity. There, first evidence of experimental water wave time refocalisation is given. Spatial and temporal refocalisation on the initial source point is shown. The role of the non-negligible wave attenuation as well as the number of re-emitting channels on the refocalisation quality is studied. Owing to the dispersive nature of the water waves, even one-channel refocalisation is presented.

- **Water Wave Turbulence** (Chapter 4): this chapter concentrates on the experimental study of wave turbulence. Because of our measurement method, we have access to the wavevector-frequency wave energy density spectra. Behavior of that spectra for various forcing frequency bandwidths and forcing amplitudes is investigated and compared with theory and recent experimental studies on that subject. Different regimes, depending on the forcing frequency bandwidth, are shown.

- **Bathymetry** (Chapter 5): the measurement of local liquid depth is a subject of this chapter. We present experimentally a feasibility of underwater depth reconstruction obtained with circle method as well as by means of Helmholtz equation. Limitations of methods and its possible applications are discussed.

- **Conclusions and perspectives** (Chapter 6): summary of the presented results is given. Major conclusions and propositions for further experimantal investigations are provided.

CHAPTER 2

FOURIER TRANSFORM PROFILOMETRY FOR PURE WATER WAVES

This chapter presents a brief description of Fourier Transform Profilometry (FTP) method for water waves and its influence on water properties, manifested by an enhanced energy dissipation. The physical basis of this effect are discussed. It is followed with the article published in *Experiments in Fluids* [68] describing the improvement to the FTP technique, which overcomes the enhanced damping effect and enables a proper investigations of the wave phenomena.

2.1 Fourier Transform Profilometry - method description

Experimental investigations of the physical phenomena demands the measurement technique and appropriate equipment. Constant progress in water waves experiments spurs researchers to invent new methods, which can make use of new technologies. The most valuable quantity in the study of surface waves is the free-surface deformation (FSD). The development of a water wave field is revealed through its FSD. The technique for studying the FSD underlies the fundamental issue in the experimental investigations of phenomena occurring on the free surface and its vicinity. In the last decades various techniques have been invented, such as refractive and reflective techniques [15], gradient detector techniques [83, 84], diffusing light photography [76], and others. Unfortunately, all these methods present limitations (only one or few-points measurements, intrusive methods) and cannot be easily applied in a wide range of experiments on water waves (for the extensive monograph of different fringe projection techniques and its recent developments see Gorthi and Rastogi [35]). Advanced research of the FSD in the laboratory scale requires a technique that allows to reconstruct, non-intrusively, the 3D surface deformation with high space and time resolution.

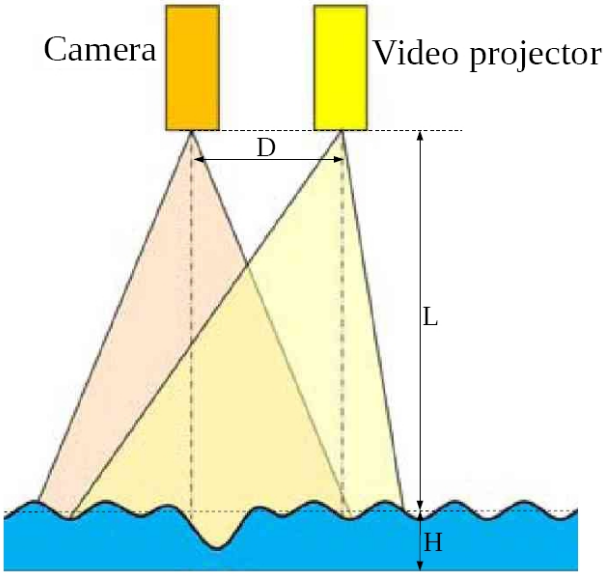

Figure 2.1: Setup of the FTP method for water waves with parallel optical axes.

A Fourier Transform Profilometry method (FTP) seemed to be a good answer to our needs. Originally developed for solid bodies [72, 73] it has been used to measure water waves firstly in 2002 [82]. Later, it has been adapted by our group for fully resolved space-time measurements of FSD. The scheme of our setup configuration is presented in the Fig. 2.1. The basic idea is as follows: the fringe pattern of known characteristic is projected onto the flat surface and recorded by a camera (reference image). When surface deforms the fringe pattern acquired by the camera is also distorted. The deformation depends on the object's profile and the perspective from which it is seen by the camera. This deformed fringe pattern is then compared to the reference one, revealing the phase difference between them (see Fig. 2.2). The information about FSD is directly encoded in this phase shift map. The appropriate detection of the underlying phase shift map $\triangle\varphi$ of the captured patterns and conversion from $\triangle\varphi$ to absolute height η are the key tasks in the FTP method for water waves.

Following [10, 58] (where the detailed description of the method can be found) the elementary geometrical optics is used to connect surface elevation η with a phase shift $\triangle\varphi$:

$$\eta = \frac{\Delta\varphi L}{\Delta\varphi - 2\pi/pD}, \tag{2.1}$$

where D is a distance between camera and videoprojector, L is a distance between surface at rest and the camera/videoprojector (see Fig. 2.1) and p the periodicity of the fringes. These values are known *a priori*, thus the phase shift $\triangle\varphi$ has to be found to reconstruct FSD.

Omitting the background variations, the intensity of light recorded by the camera for reference image I_0 and deformed image I, while projecting sinusoidal wave can be mathematically described as:

$$I_0(x,y) = A(x,y)\cos(\frac{2\pi}{p}x + \varphi_0(x)), \tag{2.2}$$

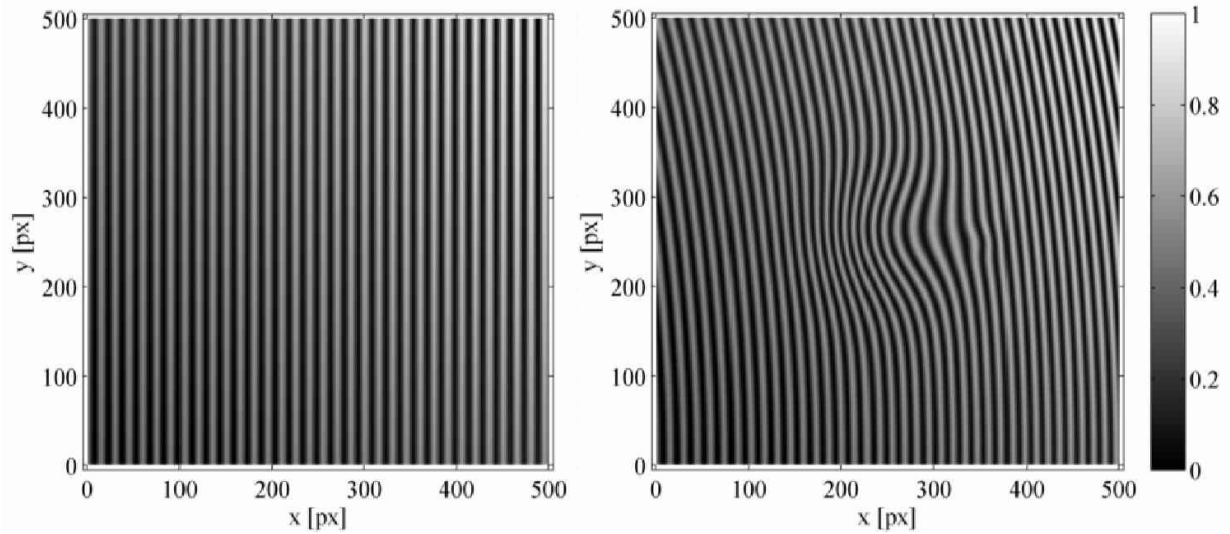

Figure 2.2: A reference fringe pattern of known characteristic is projected onto a surface at rest (on the left) and onto a deformed surface (on the right). The distortion of the fringe pattern on the deformed image with respect to the undeformed one is clearly visible. Determination of the phase shift $\triangle\varphi$ between both patterns is fundamental to reconstruct the free surface deformation (FSD) by means of the FTP method.

$$I(x,y) = A(x,y)\cos(\frac{2\pi}{p}x + \varphi(x)) \tag{2.3}$$

A stands for the amplitude intensity of the captured pattern. This light intensity amplitude A depends not only on the projection power, but also on a surface light diffusivity and a camera sensitivity. Note also that due to the inhomogeneous projection by the videoprojector (more intense at the center than close to the borders) its value is not constant on the recording area. Now, an analytical form to obtain phase shift $\triangle\varphi = \varphi(x) - \varphi_0(x)$ has to be found. Let's perform a Hilbert transform of both quantities:

$$\mathscr{H}(I_0) = A(x,y)exp[i(\frac{2\pi}{p}x + \varphi_0(x))], \tag{2.4}$$

$$\mathscr{H}(I) = A(x,y)exp[i(\frac{2\pi}{p}x + \varphi(x))], \tag{2.5}$$

where i stands for the imaginary unit. Complex conjugation of the expression (2.4) multiplied by the expression (2.5) gives:

$$\mathscr{H}(I)\cdot\mathscr{H}^*(I_0) = A^2 exp[i(\frac{2\pi}{p}x + \varphi(x) - \frac{2\pi}{p}x - \varphi_0(x))] = A^2 exp[i\triangle\varphi] \tag{2.6}$$

To separate the value of phase shift $\triangle\varphi$ from the above formula, it is enough to take the imaginary part of the natural logarithm:

$$\ln[\mathscr{H}(I)\cdot\mathscr{H}^*(I_0)] = \ln|A| + i\Delta\varphi \tag{2.7}$$

This procedure allows one to obtain $\Delta\varphi$ completely isolated from the light intensity variation A.

This method has been successfully employed in our laboratory and used by our group to study water-wave trapped modes [11, 13] and drop impact on thin liquid film [45]. It has also been used by other groups of scientists, e.g. in the case of wave turbulence on the surface of fluid [40].

Since the FTP method uses images reflected from the surface, this surface has to be light diffusive. The most natural and cheapest liquid for studying wave phenomena is obviously water, for which the sufficient surface diffusivity cannot be obtained. Our previous experimental investigations (quoted above) used white paint dissolved in water (at 1 : 200 ratio by volume). This solution does not change significantly the density and gives the sufficient light scattering to employ the FTP method.

While performing experiments it has been found that the attenuation of waves is strongly enhanced compared to the one of pure water. At the beginning a reason for such behavior was unknown. The solution to that problem was a first task of my thesis and gave unexpected results.

2.2 Surface wave attenuation - resonance phenomenon

Water waves suffer attenuation due to the viscosity μ (not considered in the linear wave theory developed in section 1.2) through two main processes of energy dissipation. The first one is the bottom friction. Its presence is significant, whenever the wavelength λ is large compared to the depth of the liquid H. In that case, the wave motion is far from being cylindrical and takes an elliptical form. Horizontal motion near the bottom induces the friction and in consequence the attenuation.

Second type of attenuation connected with the water viscosity μ is known as internal (bulk) dissipation. If we take into account water viscosity, then the stress tensor is altered and governing equation changes, namely the linearized momentum equation (1.2) takes a form:

$$\rho\frac{\partial \mathbf{u}}{\partial t} = -\nabla p_e + \mu\Delta\mathbf{u} \tag{2.8}$$

and this in consequence changes boundary condition on the free surface (it is no more only surface tension and gravity that are balanced on the surface). The new set of boundary conditions, which incorporate the viscous losses, has to be satisfied now, resulting in the wave energy dissipation. Based on the conservation of energy, one can derive the relationship between the spatial decay of the wave amplitude and the fluid viscosity [2] (presented in eq. (5) in the following article). The resulting internal attenuation by viscous shearing is substantial only for high frequency waves (low wavelengths).

None of that effects could be responsible for the largely enhanced dissipation of the intermediate waves. It has been finally discovered that the application of paint has a big disadvantage not considered before. Paint requires substances stabilizing emulsion. These surface active substances, so important in normal use of paint, can have a dramatic impact directly

on the water surface and indirectly on water wave character (amplitude and energy attenuation). Due to the surfactant's structure, containing the hydrophobic and hydrophilic groups, their molecules move towards liquid's interface (water-air interface in this case) spreading on the water surface until creating a monolayer. Hence, relatively small amount of surfactant can cause an extensive area of fluid to be covered. It may seem questionable whether the surfactant film of the thickness of few 10^{-9} m can have a considerable influence on wave attenuation, however, the investigations of the surface film rheology, carried out in the end of the XXth century, distinctly proved the enhance of the wave energy dissipation due to the physical properties of the monomolecular film. Passing wave locally expands (at the wave back) and compresses (at the wave front) the surfactant monolayer causing locally higher and lower surface tension areas (due to the local differences in surfactant density) and in consequence of surface gradients - tangential stresses.

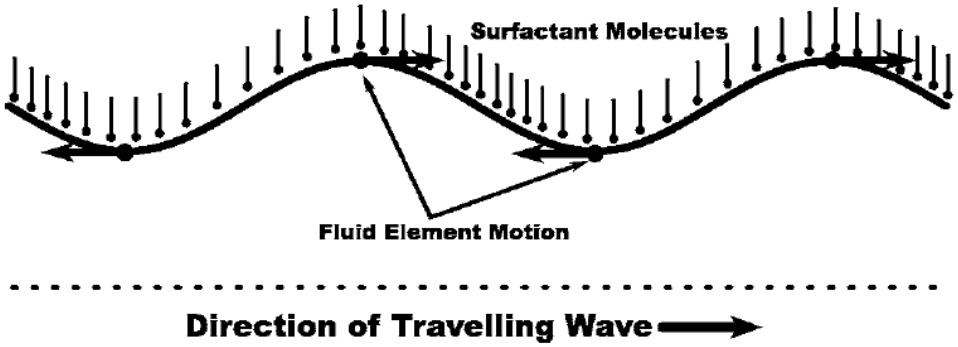

Figure 2.3: Due to the horizontal velocity on the surface of the traveling wave, the surfactant density on the wave front is increased and reduced on its wave back. Resulting surface tension gradients induce longitudinal waves (Marangoni waves). The scheme proposed by Behrozzi et al. [3]

In the consequence of elastic properties of the surface, which causes resistance to stretching and compressing, the underlying fluid changes its motion pattern from cylindrical to elliptical. For this reason, the energy is drawn away stronger by viscous friction. The resulting damping coefficient is significantly enhanced. The experiments performed in 1940s [47], in 1950s [19] and in the next decade [52, 60] showed that surface elasticity has strong influence on capillary wave damping. They revealed that damping is the strongest for low surface elasticity values, however, the precise explanation for this effect remained unanswered. Finally, in 1968, Lucassen [50] made a discovery. He proved an existance of longitudinal waves (called Marangoni waves) accompanying the capillary ones. He stated that in contrast to capillary waves, the Marangoni waves are governed by the surface elastic modulus rather than by surface tension. Due to the tangential surface stresses, the kinematic boundary condition on the surface is changed, thus the linearized Navier-Stokes equation has two different solutions: one describing well-known transversal waves and another describing Marangoni waves. These waves occur independently of each other. He also reported [50] that surface

elasticity has practically no influence on surface transversal waves, while it has strong influence on Marangoni waves, which reaches maximum damping for a low surface elasticity.

Further investigations revealed that not only capillary waves, but also short-gravity as well as intermediate ocean waves, can be significantly damped while Marangoni waves exist (see [8, 42, 51]). An in-depth explanation to these observations has been given by Alpers and Hühnerfuss [1]. They stated that increased energy attenuation is caused by the resonance-type wave damping between Marangoni and short-gravity waves.

In the second section of this chapter my article published in *Experiments in Fluids* [68] is presented. The article describes in details the theory of surface contamination and proposes the use of new pigment to obtain water-air interface light scattering with clean surface. The experimental measurements of water colored by standard paint and non-surface active pigment are given and compared. The resonance-type damping arising from the surface tensions gradients is confirmed experimentally. The mathematical formulas and physical interpretation of the calming effect due to the presence of surface film in the capillary-gravity regime is also discussed.

This study was crucial for subsequent experimental studies conducted during my thesis. It opened a possibility of proper studying of wave turbulence by means of FTP method as well as increased a quality of water wave refocalisation in time-reversal experiments.

Exp Fluids (2012) 52:519–527
DOI 10.1007/s00348-011-1240-x

RESEARCH ARTICLE

Fourier transform profilometry for water waves: how to achieve clean water attenuation with diffusive reflection at the water surface?

A. Przadka · B. Cabane · V. Pagneux · A. Maurel · P. Petitjeans

Received: 2 September 2011 / Revised: 6 November 2011 / Accepted: 23 November 2011 / Published online: 3 December 2011

Abstract We present a study of the damping of capillary-gravity waves in water containing pigments. The practical interest comes from a recent profilometry technique (FTP for Fourier Transform Profilometry) using fringe projection onto the liquid-free surface. This experimental technique requires diffusive reflection of light on the liquid surface, which is usually achieved by adding white pigments. It is shown that the use of most paint pigments causes a large enhancement of the damping of the waves. Indeed, these paints contain surfactants which are easily adsorbed at the air–water interface. The resulting surface film changes the attenuation properties because of the resonance-type damping between capillary-gravity waves and Marangoni waves. We study the physicochemical properties of coloring pigments, showing that particles of the anatase (TiO_2) pigment make the water surface light diffusive while avoiding any surface film effects. The use of the chosen particles allows to perform space-time resolved FTP measurements on capillary-gravity waves, in a liquid with the damping properties of pure water.

A. Przadka · B. Cabane · P. Petitjeans (✉)
Laboratoire de Physique et Mécanique des Milieux Hétérogènes (PMMH), UMR CNRS 7636–ESPCI–UPMC Univ. Paris 6–UPD Univ. Paris 7, 10 rue Vauquelin, 75005 Paris, France
e-mail: phil@pmmh.espci.fr

V. Pagneux
Laboratoire d'Acoustique de l'Université du Maine, UMR CNRS 6613, Avenue Olivier Messiaen, 72085 Le Mans, France

A. Maurel
Institut Langevin LOA, UMR CNRS 7587–ESPCI–UPD Univ. Paris 7, 10 rue Vauquelin, 75005 Paris, France

1 Introduction

Free surface waves are an important subject in fluid dynamics due to their practical applications in the industry (such as naval architecture, coastal and ocean engineering) and also due to the wealth of physical phenomena that they display. Most experimental studies on liquid surface deformation have used qualitative direct visualizations of the 2D surface or quantitative one-point temporal measurements. Recently, our group has proposed a full space-time resolved measurement of the surface elevation, using a technique called Fourier transform profilometry (FTP). This technique was first developed by Takeda et al. (1982), Takeda (1983) for solid surfaces. We have improved and implemented it for liquid surfaces (for details and bibliography see Maurel et al. 2009; Cobelli et al. 2009; Gorthi 2010). Typical examples of measured wave fields are shown in the Fig. 1. In the first example, a plane wave propagates with defined frequency ω over a nonuniform bottom producing wave scattering. Owing to the temporal resolution, the total measured displacement field $h(x, y, t)$ can be easily expanded in $h(x, y, t) = \sum_n Re[h_n(x, y)e^{\mathrm{in}}\omega t]$ to extract the complex field h_1 that is later analyzed. The second example is of particular interest with respect to the purpose of this paper.[1] In the case of wave turbulence experiments, the water wave field results from the nonlinear interactions of random waves. The theoretical predictions in weak turbulence theory are done in the Fourier (k, ω)-space, and this space becomes accessible

[1] The effect of monomolecular surface film, that we want to avoid, has been studied in Alpers (1989), where the authors show that the power law of the energy spectra in water wave turbulence can be modified by the presence of a surface film.

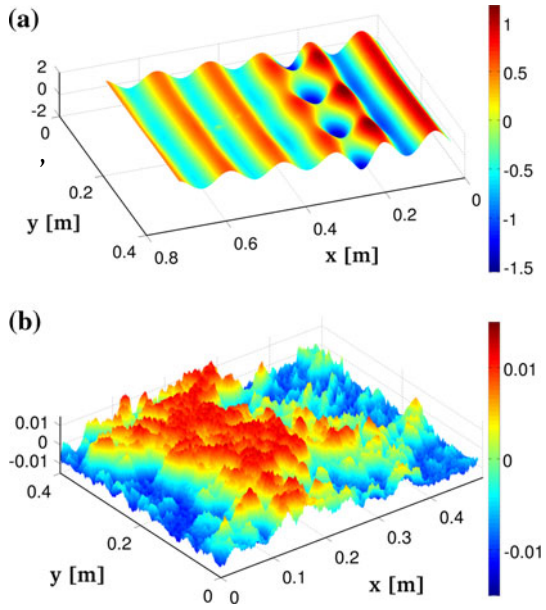

Fig. 1 Example of FTP measurements in water wave experiments: **a** real part of the wave field $h_1(x,y)$ in experiments of wave propagating over a nonuniform *bottom*. The complex field h_1 is obtained by extracting the Fourier component of the total measured field. *Colorbar* is in mm. **b** Instantaneously measured velocity field in experiments of wave turbulence. The measure of $h(x, y, t)$ gives access to the Fourier (k, ω)-space for comparison with theoretical predictions. *Colorbar* is in m/s

experimentally thanks to our full space-time resolved method.

Since the FTP method uses the deformation of fringes projected onto the free surface, this surface must scatter light. It is not possible with pure water, which is transparent and has a very low surface reflectance. Previously, light diffusivity was achieved by diluting white paint in water. This produced a substantial increase in the scattering from water (in the reflectance of the water surface). However, it was also found that the attenuation of surface waves was dramatically enhanced compared to that of pure water. This spurious attenuation is particularly harmfull when studying wave phenomena. It was soon found that it is caused by the presence of a film at the surface of water. Indeed, water is a liquid that has an unusually high cohesion and, therefore, a very high surface tension. Consequently, many species adsorb to the water–air interface, either from the water side (dissolved species) or from the atmosphere (airborne molecules or particles). These species quickly create a film at the water surface and this film may strongly change the attenuation properties of surface waves: this phenomenon is well known since the observations of the "calming effect of oil on water" by Benjamin Franklin in the eighteenth century (Franklin 1774; Behroozi et al. 2007). Since then, the attenuation due to the excitation of surface film vibrations by water waves has been studied in details by several authors (Alpers 1989; Levich 1962; Miles 1967; Lucassen 1968, 1982; Lange 1984).

We have found a way to make the water light diffusive while keeping its low attenuation property. The solution to this problem required investigation into the surface chemistry of the pigments. It also involved the use of rigorous methods to ensure good pigments dispersion without release of any surface active molecules in water (not even traces!).

This paper is organized as follows: Section 2 is dedicated to the choice and characterization of nonsurface active aqueous dispersions that can make water light diffusive while avoiding the formation of a surface film. To verify the absence of a surface film, the measurement of the surface tension of the dilute aqueous dispersions was performed. In Sect. 3, we present FTP measurements of the water wave attenuation, comparing water colored by plain paint to the dispersion of nonsurface active particles. It is also confirmed that the chosen particles allow us to restore the attenuation of pure water. Incidentally, it is shown that the enhancement of attenuation by plain paint is associated with a resonance of the film surface, in agreement with the theory (Alpers 1989; Lucassen 1968, 1982).

2 Nonsurface active dispersions

The desired characteristics of the pigment particles are threefold: (a) they must provide a high reflectance of the water surface; (b) they must be well dispersed in water; (c) they must not release any surface active molecules or ions that would form a film at the surface of water. To a large extent, these constraints are in conflict with each other and this is what makes the choice of the pigments difficult.

In order to meet condition (a), the classical choice is to use titania (TiO_2) particles. Indeed, titania has a very high refractive index ($n = 2.7$), nearly the highest among minerals. With this high refractive index, the optimum size of the titania particles is about 300 nm, which is the average size of commercially available TiO_2 pigments. Particles of this size are strongly agitated by Brownian motions and sediment quite slowly, unless they aggregate.

Condition (b) is not easily met for pure titania particles, for two reasons. Firstly, titania surfaces are ionized in water according to the classical reaction schemes:

$$\begin{aligned} \mathrm{Ti-OH} + \mathrm{OH^-} &\leftrightarrow \mathrm{TiO^-} + \mathrm{HOH}, \\ \mathrm{Ti-OH} + \mathrm{OH_3^+} &\leftrightarrow \mathrm{TiOH_2^+} + \mathrm{HOH} \end{aligned} \tag{1}$$

If one of these reactions prevails, the surface acquires a net electrical charge and the corresponding electrical potential attracts a double layer of counterions in the

vicinity of the surface. When particles approach each other, the overlap of the diffuse layers of counterions gives rise to the classical DLVO repulsions, which keep the surfaces apart and prevent particle aggregation (Evans 1994; Israelachvili 1991; Hunter 1981). However, for titania, their reactions are balanced at pH = 6, which means that the surface has an isoelectric point at this pH. Consequently, the titania surfaces do not retain any electrical double layers of counterions, and when particles approach each other, the classical DLVO repulsive forces are absent. This is true for both common crystalline forms of titania, that is, anatase and rutile.

In order to prevent the aggregation of titania particles in water, the particles' surfaces are usually covered either with a layer of another oxide (e.g., silica or alumina) or with adsorbed polyelectrolytes, such as polyacrylates. These changes shift the zeta potential curve and the location of the isoelectric point on the pH scale. Figure 2 shows the results of measurements of the electrophoretic mobility of various titania dispersions, here expressed in terms of the zeta potential, which is the electrical potential at the shear plane near the particle surface. The titania pigments provided by Kronos International, Inc. have been applied in all our dispersions.

These values of the zeta potential make it possible to predict the aggregation behavior of the various titania dispersions. Indeed, it is known from DLVO theory that zeta potentials above 40 mV provide strong electrical double layer repulsions and, therefore, predict adequate colloidal stability. Conversely, zeta potentials below 30 mV do not provide sufficiently strong electrical double layer repulsions, especially for the case of particles that have strong Van der Waals attractions as is the case for titania particles.

According to the results shown in Fig. 2, the rutile TiO_2 coated with alumina would only be acceptable at pH $\leq$ 3, which is too acidic to be handled in a large water tank with delicate electrical and optical equipment. Similarly, the rutile TiO_2 coated with alumina and silica would not aggregate in a solution with pH $\geq$ 9, but this is not acceptable in a laboratory with standard instrumentation.

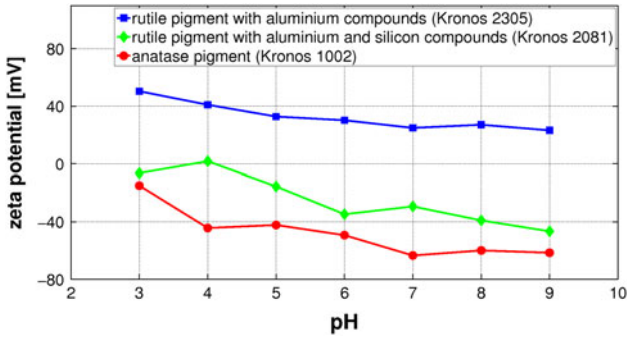

Fig. 2 Zeta potential as a function of pH

Nowadays, many titania dispersions have gained a surface charge and a high zeta potential through the adsorption of polycarboxylates, e.g., sodium polyacrylate or sodium citrate. However, the molecules are only physically bound to the titania surfaces through ionic interactions with the surface sites. A fraction of these molecules is always released in water, either because the adsorption forces are not infinitely strong or because the manufacturer has added an amount of the molecules that exceeds the saturation level of the surface (most likely). It is then in conflict with condition (c), because these excess molecules are surface active and, therefore, spontaneously adsorb and form a film at the free water surface. Indeed, we have found that all water-dispersible pigments that are made of particles with "dispersants" adsorbed on their surfaces fail to pass condition (c), as defined by the criteria presented below.

Figure 2 shows that the anatase pigment is for us the best choice since it has a zeta potential $Z_p < -40$ mV in all aqueous solutions with pH > 4. It is then possible to use pure water to disperse these particles. The water used in our experiment is purified. Its resistivity is greater than 16 MΩ cm, and its surface tension is 71 mN/m.

It is then necessary to verify that condition (c) is met with the chosen pigment. For this purpose, some experimental criteria and procedures must be defined. A criterion for the presence or absence of a film at the water surface is the value of the surface tension. If p_{film} is the film pressure, γ the measured surface tension and γ_0 the surface tension of pure water, then

$$\gamma = \gamma_0 - p_{\text{film}}$$

Typical values of p_{film} are 20 mN/m for water surfaces exposed to open air and 40 mN/m for water containing dissolved surface active molecules. Thus, a practical criterion for assessing the absence of adsorbed films at the water surface is that the measured surface tension should be within 5 mN/m of that of pure water. As noted previously, the absence of any surface film is not easily achieved with water containing dispersed pigments, as most commercially available pigments release surface active species in water. In contrast, aqueous dispersions made with the anatase pigment had surface tensions above 70 mN/m. This surface tension decreased very slowly with time because of adsorption of surface active species that have migrated from the air or other parts of the equipment (Prisle et al. 2008). A brief aspiration of the surface layer brought it back to its initial value.

For FTP experiments, it is useful to characterize the reflectance of the water surface (condition (a)) in terms of the contrast. The contrast is defined as the number of intensity gray levels between the white and black fringes.

The better resolved is the fringe signal recorded by the camera, the better resolution on the measured surface shape. This is because the resolution in the FTP measurements depends on this contrast (for more technical details see Sect. 3.1). This contrast is a combination of the absolute reflectance of the particles, of the characteristics of the projecting device and of the characteristics of the camera. In our studies, we have obtained accurate measurements for at least 50 gray levels between white and black fringes, while the contrast below 20 gray levels was found to be critical.

Figure 3 illustrates the contrast as a function of the concentration of anatase (rutile pigments are given for comparison). For the chosen anatase particles, the contrast of 50 is obtained for a concentration of 2 g/l.

Finally, the particle sedimentation has been analyzed for the chosen anatase pigment. Settling out process causes the light to be diffused not from the surface, but from the lower layer of the dispersion and this induces an error in the measurements. The sedimentation speed v can be calculated by equaling the gravity force and viscous resistance of the water

$$v = \frac{2}{9}\frac{r^2 \Delta\rho g}{\mu}, \qquad (2)$$

where r stands for particle radius, g for the gravity acceleration, and $\Delta\rho = 2.8\,\mathrm{g/cm^3}$ for the density difference between the particles and water, and $\mu = 10^{-3}$ Pa.s for the dynamical viscosity. The measurements of the particles' size for the pH in the electrically stable range showed the particle diameter to be 350 ± 50 nm.

Figure 4 illustrates the effect of the particles' sedimentation on the FTP measurements. The liquid was agitated at the initial time, and then the elevation of the free surface was measured at several times in two cases: I) the liquid was not shaken anymore (it remained at rest) during the whole experiment, and II) the liquid was excited by the wavemaker for a short time between two measurements.

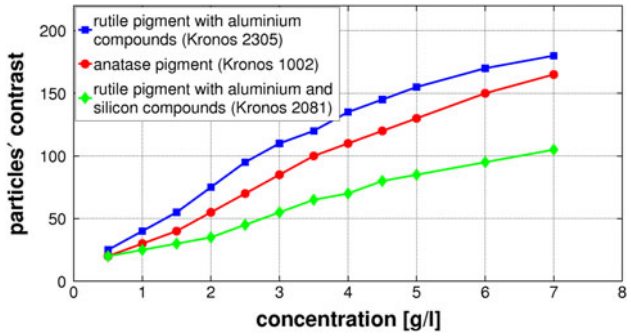

Fig. 3 Contrast as a function of the particles' concentration for anatase pigment and rutile pigments. The camera worked at 8 bits (256 gray levels)

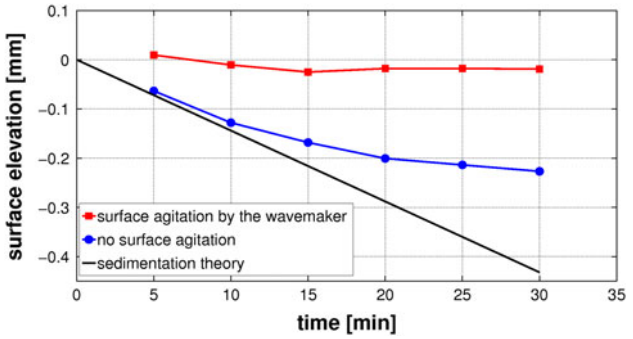

Fig. 4 The apparent surface position, as measured by FTP, as a function of time for two cases: no liquid shaking (*blue curve*), the liquid was excited by waves produced by a wavemaker during a short time between two measurements (*red curve*). *Black curve* shows the theoretical prediction for the sedimentation (Eq. 2, using the mean size of the particles). The dispersion used here is the anatase with a concentration of 4 g/l. The real position of the free surface is at zero (the *errorbar* is 0.02 mm)

In the first case, the free surface position seems to decrease in time which is connected with particles' sedimentation. Initially, sedimentation follows reasonably the theoretical prediction (black curve in the Fig. 4) using Eq. 2 with r the mean size of the particles. Then, the particles seem to sediment slower. It is connected with the existence of smaller particles which settle out slower. In the case II, the free surface position varies around the zero level within the error bar. This means that the motion induced by the wave propagation provides enough mixing to prevent the sedimentation effect.

3 FTP measurement of water wave attenuation

In 1872, Marangoni described the effect of surface tension gradients. He found that they alter the tangential stresses balance on the surface: while the wave passes, it locally expands (at the wave back) and compresses (at the wave front) the surfactant monolayer causing locally higher and lower surface tension areas due to the local differences in surfactant density. In 1968, Lucassen proved the existence of longitudinal waves on the surface film accompanying the capillary-gravity waves. These waves are governed by the surface elastic modulus of the film rather than by the surface tension and the gravity. Because of the tangential surface stresses, the kinematic boundary condition on the surface is changed, implying that the linearized Navier–Stokes equation has two different solutions: one describing well-known water waves and another one describing longitudinal waves (often called Marangoni waves).

In the past, the calming effect due to the monomolecular slicks existence has been supposed to affect only the capillary waves. Few years later, Lucassen (1982), Cini et al.

(1987) showed that such a film can induce the resonance-type wave damping between Marangoni and capillary-gravity waves, which results in a large attenuation enhancement also in the short-gravity-wave region. At the same time, the experimental evidence of the higher energy dissipation of the short gravity waves was given by Lange (1984) in the laboratory scale and by Ermakov et al. (1986) in the open sea. The mathematical description of the problem, originally proposed by Alpers (1989), can be found in the "Appendix".

3.1 Experimental details

The presented experiments were performed in the rectangular basin of 160×60 cm^2. The industrial titanium dioxide anatase particles (Kronos 1002) with a concentration 4 g/l were used to color water of 5 cm depth. The surface tension γ was measured before and regularly during experiments by Krüss K100 Tensiometer using the ring method and was equal to 71 ± 1 mN/m for water with titania particles (and 32 ± 1 mN/m for water colored by plain paint). Water temperature was maintained at 17 ± 1°C.

The FTP method implemented by Maurel et al. (2009) and Cobelli et al. (2009) was applied to measure the surface elevation $h(x, y, t)$. In the FTP method, a fringe pattern is projected onto the free surface and observed from a different position by the camera. The surface elevation information is encoded in the fringes deformation in comparison with the original (undeformed) grating image. It is, therefore, the phase shift between the reference and deformed images which contains all information about the deformed surface (see Lagubeau et al. 2010; Cobelli et al. 2009, 2011a, b, for the examples of applications).

A Phantom v9 high-speed camera was used to record the surface of 30×30 cm^2 area with a 560×560 pix^2 and a sampling frequency $f_s = 160$ fps. The horizontal resolution was equal to 0.53 mm, which corresponds to the pixel size. The vertical precision was estimated to 0.1 mm with an error of 0.05 mm. It was found to be sufficient to reconstruct the waves with typical wavelength 3–15 cm and amplitude of few millimeters (to avoid the nonlinear effects).

The experiment consists in recording the transient wave produced by a broadband wavepacket signal (modulated with a blackman window). In the case of water colored by the titania particles, the central frequency of the signal was 8 Hz and the sampling was chosen such that 20 points were recored per period. A single input signal allowed us to treat broad frequency range between 4 and 10 Hz. For water colored by plain paint, the damping is enhanced, so the frequency range around the central frequency with energy above the noise level is reduced. Thus, five different input signals were used with central frequency at 4, 5, 6, 7 and 8 Hz. The images recording finished after capturing 16,000 images (100 s), which was enough for the waves to be totally attenuated.

Since the depth of the water is constant, in the harmonic regime, at pulsation ω, it can be shown that the height perturbation is the solution of the Helmholtz equation:

$$(\triangle + \mathbf{k}^2)H = 0, \tag{3}$$

where $\mathbf{k}$ is linked to the pulsation ω by the linear dispersion relation. It is important to notice that $\mathbf{k}$ has an imaginary part due to the attenuation ($\mathbf{k} = \kappa + \mathrm{i}\beta$, where κ, β are real). In the above equation, $\mathbf{k}$ is the unknown and H stands for the time Fourier transform of the measured transient height $h(x, y, t)$:

$$H(x, y, \omega) = \int_{-\infty}^{\infty} h(x, y, t) \cdot \mathrm{e}^{-\mathrm{i}\omega t} \mathrm{d}t \tag{4}$$

The FTP measurement of the transient h allowed to obtain the H fields for a broad range of frequencies with 0.01 Hz step.

An example of the measured H field is shown in the top of the Fig. 5. Owing to the spatial resolution of the FTP

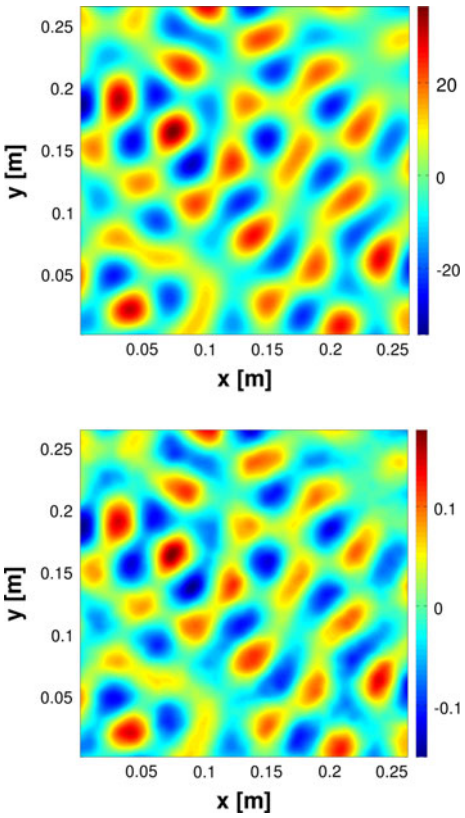

Fig. 5 Typical real value of the complex signal H (*top*) and corresponding real value of its laplacian with a negative sign: $-\Delta H$ (*bottom*)

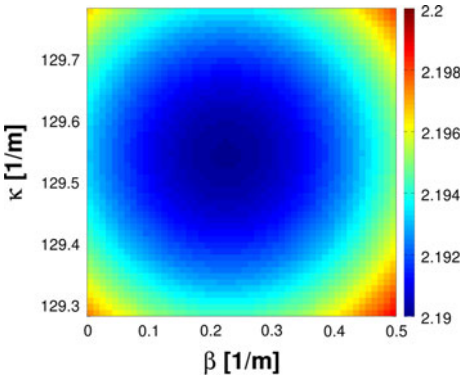

Fig. 6 Minimization of the norm $\left\|(\triangle + \mathbf{k}^2)H\right\|$ in the function of κ (the real part of the wavenumber **k**) and damping coefficient β (the imaginary part of the wavenumber **k**)

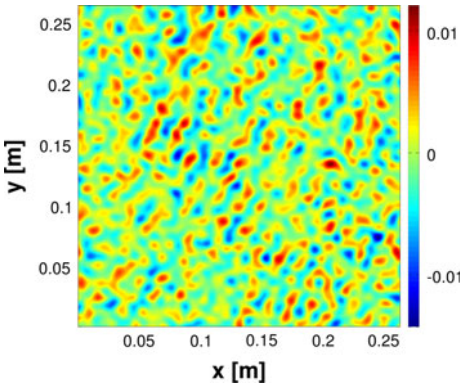

Fig. 7 Typical field of the minimization error $\varepsilon = (\triangle + \mathbf{k}^2_{\text{calc}})H$

measurements, it is possible to numerically compute the discrete laplacian

$$[\Delta H]_{ij} = \frac{1}{\Delta x^2}(H_{i-1,j} + H_{i+1,j} + H_{i,j-1} + H_{i,j+1} - 4H_{i,j}).$$

The field corresponding to $-\Delta H$ is shown in the Fig. 5 (bottom). Both patterns are very similar, indicating that the calculation of the wavenumber from the Helmholtz equation 3 can be achieved. To find the complex wavenumber **k,** we used the following method: from a given H pattern, the norm function $\left\|(\triangle + \mathbf{k}^2)H\right\|$ is minimized in the complex **k** plane. Figure 6 illustrates the minimization result. As it can be noticed from that plot, the minimum is found to be cylindrical and well defined.

The error of the minimization $\varepsilon = (\triangle + \mathbf{k}^2_{\text{calc}})H$ for the calculated wavenumber $\mathbf{k}_{\text{calc}}$ is shown in the Fig. 7. This error is one order of magnitude smaller than ΔH, and it is fairly randomly distributed in space.

3.2 Results

The above procedure allowed to determine the wavenumber **k** and thus the attenuation for surface waves on water

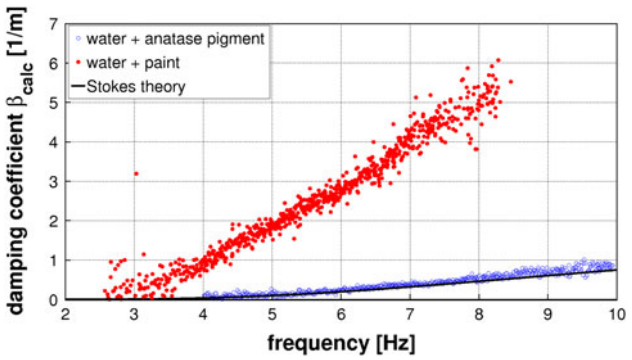

Fig. 8 Absolute damping coefficient β_{calc} in the function of the frequency. Comparison of the water suspensions obtained by adding anatase pigment and white paint. The *black line* is the theoretical attenuation β_0 given by Stokes (Eq. 5)

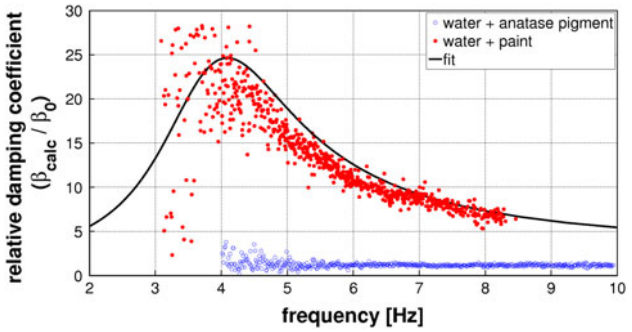

Fig. 9 Relative damping coefficient ($\beta_{\text{calc}}/\beta_0$) in the function of the frequency. Comparison of the water suspensions obtained by adding anatase pigment and white paint. The *black line* is the theoretical fit based on the formula proposed by Alpers (1989)

colored by titanium dioxide pigment (anatase) and colored by plain paint. The measured damping coefficient (β_{calc}) of these two different aqueous dispersions is compared in Fig. 8. The theoretical values for water with a clean surface are caused by the viscous attenuation in the bulk and are given by Stokes equation:

$$\beta_0 = \frac{4\kappa^2\mu\omega}{\rho g + 3\gamma\kappa^2} \tag{5}$$

We can notice that the attenuation of the titanium dispersion is comparable to the theoretical attenuation of the pure water, satisfying the aim of this study. The attenuation of the water colored by plain paint is many times larger than for the pure water and strongly depends on the frequency. It confirms that a viscoelastic film dramatically enhances the viscous energy dissipation in the boundary layer near the free surface.

Figure 9 shows the relative damping normalized by the damping of pure water. The theoretical prediction of the relative damping of water covered by a thin viscoelastic surface film is given by the Eq. 9 of Alpers (1989) (not reported here). It is compared to the measured attenuations

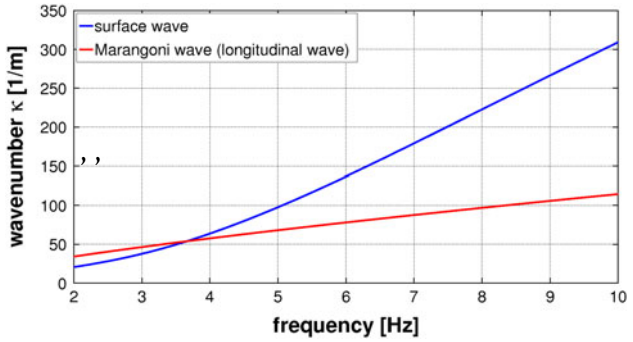

Fig. 10 Dispersion relation of the Marangoni and surface waves. The intersection region is the region of the dramatical increase in the wave energy dissipation

in the case of the water colored by plain paint, by fitting the surface-dilational modulus ε of the model. The black line in Fig. 9 shows the fit for which the absolute value of this modulus was found to be $|\varepsilon| = 0.033$ N/m and its phase angle $\theta = 180°$.

The maximum damping enhancement due to the surface film is found to be around 4 Hz where the attenuation with plain paint is 25 times larger than the attenuation of the water with clean surface. This damping resonance coincides with the intersection of the dispersion relation branches for the surface and Marangoni waves presented in the Fig. 10. The dispersion relation for Marangoni waves is given by:

$$\omega_M^3 = \left[\frac{-\mathrm{i}\varepsilon^2}{\rho\mu}\right]\mathbf{k}_M^4, \tag{6}$$

while for the water capillary-gravity waves, it is:

$$\omega_S^2 = g\mathbf{k}_S + \frac{\gamma}{\rho}\mathbf{k}_S^3 \tag{7}$$

Note also that based on the theoretical wave attenuation of the pure water (Eq. 5), the drop of the surface tension γ, caused by the presence of the surfactant, increases by itself the damping coefficient (without considering any resonance phenomena). Indeed, it was measured by Behroozi et al. (2007) that the decrease in the surface tension has influence on the attenuation jump.

Since the surface of suspension is exposed to ambient air, it becomes polluted as time evolves. Thus, the time range for which the suspension remains the damping equal to that of the pure water is in great interest for the experimentalists. Qualitative measurements were carried out systematically in time (for wave packet centered at 8 Hz). We observed a slow increase in the damping coefficient during the first 10 h. Further measurements revealed that a plateau is reached after 24 h. This enhancement of the attenuation cannot be neglected; however, it is small and does not exceed 35% of the original value. Practically, this pollution effect can be reduced by a careful surface aspiration which permits to restore the original value of the damping coefficient (where the original value means the value just after suspension preparation).

4 Conclusions

We have shown the great influence of the surface viscoelastic film on water wave attenuation when water is colored with plain paint for which the theoretical predictions of the Marangoni-surface wave resonance damping (studied by Alpers 1989) have been confirmed experimentally. Different types of titanium dioxide particles have been investigated in order to avoid the enhancement of damping. Eventually, the titanium dioxide anatase particles have been chosen to color water. They allow to perform space-time resolved FTP measurements of water waves with a damping equivalent to the clean surface case.

Acknowledgments We are thankful to Kronos for supplying us with Titanium dioxide particles. This work is founded by the ANR Tourbillonde and ProComedia.

Appendix

Let us consider the propagation of a plane wave in x positive direction (coordinate z being normal to the surface at rest) in an incompressible fluid with density ρ and dynamical viscosity μ. Neglecting the nonlinear terms, the Navier–Stokes equations for the velocity field $\mathbf{u} = [u_x, u_z]$ read:

$$\begin{aligned}\rho\frac{\partial u_x}{\partial t} &= -\frac{\partial p}{\partial x} + \mu\Delta u_x \\ \rho\frac{\partial u_z}{\partial t} &= -\frac{\partial p}{\partial z} + \rho g + \mu\Delta u_z\end{aligned} \tag{8}$$

where g denotes the gravity acceleration, and p is the pressure.

Considering the existence of the surface tension gradients, the kinematic boundary conditions on the surface (tangential and normal components, respectively) can be expressed as:

$$\begin{aligned}\frac{\partial\gamma}{\partial x} - \mathbf{T}_{xz} &= 0 \\ \gamma\frac{\partial^2\zeta}{\partial x^2} + p - p_a - \rho g\zeta - \mathbf{T}_{zz} &= 0\end{aligned} \tag{9}$$

where ζ denotes the surface elevation, p_a is the atmospheric pressure, and $\mathbf{T}$ the stress tensor. It has to be noted that the only difference in the whole mathematical formulation compared to the clean surface case is the nonzero tangential component of the stress tensor (due to the Marangoni effect of surface tension gradients). This gradient can be expressed as:

$$\frac{\partial \gamma}{\partial x} = \varepsilon \frac{\partial^2 \xi}{\partial x^2}$$

Here, ξ is the horizontal displacement of the surface, and ε denotes the surface-dilational modulus, which characterizes the viscoelastic fluid properties and is a complex number in general. The whole quantity is given by:

$$\varepsilon = |\varepsilon| \exp(-\mathrm{i}\theta)$$

A phase difference between the imposed area change and the surface tension variations, caused by a relaxation processes such as diffusion exchange, is expressed by the θ number.

Introducing the velocity field **u** as a sum of the velocity potential Φ (providing an irrotational field) and the vorticity function Ψ (providing a divergence-free field) and assuming zero velocity at infinite depth, we can obtain the harmonic wave solutions to the linearized Navier–Stokes equations (8).

Substituting these solutions into boundary conditions (9), it can be shown that the system has two solutions at each frequency. One solution corresponds to the classical capillary-gravity water wave and the other to the Marangoni wave. Lucassen (1968) showed experimentally that the wavelength of the capillary-gravity wave does not depend on the surface viscoelastic properties (is almost independent of ε), while the imaginary part of their wavenumber (damping coefficient) is strongly dependent on ε.

A simple way to obtain the dispersion relation of the Marangoni wave is to take the tangential component of the force balance at the surface assuming a horizontal Stokes boundary layer in the fluid:

$$\varepsilon \frac{\partial^2 \xi}{\partial x^2} \simeq \mu \frac{\partial u_x}{\partial z}$$

Then, the derivative $\partial_z u_x$ is equal to $m u_x$ (with the exponential decrement of the Stokes boundary layer $m = \sqrt{\mathrm{i}\omega\rho/\mu}$). Eventually, the continuity of horizontal velocity between the film surface and the fluid, $u_x = i\omega\xi$, is used to obtain

$$\varepsilon \frac{\partial^2 \xi}{\partial x^2} = i\mu\omega m \xi$$

that yields the dispersion relation for the Marangoni wave, given by Eq. 6.

This Marangoni wave is strongly damped. Assuming purely elastic film (ε is a real quantity) and denoting $\mathbf{k}_M = \kappa_M + \mathrm{i}\beta_M$:

$$\begin{aligned} \kappa_M &= \cos(\pi/8)\left(\frac{\rho\mu}{\varepsilon^2}\right)^{1/4} \omega_M^{3/4} \\ \beta_M &= \tan(\pi/8)\kappa_M \approx 0.414\kappa_M \end{aligned} \tag{10}$$

The real and imaginary part are of the same order of magnitude—the longitudinal waves are damped out very rapidly!

The capillary-gravity waves and surface waves are in general not oscillating with the same frequency and wavelength. However, the character of the dispersion relations allows to intersect the frequency-wavelength branches (Fig. 10). When the frequencies and wavelengths of the capillary-gravity wave and Marangoni wave are equal, the particle motion coincides for both waves, giving rise to a high velocity gradients in a Stokes boundary layer just beneath the surface film. This explains why the strongest enhancement of damping of capillary-gravity wave is found to be around the transverse-longitudinal resonance values.

References

Alpers W, Hühnerfuss H (1989) The damping of ocean waves by surface films: a new look at an old problem. J Geophys Res 94(5):6251–6265

Behroozi P, Cordray K, Griffin W, Behroozi F (2007) The calming effect of oil on water. Am J Phys 75:407–414

Cini R, Lombardini PP, Manfredi C, Cini E (1987) Ripple damping due to monomolecular films. J. Colloid Interface Sci 119:74–80

Cobelli P, Pagneux V, Maurel A, Petitjeans P (2009) Experimental observation of trapped modes in a water wave channel. Euro Phys Lett 88:20006

Cobelli P, Maurel A, Pagneux V, Petitjeans P (2009) Global measurement of water waves by Fourier transform profilometry. Exp Fluids 46:1037–1047

Cobelli P, Pagneux V, Maurel A, Petitjeans P (2011a) Experimental study on water-wave trapped modes. J Fluid Mech 666:445–476

Cobelli P, Przadka A, Petitjeans P, Lagubeau G, Pagneux V, Maurel A (2011b) Different regimes for water wave turbulence. Phys Rev Lett 107:214503

Ermakov SA, Zujkova AM, Panchenko AR, Salashin SG, Talipova TG, Titov VI (1986) Surface film effect on short wind waves. Dyn Atmos Oceans 10:31–50

Evans DF, Wennerström H (1994) The colloidal domain. VCH, Wiley, New York

Franklin B (1774) Of the stilling of waves by means of oil. Philos Trans 64:445–460

Gorthi SS, Rastogi P (2010) Fringe projection techniques: whither we are? Opt Lasers Eng 48(2):133–140

Hunter R (1981) Zeta potential in colloid science. Academic Press, New York

Israelachvili J (1991) Intermolecular and surface forces. Academic Press, New York

Lagubeau G, Fontelos M, Josserand C, Maurel A, Pagneux V, Petitjeans P (2010) Rosace patterns in drop impact. Phys Rev Lett 105:184503

Lange P, Hühnerfuss H (1984) Horizontal surface tension gradients induced in monolayers by gravity wave action. J Phys Oceanogr 14:1620–1628

Levich VG (1962) Physicochemical hydrodynamics. Prentice-Hall, Elmsford Park

Lucassen J (1968) Longitudinal capillary waves. Part 1—theory. Trans Faraday Soc 64:2221–2229

Lucassen J (1982) Effect of surface-active material on the damping of gravity waves: a reappraisal. J Colloid Interface Sci 85:52–58

Marangoni C (1872) Sul principio della viscosita superficiale dei liquidi stabili. Nuovo Cimento Ser 5/6(2):239–276

Maurel A, Cobelli P, Pagneux V, Petitjeans P (2009) Experimental and theoretical inspection of the phase-to-height relation in Fourier transform profilometry. Appl Opt 48(2):380–392

Miles JW (1967) Surface wave damping in closed basins. Proc R Soc Lond A 297:459–475

Prisle NL, Raatikainen TR, Sorjamaa R, Svenningsson B, Laaksonen A, Bilde M (2008) Surfactant partitioning in cloud droplet activation: a study of C8, C10, C12 and C14 normal fatty acid sodium salts. Tellus B 60:416–431

Takeda M, Mutoh K (1983) Fourier transform profilometry for the automatic measurement of 3-D object shapes. Appl Opt 22:3977–3982

Takeda M, Ina H, Kobayashi S (1982) Fourier-transform method of fringe-pattern analysis for computer-based topography and interferometry. J Opt Soc Am 72(1):156–160

2.4 Supplementary results

As it was mentioned in the article, surface becomes polluted as time evolves. Fig. 2.5 shows a relative damping coefficient just after suspension preparation (blue), after 24 hours of surface exposure to ambient air (green) and after carefull surface aspiration (red). We can observe that after 24 hours the attenuation coefficient is shifted up and reduces after surface aspiration.

This behavior has been also confirmed in the stationary state, when we imposed not a broadband signal, but a constant sinusoidal wave with a frequency of 8 Hz. In this case the recorded signal of 10 s was enough to calculate time Fourier transform of the measured height. The measurements started when the waves produced due to the effect of switching on the wavemaker were totally attenuated. The results of the stationary state validate results obtained for transient waves. The usefulness of surface aspiration is also proved (see Fig. 2.5).

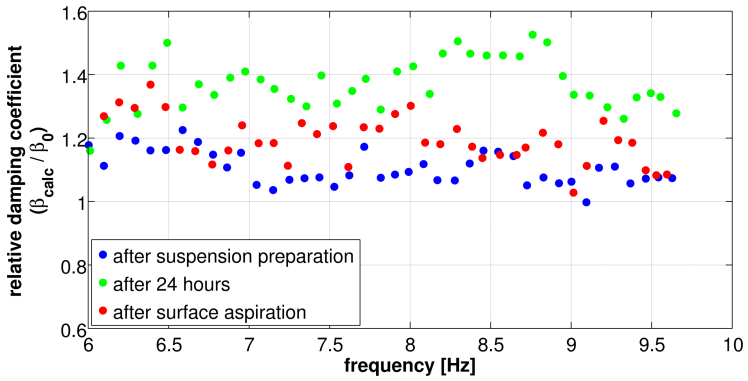

Figure 2.4: Relative damping coefficient (β_{calc}/β_0) in the function of the frequency. The influence of surface pollution on damping coefficient can be observed 24 hours after suspension preparation. Surface aspiration reduces that effect.

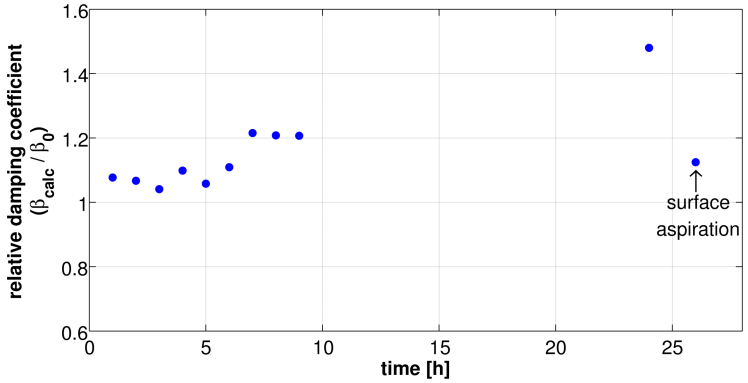

Figure 2.5: Relative damping coefficient (β_{calc}/β_0) in the function of time for the measurements performed in the stationary state. The influence of surface pollution on damping coefficient during first 24 hours after suspension preparation is presented. Surface aspiration reduces that effect.

CHAPTER 3

TIME-REVERSAL OF WATER WAVES

Recent developments, applications and theoretical description of perfect time-reversal phenomenon, as well as its limitations in the reality are given in this chapter. It is followed by the description of the experimental investigations for time-reversal water waves. The preprint of the article accepted for publication in *Physical Review Letters* [69] presents the most important results obtained during this study. The chapter is completed with the supplementary material not published in the mentioned article.

3.1 Motivation

Wave focusing is an important phenomenon commonly present in nature and everyday life. Spatial focusing of monochromatic or pulsed waves can be reached by means of optical or acoustic lenses, such as light focusing by the assembly of lenses in eyes or acoustic focusing by means of headphones. Wave focusing is also a subject of extensive studies in water waves. This is mainly due to the appearance of steep waves (called freak or rogue waves) in the open sea, which have huge potential for damage and thus are of great importance for oceanographers and physicists. The mechanism for the presence of these extreme waves highly localized in space and time is still not fully understood, however, it has been demonstrated that nonlinear effects are essential in their evolution [5]. Large amplitude waves can also be expected as a result of interactions between surface gravity waves and a mean flow (see [67] for theoretical description and [56, 75] for recent experimental studies).

It is shown numerically and experimentally in [70] that nonlinear wave group evolution of initially wide bandwidth can emerge as a single steep wave if numerous frequency harmonics arrive in phase to the certain location. It is proved that it is possible to obtain a designed form of the wave in the focalisation point by the backward integration of the Zakharov equation [78] starting from the focusing location till the source location. The process of formation

of huge waves on water in this case is a result of dispersive wave grouping due to an appropriate phase modulation of initial wave trains. Note that the signal in the source location has wide frequency spectrum with moderate amplitude, so can be easily generated by the wavemaker in the case of experimental investigations.

The above procedure allows the focusing of waves in time and space, however, it has inherent limitations and difficulties. The evolution of the wave group (in time and space) has to be calculated and a well-controlled signal, far from the focusing location, has to be sent to recreate the designed form of the wave in the focusing location. In this case, the re-emitting position with respect to the focusing location, as well as the geometry of the propagation medium has to be known. The following paragraphs present a method that can re-create wave (*ergo*: re-focus energy) in time and space, while the geometry, distance from source and focusing point as well as the form of the wave to re-create is *a priori* unknown!

The latter can be accomplished due to the time-reversal invariance of the wave equation in lossless media. It allows one to examine a unique phenomenon associated with wave physics - the focusing back energy of the wave at the initial source point, as though the wave was being played backwards (wave has the same shape as the initial one, but propagates in the reverse direction). The time-reversal technique was developed at the beginning of the 1990s (primarily for acoustic waves) by a group of Mathias Fink [6, 31, 77] and is now employed in many different fields of wave physics. If one can claim that it is trivial that, due to the time-invariance of the wave equation, the re-emitted energy will focus back on the original source, it is obviously not trivial that the refocalisation of waves is possible in inhomogeneous open system (with unknown geometry), in multiple scattering medium, in chaotic cavities, with only single source/receiver or in the presence of nonlinearities and attenuation. Since the first experimental evidences on the efficiency of this concept its limitations, refocusing quality and perspectives have been extensively studied in theoretical as well as applied aspects. Its applications have been investigated in the areas such as indoor wireless communications [49], seismic source location [46], tumor detection [44] and sensors to measure small perturbations in the system [71]. It is then unexpected that water waves were never tested experimentally in the case of time-reversal focusing and we are first to qualitatively demonstrate its feasibility.

In a classical time-reversal experiments the wave emitted from source point generates a wave field. The field is closed and recorded on a surrounding surface. In the second step the recorded signal is reversed in time and re-emitted into the system. The resulting field undoes the same phase changes and distortions that they suffered in time-forward propagation focusing back on the source position [33].

It has been shown that time-reversal experiments are not limited only to the closed cavities. They can also converge on the targets (scattering centers) in the open system (with inhomogeneous medium). In the case of acoustic waves, the area which contains a target (for example a kidney stone) is first illuminated. The wave is distorted due to inhomogeneities and reflects from the target. The backscattered pressure is recorded by the transducer array, then time reversed and re-emitted. The resulting pressure field focuses back on the target [77]. Further experiments [18] surprisingly proved that even in the presence of high-order scatter-

ing in the open system (that was initially considered to limit the time-reversal efficiency [31]) acoustic waves can be successfully converged to its source. In addition, the focusing resolution was found to be below the theoretical limit for the aperture used in the experiment.

In a case of a closed cavity, to ideally reconstruct a refocusing wave, the perfect measurement of the Green's function (and its normal derivative) over the whole surrounding surface should be performed. This would require an infinite number of transceivers to capture the entire signal emitted from the source. Also, a reciprocity theorem has to be fulfilled - impulse response from the source point to receiving point and from receiving point to source point are identical (the positions of the source point and receiving point can be reversed without altering the wave field). In practice, the refocusing quality is reduced because of the finite number of transceivers and the diffraction limit of the retransmitting devices.

Despite these limitations, it has been shown [20] that a confined reflective cavity with chaotic ray dynamics can simplify time-reversal focusing to a single transceiver (one-channel time-reversal) whilst maintaining very good spatial and temporal quality of refocusing! The quality increases with the time-reversal window. The presence of multiple reflections and no signal "leaks" might indicate that in the lossless media all the information about the system can be collected in one point, however, theoretical [21] and experimental [22] investigations distinctly proved that even in the case of infinite time-reversal window the reversal focusing quality is limited.

Note that if the propagation medium is attenuative, then the odd order time-derivative operator appears in the wave equation and this might suppress the time-reversal invariance as well as the validity of the reciprocity theorem. Water waves have strong attenuation, thus their time-reversal focusing is not obvious. On the other hand, they are dispersive by nature which can largely enhances the refocusing quality and decreases the number of re-emitters needed in the backward step. This encouraged us to test, experimentally, the possibility of time-reversal water waves focusing in a reverberating cavity.

3.2 Time-reversal - problem formulation

Following [21] and [32] the mathematical description of time-reversal focusing can be developed.

Let us consider a wave propagating with velocity c (in general dispersive) in a lossless medium with a wave scalar field $\sigma(\mathbf{r},t)$ and the source term function $f(t)$ at the position $\mathbf{r}_0$, then the wave equation reaches:

$$(\Delta - \frac{1}{c^2}\frac{\partial^2}{\partial t^2})\sigma(\mathbf{r},t) = -\delta(\mathbf{r}-\mathbf{r}_0)f(t) \tag{3.1}$$

If for now, for simplicity, we assume that our source is impulsive $f(t) = \delta(t)$ then the associated Green's function verifies:

$$(\Delta - \frac{1}{c^2}\frac{\partial^2}{\partial t^2})G(\mathbf{r},\mathbf{r}_0,t) = -\delta(\mathbf{r}-\mathbf{r}_0)\delta(t) \tag{3.2}$$

Note that with respect to the causality in physics, we have chosen a retarded Green's function - diverging wave from the source (see Fig. 3.1).

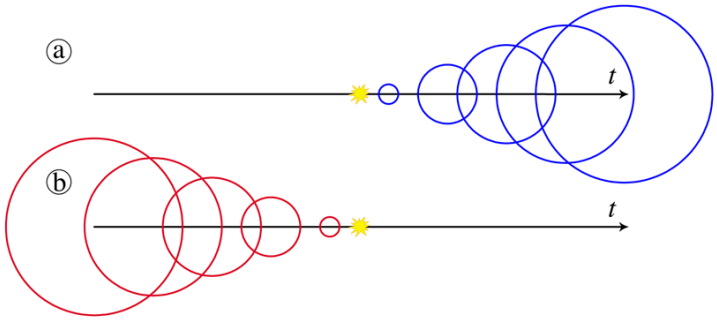

Figure 3.1: A schematic view of the (a) retarded and (b) advanced Green's function solutions. The retarded solution diverges from the source (the yellow star), while the advanced solution converges to it. Relationship between causes and effects inclined us to choose retarded solution in the eq. (3.2) - diverging wave from the source. The aim of the time-reversal is to create an advanced solution!

In the perfect time-reversal phenomenon, in its first step, the wave elevation and its normal derivative should be measured in every point $\mathbf{r}_s$ on the surrounding surface S during a time-window ΔT. In the second step, the obtained signals are time reversed and re-emitted (with an inverse direction as they arrived). The original source becomes passive and surface becomes active with sources:

$$\begin{aligned} \sigma_s(\mathbf{r}_s, t) &= G(\mathbf{r}_s, \mathbf{r}_0, T-t) \\ \partial_n \sigma_s(\mathbf{r}_s, t) &= \partial_n G(\mathbf{r}_s, \mathbf{r}_0, T-t) \end{aligned} \tag{3.3}$$

Taking into account the above sources, the Gauss theorem, spatial reciprocity and time-reversal invariance the time reversed field σ_{tr} yields:

$$\sigma_{tr}(\mathbf{r}, t) = G(\mathbf{r}, \mathbf{r}_0, T-t) - G(\mathbf{r}, \mathbf{r}_0, t-T) \tag{3.4}$$

The time-reversal generates not only the advanced solution, but a difference of the advanced and retarded solutions. Indeed, while the propagation equations can be reversed in time, the energy input induced by the impulse cannot (we cannot suck out the energy from the system). For that reason, the converging wave (advanced solution) typically diverges (retarded solution) after the recompression time T. Note that it has been shown that if a source point can work as an emitter, then an excitation function can be also time reversed (sink) and imposed in the anti-phase to the diverging wave creating a super-focusing of the reversed signal.

We simplified the calculation by introducing the impulsive source. If we want to obtain the time reversed field after the excitation $f(t)$, the right hand side of the expression obtained in (3.4) should be convoluted with a signal $f(-t)$. This gives us a perfect time reversed signal in the cavity.

In reality we can simplify this problem and consider that the surface is located on the far field from the source, then the source due to the re-transmitted normal derivative can be omitted (see eq. (3.3)). In addition, only the finite number N of the transceivers on the surrounding surface can be analyzed. Then - the signal at the source location $\mathbf{r}_0$ after emitting a time reversed signal from the N positions reaches:

$$\sigma_{tr}(\mathbf{r}_0, t) \propto \sum_{i=1}^{N} G(\mathbf{r}_0, \mathbf{r}_i, -t) \otimes G(\mathbf{r}_0, \mathbf{r}_i, t), \tag{3.5}$$

where $\otimes$ is a convolution operator and from the definition:

$$G(\mathbf{r}_0, \mathbf{r}_i, -t) \otimes G(\mathbf{r}_0, \mathbf{r}_i, t) = \int d\tau G(\mathbf{r}_0, \mathbf{r}_i, t+\tau) G(\mathbf{r}_0, \mathbf{r}_i, \tau) \tag{3.6}$$

Each term of N channels in this sum reaches maximum at $t = 0$ and is added constructively, while in other times this summation is uncorrelated, thus a peak appears for $t = 0$!

3.3 One-channel time-reversal in chaotic cavity

As was mentioned earlier, time-reversal can be carried out using down to one sensor and transmitter. The main difference between one-channel time-reversal with the problem formulated in the previous section is that the boundaries do not absorb the energy, the receiver can be localized inside the cavity and that the re-emitted signal is omnidirectional.

The requirement is for the cavity to be chaotic, so that wavefronts leaving the source in any direction eventually come to the sensor to be recorded. This is analogous to an ergodicity condition.

In that case if we inject a signal $f(t)$ at point A, then a signal obtained in B can be expressed as $f(t) \otimes G(\mathbf{r}_A, \mathbf{r}_B, t)$. This signal has to be time reversed and re-emitted. The refocusing signal $S_A(t)$ arriving in the second step to point A thus reaches:

$$S_A(t) = f(-t) \otimes G(\mathbf{r}_A, \mathbf{r}_B, -t) \otimes G(\mathbf{r}_B, \mathbf{r}_A, t) \tag{3.7}$$

Unfortunately, not all the information imposed in point A can be gathered and re-transmitted by point B, giving rise to the temporal and spatial sidelobes.

Let us consider a signal that is injected, captured and re-transmitted by the same point A. In the case of perfect time-reversion, we would expect from the refocusing signal to give: $f(-t) \otimes G(\mathbf{r}_A, \mathbf{r}_A, -t)$. Using an eigenmode analysis it can be proved [21] that, for long time-reversal signals, the temporal shape of the refocused signal $S_A(t)$ is equal to the given perfectly reversed signal ($f(-t) \otimes G(\mathbf{r}_A, \mathbf{r}_A, -t)$) convoluted with the backscattering impulse response of B:

$$f(-t) \otimes G(\mathbf{r}_A, \mathbf{r}_B, -t) \otimes G(\mathbf{r}_B, \mathbf{r}_A, t) = f(-t) \otimes G(\mathbf{r}_A, \mathbf{r}_A, -t) \otimes G(\mathbf{r}_B, \mathbf{r}_B, t) \tag{3.8}$$

and we obtain a cavity equation:

$$G(\mathbf{r}_A, \mathbf{r}_B, -t) \otimes G(\mathbf{r}_B, \mathbf{r}_A, t) = G(\mathbf{r}_A, \mathbf{r}_A, -t) \otimes G(\mathbf{r}_B, \mathbf{r}_B, t), \tag{3.9}$$

The above formula introduces a reduction in the reversal quality in terms of the backscattering impulse response of B. This impulse will deviate the perfect focusing. It suggests that the loss of the information is entirely due to point B. Indeed, point B (unlike point A) is located in the nodes of some excited eigenfrequencies and thus cannot reproduce them! In addition, the weight of the other eigenmodes is also not perfectly re-injected (it depends on the measured amplitudes of the eigenmodes at point B during the first step). This gives rise to the appearance of the temporal sidelobes in the refocused signal. It has been found [21] that the refocusing peak at A contains roughly 1/3 of the total energy present in all cavity.

Despite the wrong re-transmission of the eigenmodes' amplitudes, all of their phases are correctly set back to 0 at the point A at the time $t = 0$. In the effect, they are constructively superposed in contrast to the rest of the cavity, where the superposition is decorrelated. We can then conclude, that increasing the number of frequencies excited in the cavity increases the refocalisation quality.

By analogy to the number of excited frequencies, the use of several reversal points can lead to the increased refocalisation quality! In this case, refocused signal $S_A(t)$ is the sum of signals originating from different time-reversal points and thus based on the cavity equation (3.9):

$$S_A(t) = f(-t) \otimes G(\mathbf{r}_A, \mathbf{r}_A, -t) \otimes [G(\mathbf{r}_B, \mathbf{r}_B, t) + G(\mathbf{r}_C, \mathbf{r}_C, t) + ...] \tag{3.10}$$

A constructive superposition indicates that the peak amplitude increases linearly with number of re-emitters N, while noise should be proportional to its square root ($\sqrt{N}$).

There is also one more crucial parameter to be discussed, namely the time reversal window ΔT. In this section, till now, we assumed that $\Delta T \to \infty$. Introduction of the finite ΔT will induce the noise in the system. The influence of ΔT on the refocalisation quality was a subject of experimental study presented in [22]. The re-injected signal from B is omnidirectional, thus the waves are sent in directions that find their way back to the source (and as mentioned above - all of them set back their phase to 0 at the source point at time $t = 0$) as well as in directions that take the wrong way, and though are randomly superposed in all the cavity at the recompression time. It has been found that, if we consider noise induced only due to the finite ΔT, the quality of the refocused signal increases linearly with ΔT. However, considering also the residual noise (induced by imperfect reconstruction of the weights of the eigenmodes in B) the saturation is reached for large ΔT. It is never possible to infinitely increase refocusing quality, because even for infinite ΔT it is not possible to recover the signal lost in B.

The important condition to perform succesful one-channel time-reversal is a low absorption coefficient. The emitted and re-emitted wavefronts may undergo several reflections on the borders between the source and the sensor. This condition is easily verified by acoustics waves whose absorption coefficient is close to zero at the experimental time scale (for an example see [20], where decay time corresponds to around 100000 to 200000 periods of the injected signal and is about 10 times longer than the largest time-reversal window).

In the case of water waves, the attenuation is much larger and (for gravity waves in the lab-

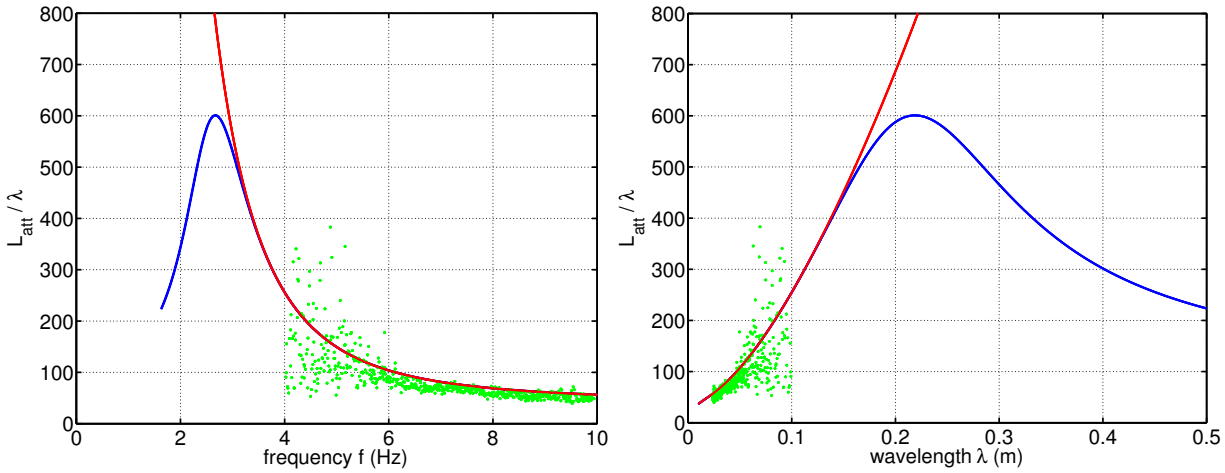

Figure 3.2: Ratio of typical attenuation length L_{att} to the wavelength λ in the function of the frequency (left) and wavelength λ (right). Blue line corresponds to the waves at the laboratory scale and considers both: viscous damping and bottom friction (for water depth $H = 10$ cm). Red line corresponds to the waves on the sea and then takes into account only viscous damping. Green points (given for the comparison) are our experimental values presented and discussed in the Chapter 2 "Fourier Transform Profilometry for pure water waves". Influence of finite water depth is visible, which suggests that time-reversal of water waves should be more effective for sea waves.

oratory scale) corresponds to roughly few hundreds periods (see Fig. 3.2). One can doubt that time-reversal refocusing in that case cannot be reached. It is shown in the following article that the quality of the refocusing is highly damped due to the attenuation, however, thanks to the broadband excitation function - a successfully refocusing is obtained! During our experiments we used a one-period signal with a central frequency $f_0 = 5$ Hz, which is able to re-create small focal spot (compared to the measurement field) and excites broad bandwidth of the frequencies, which do not suffer a huge damping due to the strong viscous forces nor bottom friction. It is a first experimental evidence of time-reversal phenomenon for water waves.

Time-reversal of water waves

A. Przadka, S. Feat, P. Petitjeans
Physique et Mécanique des Milieux Hétérogènes, PMMH,
UMR CNRS 7636 - ESPCI - UPMC Univ. Paris 6 - UPD Univ. Paris 7, Paris, France

V. Pagneux
Laboratoire d'Acoustique de l'Université du Maine,
UMR CNRS 6613, Avenue Olivier Messiaen, 72085 Le Mans, France

A. Maurel, M. Fink
Institut Langevin, ESPCI & CNRS, UMR CNRS 7587,
10 rue Vauquelin, 75005 Paris, France

We present time-reversal experiments demonstrating refocusing of gravity-capillary waves in water tank cavity. Owing to the reverberating effect of the cavity, only few channels are sufficient to reconstruct the surface wave at the point source, even if the absorption is not negligible. Space-time resolved measurements of the waves during the refocusing allow to quantitatively demonstrate that the quality of the refocusing increases linearly with the number of re-emitting channels. Numerical simulations corresponding to water waves at larger scales, with negligible damping, indicate the possibility of very high quality refocusing.

Time-reversal of acoustic, elastic and electromagnetic waves has been extensively studied in recent years [1, 2]. In a standard TR experiment, waves generated by a source are first measured by an array of antennas positioned around the source, and then time reversed and simultaneously rebroadcasted by the same antenna array. Due to the time invariance of the wave process, the re-emitted energy will focus back on the original source whatever the complexity of the propagation medium [3]. According to diffraction theory, an exact control of the wave would require to measure and time reverse both the wave and its normal derivative along a closed surface. This would require a large number of antennas and time-reversal channes. However, it has been shown that the reversal remains quite good even when these conditions are not fulfilled by the experiment [4]. One surprising result that was demonstrated both for elastic [5–7] and electromagnetic waves [2] was that when a broadband wave field is trapped inside a reverberating cavity, a one channel time-reversal antenna is enough to refocus back on the source. In this case, the refocusing quality depends directly on the number of cavity modes that are excited by the source. To better resolve these modes, breaking the symmetries of the cavity avoids mode degeneracy which improves the refocusing [6].

The present work concentrates on the application of time-reversal to the focusing of water waves in a laboratory tank which plays the role of reverberating cavity. Although water waves are ubiquitous and easily observable, they have never been tested in a time-reversal experiment (for theoretical formulation of time-reversal for water waves see [8]). This is certainly due to their complexity: to cite Richard Feynman, "[water waves] that are easily seen by everyone and which are usually used as an example of waves in elementary courses [...] are the worst possible example, because they are in no respects like sound and light; they have all the complications that waves can have." [9]. Water waves are scalar

waves, that refer to the evolution of small perturbation of the height of fluid $\eta(\mathbf{r}, t)$ under the action of gravity and surface tension. They are dispersive by nature, nonlinear when generated with standard wavemakers, and they experience strong damping at the scale of a laboratory experiments. The effect of dispersion on time-reversal process has already been studied in time-reversal experiments for guided elastic waves [5, 10]; these waves are dispersionless in free space and the dispersion is due only to the reflection on the boundaries of the waveguide. In the case of water waves the dispersion is intrinsic but preserve the time-reversal invariance (obviously not taking the damping into account).

The effect of the nonlinearities has been experimentally studied in [11] for acoustic waves where it has been shown that the time-reversal invariance is preserved as long as nonlinearities do not create dissipation, *i.e.* as long as the propagation distance is smaller than the shock distance. In the case of water waves, the effect of nonlinearities has been theoretically studied displaying that refocusing is robust with respect to nonlinearities, when small but not negligible [8]. Eventually, the main complication in a water wave TR experiment is the damping. This latter has various origins: i) the viscosity of the fluid that produces a bulk damping, ii) the bottom friction (water waves produces oscillation at the bottom), which occurs when the wavelength is not small compared to the fluid depth since the penetration depth of the wave is given by the wavelength, iii) the film surface effect that is able to create an important friction just beneath the surface of the liquid (the calming effect of oil on troubled waters [12]), iv) the walls of the water tank. The damping may break time-reversal invariance if it is too strong. It was already shown by our group in [13], where the same experimental set-up was used, that no surface film effect is present and that damping coefficient is comparable to the one of pure water.

In this letter, we show for the first time an experimental proof of time-reversal of gravity-capillary waves. The experiment is conducted in a water tank cavity to take advantage of multiple reflections on the boundaries. The influence of the number of channels in the time-reversal mirror is studied and it allows us to show that a small number of channels is sufficient to obtain the TR refocusing owing to the reverberating effect of the cavity.

The reverberating tank is filled with water with depth at rest $H = 10$ cm. The dimension of the rectangular tank is 53×38 cm^2 with obstacles placed in order to break the spatial symmetries (see Fig. 1). The waves are generated by using a vertical conical vibrator and recorded by using an optical method (note that this differs from TR experiments in acoustics that use the same transducer to record and to regenerate the wave). We perform a typical one channel TR experiments in two steps. In the first step of emission, a wave packet is generated from a conical vibrator that can be considered as a point source. In a second step, the signal recorded at a receiver point is time reversed and re-emitted.

The time reversed wave is expected to refocus spatially at the source point and refocus temporally at the recompression time. As previously stressed, the key point to ensure TR refocusing is the number of cavity modes that the wave packet has been able to excite in the first step of the TR.

After a few experimental trials, the authors found the central frequency $f_0 = 5$ Hz the best to obtain good refocusing in time and space. This is a compromise between the bulk dissipation that grows with a frequency increase and the bottom friction that becomes significant while decreasing frequency (note: no significant peaks in the low frequency region in the Fig. 2(b)). The Fig. 2(a) shows the signal recorded at one point (point R_1 in Fig. 1)

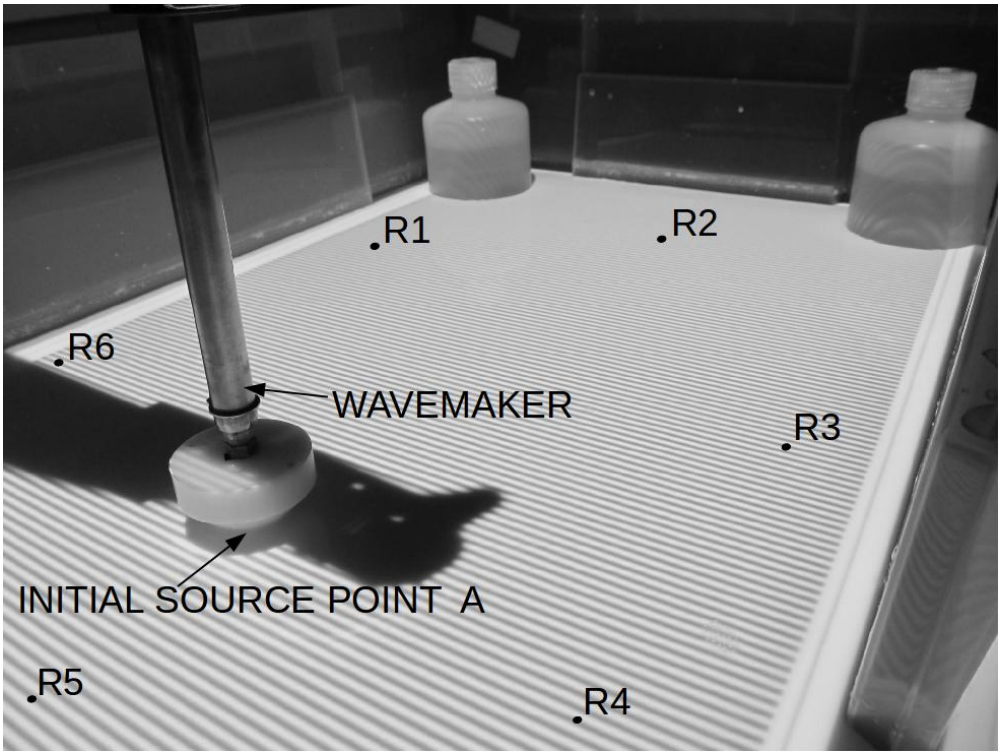

FIG. 1. Water tank used in the experiment. Point A is at the initial source position. Note the fringes used for the Fourier Transform Profilometry technique. Points R_1 to R_6 correspond to the positions of the different channels of the time-reversal mirror. At each of these channel positions the wave is measured and can be re-emitted after the time-reversal operation.

when a one-period sinusoidal pulse centered at f_0 Hz is generated at the initial source position. The duration of the signal is typically 20 s, corresponding both to reverberating effects and linear dispersion effects. This latter is given by the linear dispersion relation for water wave propagation (taking into account the effects of finite depth H and surface tension γ):

$$\omega^2 = \left(gk + \frac{\gamma}{\rho} k^3 \right) \tanh kH, \tag{1}$$

where k denotes the complex wavenumber, g the gravity acceleration and ρ the water density. The wavelength at central frequency f_0 is $\lambda = 6$ cm. The magnitude of nonlinearity of the waves based on the maximum measured gradient of surface elevation was found to be $\epsilon = 0.13$. The attenuation is such that the wave can propagate over roughly 100 wavelengths, i.e. about 10 to 20 times the lengthscale of the cavity. This is consistent with the 20 s duration of the time signal recorded at one point in the cavity (Fig. 2(a)) since the phase velocity at the central frequency is 0.33 m/s corresponding to $12 - 17$ reflections from the boundaries. The spectrum of the signal recorded during the direct propagation is shown in Fig. 2(b). It presents several peaks (one can count roughly 20 peaks) corresponding to the eigenmodes of the cavity that have been excited. Although the initial pulse covers a broadband frequency range [0 15] Hz, the signal recorded is limited to frequencies smaller than about 10 Hz. We have checked that this is an effect of the attenuation: direct numerical simulations of the 2-D wave equation in the same geometry but omitting the attenuation give a spectrum with

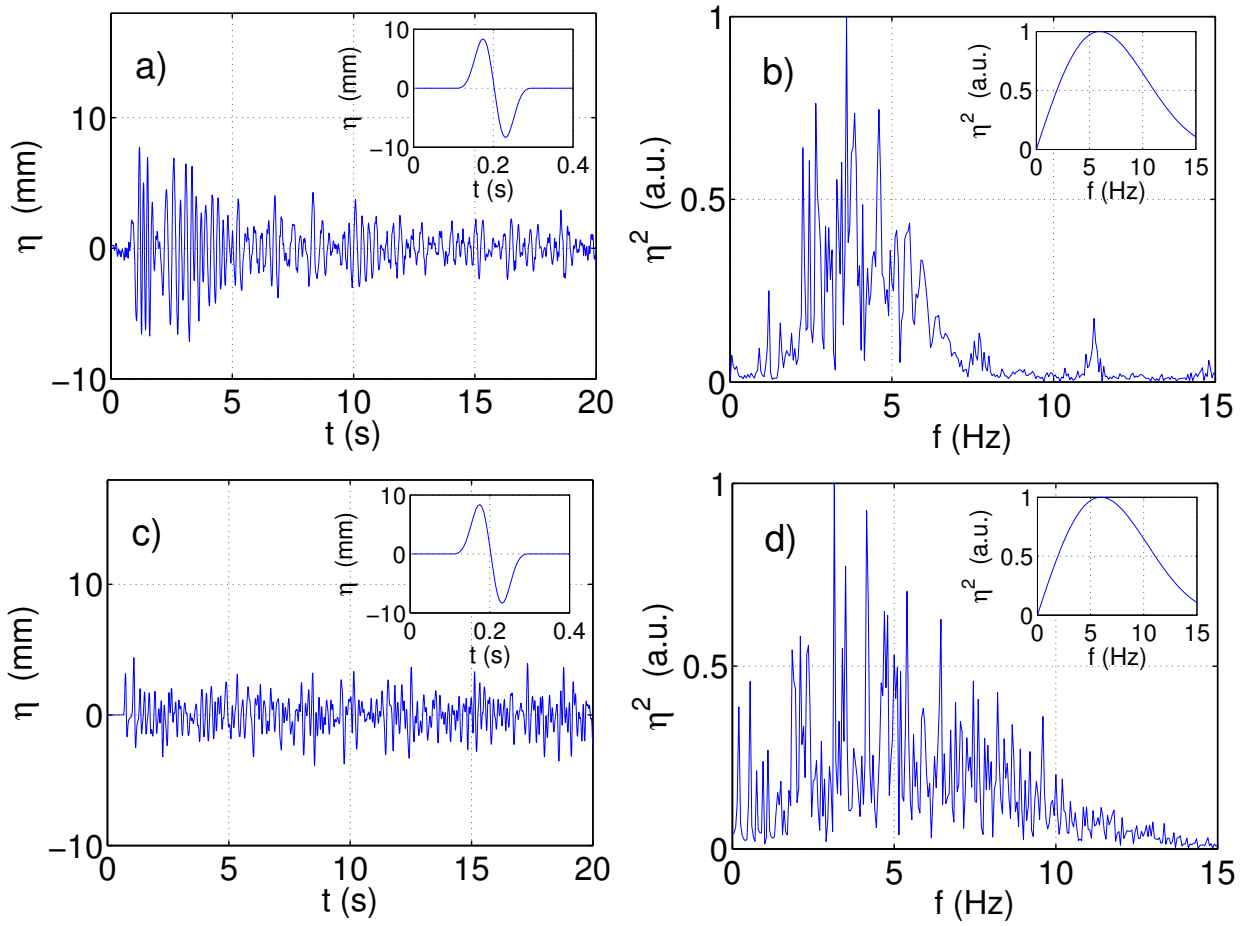

FIG. 2. (Color online). a) Experimental measurement of the temporal evolution of the surface elevation ($\eta(\mathbf{r_1}, t)$)) during the forward propagation after emission from point A. The inset shows the signal emitted from point A, b) corresponding spectrum, the inset shows the spectrum of the signal emitted from point A, c) & d): same representation from numerical simulations of the wave equation.

around 100 cavity modes excited in the whole range [0 15] Hz (Fig 2(c)-(d)).

We now investigate the refocusing. The perturbation of the surface elevation $\eta(\mathbf{r}, t)$ is measured in time and in space during the wave propagation using an optical method (FTP for Fourier Transform Profilometry) that has been adapted recently to water wave measurements [13–16]. FTP is used to measure the whole pattern of surface elevation $\eta(\mathbf{r}, t)$ at *each time* of the reverse propagation. This has been done in a one channel experiments ($N = 1$). Although the spatial refocusing and temporal recompression are visible (Fig. 3), it is not possible to distinguish the converging wavefronts before the recompression and the diverging wavefronts after recompression in this one channel experiments (for a movie, see the supplementary material).

To improve the refocusing, it is possible to increase the number of channels. In a time-reversal experiments with multiple channels, the signal emitted from the source point is recorded at N receiver points. The TR signal are then re-emitted simultaneously from the N receiver points. If the N receiver points are uncorrelated, it is meant to improve the refocusing since the wave experiences many different trajectories in the cavity. In our ex-

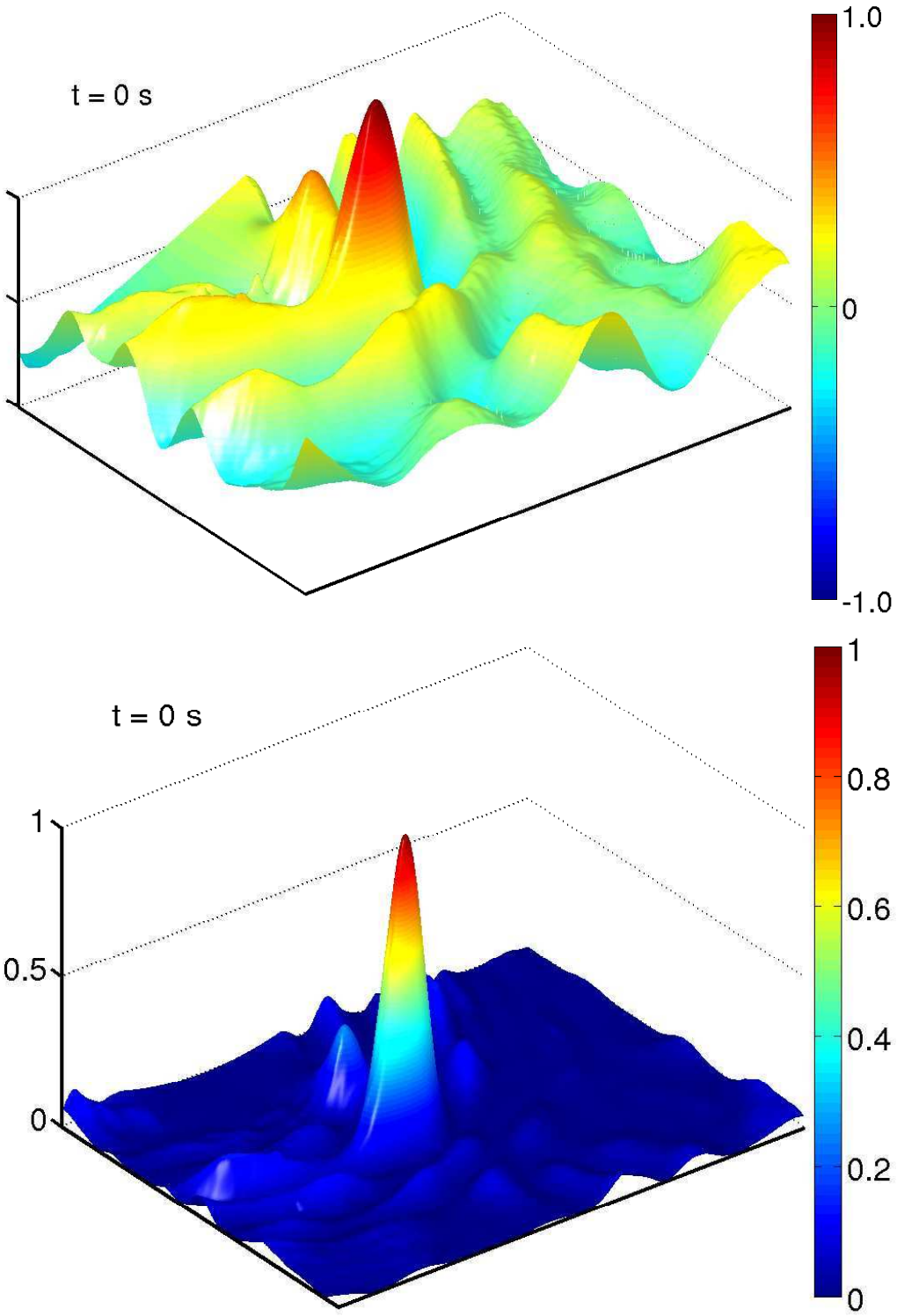

FIG. 3. (Color online). Measured amplitude ($\eta(\mathbf{r}, t = 0)$) and intensity ($\eta(\mathbf{r}, t = 0)^2$) of the time reversed wave around the initial source position (point A) where the wave is refocused at the recompression time ($t = 0$) in a one channel TR experiment ($N = 1$). The spatial range around the refocusing point A is 34×26 cm^2.

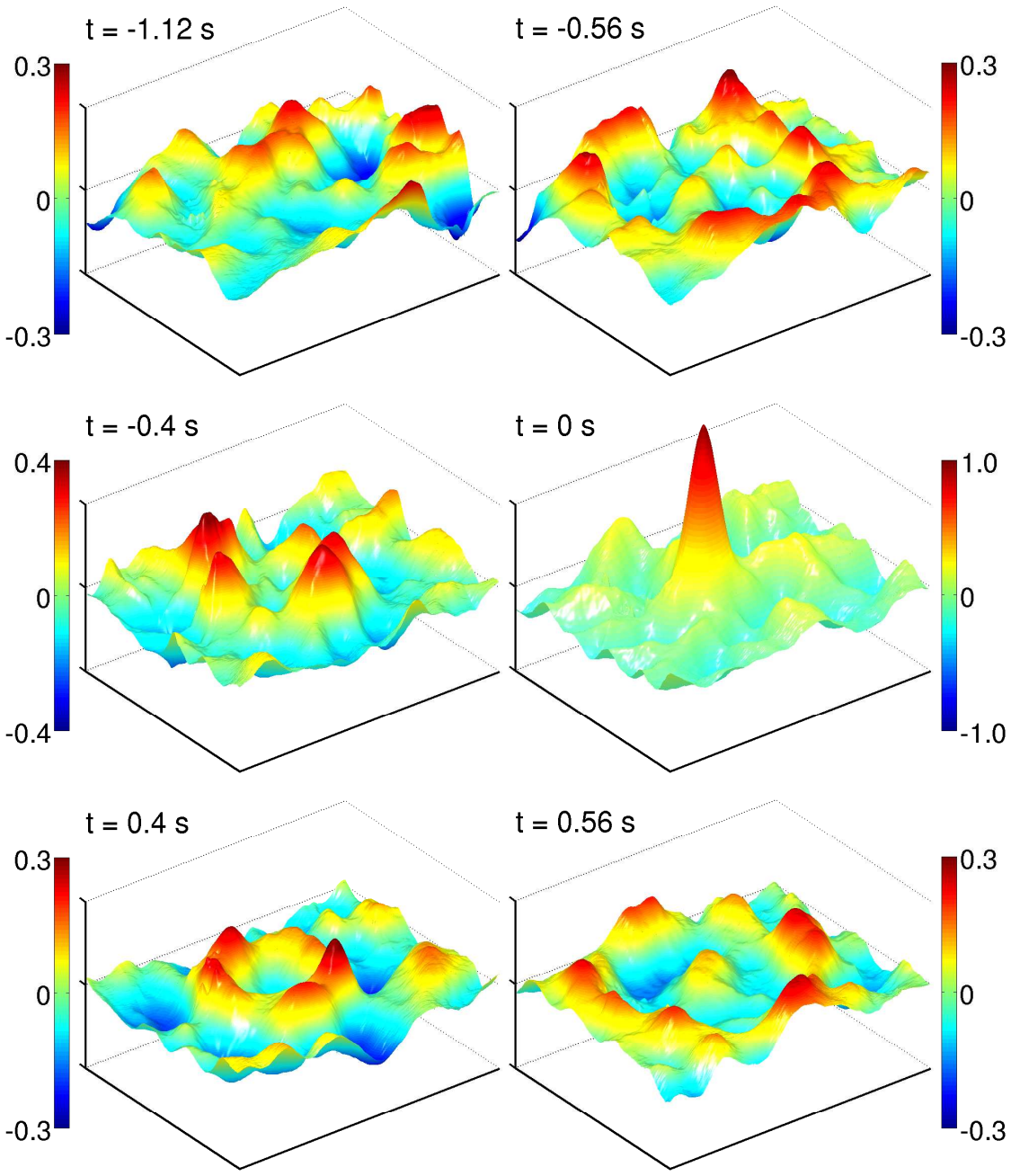

FIG. 4. (Color online). Space-time resolved experimental measurements of the surface elevation $\eta(\mathbf{r}, t)$ during the refocusing of the time reversed wave. In this case, $N = 6$ channels (points R_1 to R_6) reemit the time reversed signals. The recompression time is at $t = 0$ s. Converging and diverging wavefronts appear respectively for negative and positive time. The spatial range around the refocusing point A is 34×26 cm^2.

periment, rather than using N wave generators to reemit the signal, the N channel TR have been done with just one wave generator. This is possible by exploiting the linearity of the problem which implies that the wave field excited by N generators is equal to the sum of the N wave fields excited by each generator alone. We have checked this linearity by comparing the time signal recorded at the refocalization point when using 2 channels and when summing the two signals obtained in two single channel experiments (see supplementary material). The temporal signals in both cases coincide, with less than 10% discrepancy in a $10/f_0$ time window centered at the recompression time. Six different positions of the receiver point have been used (points R_1 to R_6 in the Fig. 1). Fig. 4 shows a time sequence of the reverse propagation for the 6 channel TR. As expected, the peak at the recompression time is much higher than in the one channel TR, confirming that the channels are uncorrelated. Besides, the converging and diverging wavefronts, before and after the recompression time are visible.

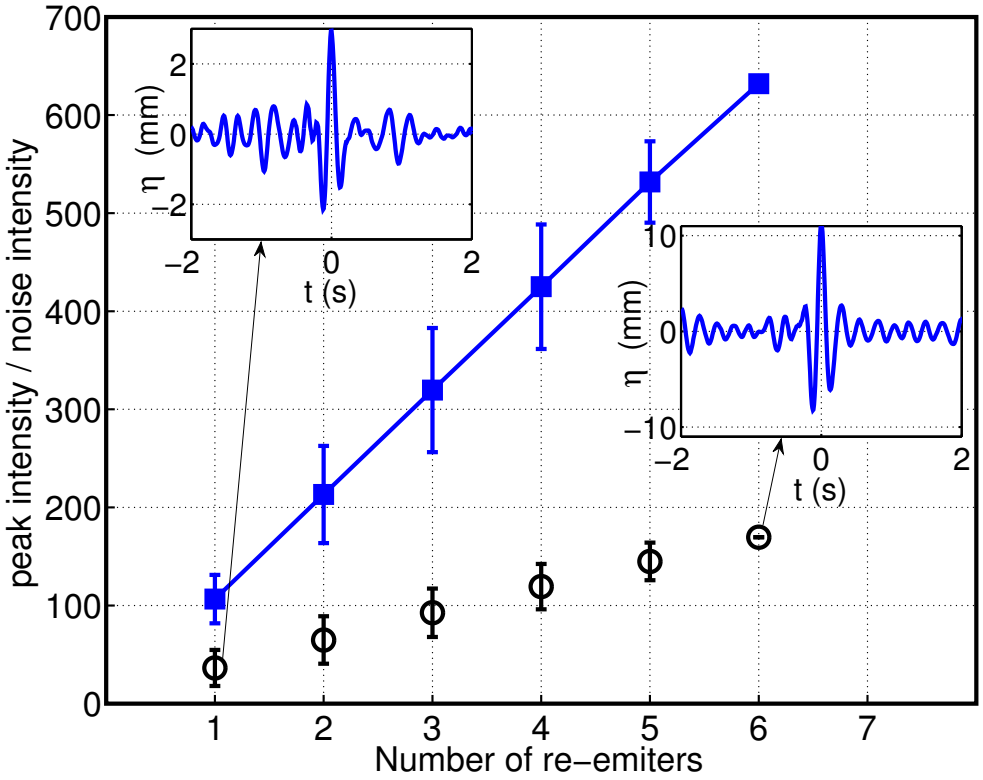

FIG. 5. (Color online). Experimentally measured peak to noise ratio as a function of the number N of channels (black points). For comparison, the blue squares show numerical results with negligible damping. Note the standard deviation accounting for the sensitivity of the refocusing to th position of the re-emission point. The insets present the experimental temporal refocalisation while using one and six channels.

To gain insights in the study of the quality of the refocusing, we want to inspect both the effect of the number of channels and the effect of the damping. To characterize the quality of the spatial refocusing, we define a peak to noise ratio (PNR) at the recompression time as the ratio of the maximum intensity at the focal spot to the mean sidelobe intensity. Experimental results are shown in Fig. 5 (black points). With a single channel, the peak to

noise ratio is typically 20, a value that is related to the number of cavity modes that can be resolved from the spectrum at the receiver point in Fig. 2. With several channels, the PNR increases linearly with the number N of channels [6]. Although this behavior is expected without damping, it was not obvious to be verified with the typical range of damping of our experiment. The insets of Fig. 5 show the temporal recompression for $N = 1$ and $N = 6$ at the refocusing point A. The refocusing is clearly visible in the one-channel time-reversal experiment but with higher temporal sidelobes than with 6 channels. Note that these temporal signals allow also to define a peak to noise ratio and we observed that PNR either defined in space or in time have roughly the same values. Varying the damping is more difficult. To perform experiments where the damping effect is negligible would necessitate much larger size of the cavity (e.g. the size of a swimming pool) because the attenuation per wavelength decreases with he frequency [17]. Therefore, numerical simulations have been used to model the case with negligible damping. The results are shown in Fig. 5 (blue square) where computations have been done by taking the same protocol as in the experiment. The same trends as in the experiment are observed: i) for $N = 1$, the PNR is equal to 100 and is given by the number of excited cavity modes that can be resolved in the spectrum in Fig. 2, ii) the PNR increases linearly with N. With about 20 excited modes in our laboratory experiments, versus the 100 modes obtained in the numerics, it appears that the refocusing can be significantly reduced because of the attenuation occurring at that laboratory scale.

Our experiments illustrate the feasibility of a few channel time-reversal refocusing for gravity-capillary waves. This has been performed in a well controlled laboratory context that allows quantitative measurements simultaneously in time and space. At this laboratory scale, with centimetric wavelengths, the quality of the refocusing is limited by the damping due to viscous effects but it is not suppressed. At larger scales, viscous damping highly decreases and numerical simulations show that the refocusing is greatly improved. Thus, this paves the way to applications in the context of water waves in the sea, with very small damping, where very high quality of refocusing is expected.

The authors thank the Agence Nationale de la Recherche for its funding under Grant No. Tourbillonde ANR-08- BLAN-0108-02.

---

[1] M. Fink, Physics Today **20**, 34 (1997).

[2] G. Lerosey, J. de Rosny, A. Tourin, A. Derode, G. Montaldo and M. Fink, Phys. Rev. Lett. **92**, 193904 (2004).

[3] M. Fink, Geophysics **71**, SI151-SI164 (2006).

[4] M. Fink, D. Cassereau, A. Derode, C. Prada, P. Roux, M. Tanter, J-L. Thomas and F. Wu, Reports on Progress in Physics **63**, 1933 (2000).

[5] C. Draeger and M. Fink, Phys. Rev. Lett. **79**, 407 (1997).

[6] C. Draeger and M. Fink, J. Acoust. Soc. Am. **105**, 611 (1999).

[7] C. Draeger and J-C. Aime and M. Fink, J. Acoust. Soc. Am. **105**, 618 (1999).

[8] J.P. Fouque and A. Nachbin, Multiscale Model. Simul. **1**, 609 (2003).

[9] R.P. Feynman, R.B. Leighton, and M. Sands (1963). The Feynman Lectures on Physics. Addison-Wesley. Volume I, Chapter 51-4.

[10] R. K. Ing and M. Fink, IEEE Transactions on Ultrasonics, Ferroelectrics, and Frequency Control **45**, 1032 (1998).

[11] M. Tanter, J.-L. Thomas, F. Coulouvrat and M. Fink, Phys. Rev. E **64**, 016602(7) (2001).

[12] P. S. Behroozi, K. Cordray, W. Griffin, and F. Behroozi, American Journal of Physics **75**, 407 (2007).

[13] recent improvements of the technique for the signal processing and the choice of the painting particles can be found respectively in : G. Lagubeau *et al.*, in preparation and A. Przadka, B. Cabane, V. Pagneux, A. Maurel and P. Petitjeans, Experiments in Fluids **52**, 519 (2012).

[14] A. Maurel, P. Cobelli, V. Pagneux and P. Petitjeans, J. Applied Optics **48**, 380 (2009), P. Cobelli, A. Maurel, V. Pagneux and P. Petitjeans, Experiments in Fluids **46**, 1037 (2009).

[15] P. Cobelli , P. Petitjeans, A. Maurel, V. Pagneux and N. Mordant, Phys. Rev. Lett. **103**, 204301 (2009).

[16] P. Cobelli, V. Pagneux, A. Maurel and P. Petitjeans, Europhys. Letter **88**, 20006 (2009), J. Fluid Mech. **666**, 445-476 (2011).

[17] M.J. Lighthill, Waves in fluids, UK: Cambridge University Press (2001).

3.5 Supplementary results

Presented refocusing for N re-emitting channels were obtained by superposition of the N wave fields generated each time by a single channel. The linearity of the system has been tested using two generators at the same time and comparing the obtained temporal focusing signal with a superposition of two temporal signals measured separately for each excitation channel. The similarity of both results is substantial (Fig. 3.3), however, the superposition seems to be more efficient. Indeed, here we approach the problem of imperfections of our system, which reduces the refocalisation quality and has not been analyzed until this point.

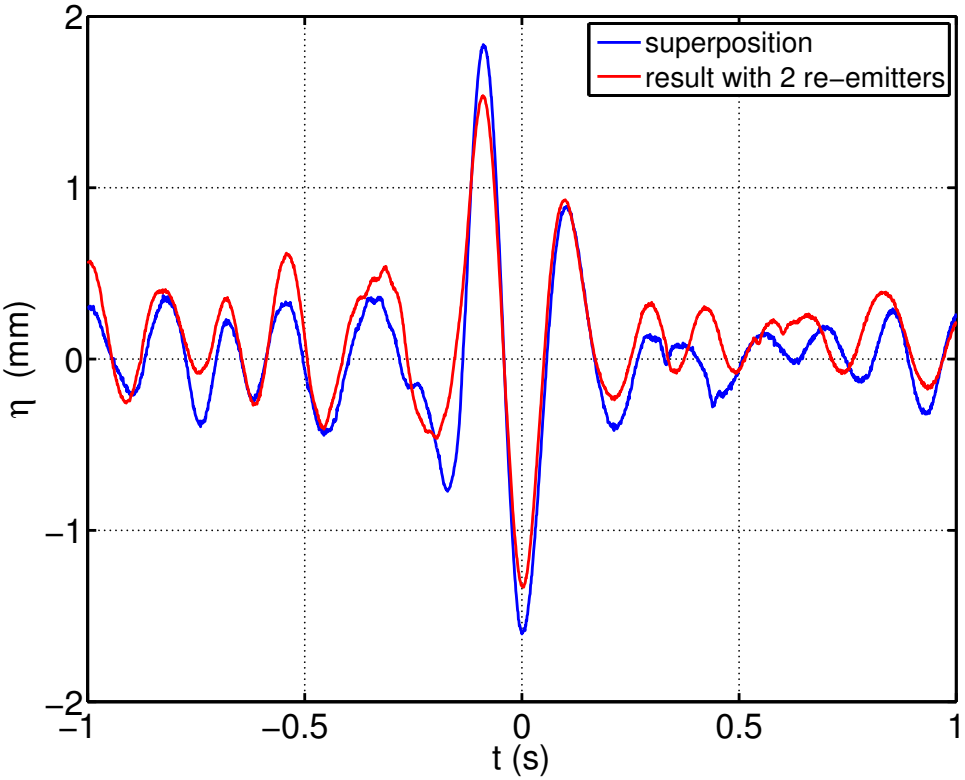

Figure 3.3: Comparison of the time signal recorded at the refocalisation point when using 2 channels (red) and when summing the two signals obtained in two single channel experiments (blue). The refocalisation quality is enhanced in the latter case.

In contrary to the acoustic time-reversal, where receiver works also like a transmitter, our re-emitting generators are obviously not present in the medium during the first step It means that, in the second step, geometry is not preserved compared to the first step! Time inversed waves would reflect not only from walls but also from the generator (that for once emitted wave would behave like an obstacle), therefore some waves that took a "good" way to the initial source position would never get there. Furthermore, while using more than one generator at the same time, waves will reflect not only from their proper generator, but also from the others, thus they will suffer more distortion than if they were sent separately one by one and

superposed. In addition, this distortion is repetitive and cannot be reduced by the averaging of many experiments. The result confirms the above line of thought (along with the system linearity) and reinforced our decision to use the superposition of one-channel signals.

The shape of refocalisation peak has also been a subject of study. Time reversed wave should redo a path which has been done by the initially injected wave, thus the shape of the peak should be comparable to the shape of the injected signal. Fig. 3.4 shows temporal elevation in the source position during a reverse propagation (blue) and compares it to the injection signal imposed during the first step of the experiment (green). It can be observed, that the reversed wave follows the original path, even when the imposed signal is broad (injected sinusoidal signal had 5 periods with central frequency equal to 5 Hz and was modulated with a Blackman window). Experiments with many-periods injection signals are a good candidate to study peak shapes, however, they excite narrow bandwidth of frequencies and in addition make it hard to analyze peak to noise spatial ratio (while observing a highest peak, some wavefronts are still converging and some are already diverging giving rise to the strong surface elevation around the main peak). After testing many signals, we found that one-period excitation functions were the most suitable experimentally.

The presented article demonstrates numerical results, however, it does not describe details of used simulation. This subject will be clarified below.

Numerical simulations concerned a simplified model of water waves and were performed for non-dispersive, linear waves. The wave equation takes a form:

$$\frac{\partial^2 U}{\partial t^2} + \Lambda \frac{\partial U}{\partial t} - c^2 \Delta U = 0, \tag{3.11}$$

where U is the scalar field, c is the wave celerity and Λ is a constant (frequency independent) absorption coefficient (set to zero for a loss-less medium). Discretizing this equation, one can reach:

$$\frac{U^{p+1} + U^{p-1} - 2U^p}{\Delta t^2} + \Lambda \frac{U^{p+1} - U^{p-1}}{2\Delta t} - c^2 \frac{\mathrm{del2}\,(U^p)}{\Delta x^2} = 0, \tag{3.12}$$

where U^p is a two-dimensional matrix modeling the field at time step p, while Δx and Δt correspond to space and time discretization respectively. The discrete Laplace operator del2 is defined for a two-dimensional array as:

$$(\mathrm{del2}\,(U))_{i,j} = (u_{i+1,j} + u_{i-1,j} + u_{i,j+1} + u_{i,j-1}) - 4u_{i,j} \tag{3.13}$$

and equal to zero on the edges (reflecting walls). The evolution equation thus yields:

$$U^{p+1} = \frac{2}{1+a} U^p - \frac{1-a}{1+a} U^{p-1} + \frac{c^2 \Delta t^2}{(1+a)\Delta x^2} \mathrm{del2}\,(U^p), \tag{3.14}$$

where $a = \frac{\Lambda \Delta t}{2}$. To satisfy the Courant-Friedrichs-Lewy condition of discrete partial differential equations, the quantity $\frac{c^2 \Delta t^2}{\Delta x^2}$ must be set below 1. Note that Λ stands for the numerical

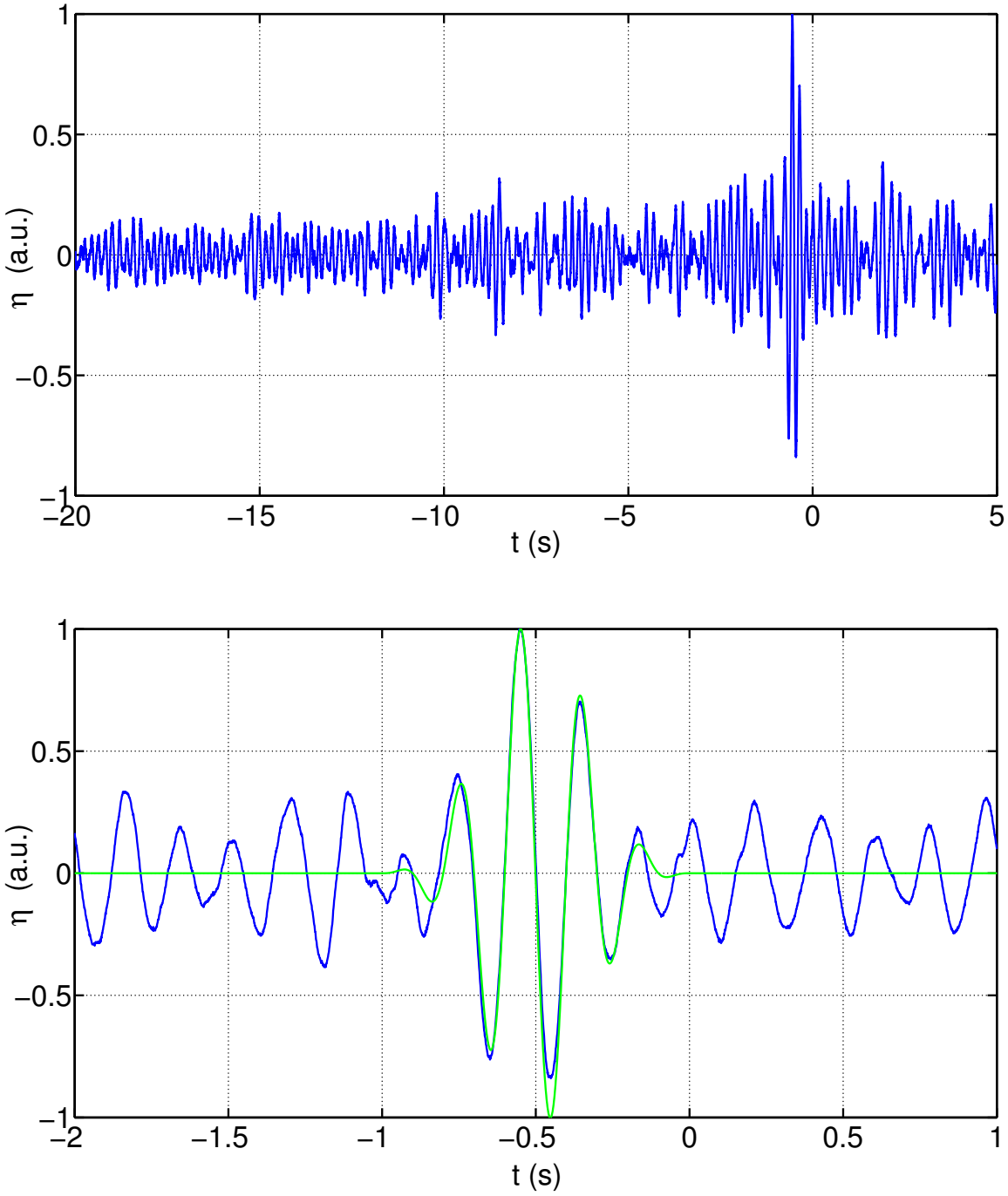

Figure 3.4: Blue line: Surface elevation measurement during the time reversed step in the source position (top) and its close-up around the recompression time $t = 0$ s (bottom). Green line indicates an excitation function used in the first step of the experiment. The undone time evolution of the reversed signal is similar to the excitation function.

dissipation coefficient and is not equal to the attenuation coefficient β (which was the subject of study in the chapter 2).

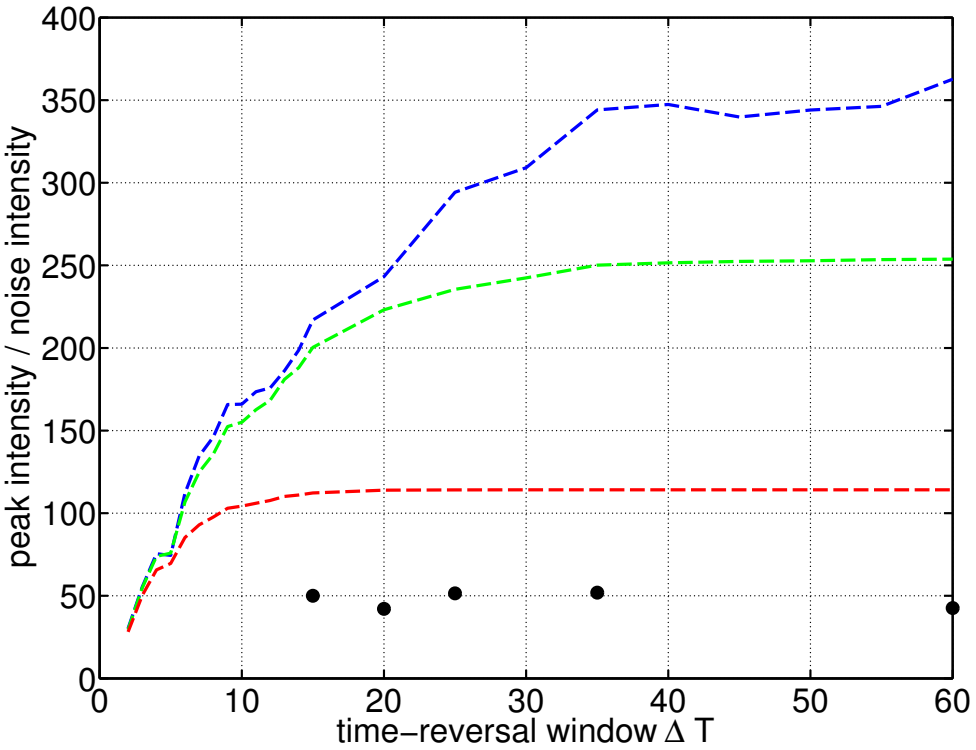

Figure 3.5: Quality of the refocusing peak in the function of time-reversal window ΔT for two-channel time-reversal experiments. Dotted lines show numerical results for non-attenuative medium (blue), for damping equal to the theoretical damping for $f = 5$ Hz (green) and $f = 8$ Hz (red). Black markers present the experimental results.

This model has been used not only to validate the strong linear increase of the peak to noise ratio in the case of non-attenuated (sea) waves, but also to present this value in the function of ΔT and compare it with experiments. Fig. 3.5 summarizes numerical and experimental results for the two-channel case. Black markers indicate the experimental results, while blue, green and red curves show the numerical results with damping set to zero and to the values equal to the theoretical damping for $f = 5$ Hz and $f = 8$ Hz. The numerical results confirm the validity of theoretical predictions presented in the Sec. 3.3. Initially linear tendency is visible, while for high ΔT the saturation is reached. The quantity ΔT for which this saturation is obtained as well as the intensity level depends strongly on the damping coefficient.

Experimental results (performed for the excitation function centered at $f_0 = 5$ Hz) do not fit the numerical predictions. It can be assumed that there are other losses of information in the system that reduce the refocalisation quality. These loses are believed to be due to the broken geometry invariance, while introducing wavemakers inside the cavity during the

reversed step of the experiment.

Despite strongly suppressed experimental refocalisation quality, it should be recalled that one-channel time-reversal refocalisation can be obtained. Fig. 3.6 shows the experimental measurements of the surface elevation $\eta(\mathbf{r}, t)$ around the refocusing point for various times, proving the success of this experimental study. Fig. 3.6 corresponds to the Fig. 4 in the presented article (for which $N = 6$ re-emitting channels were used).

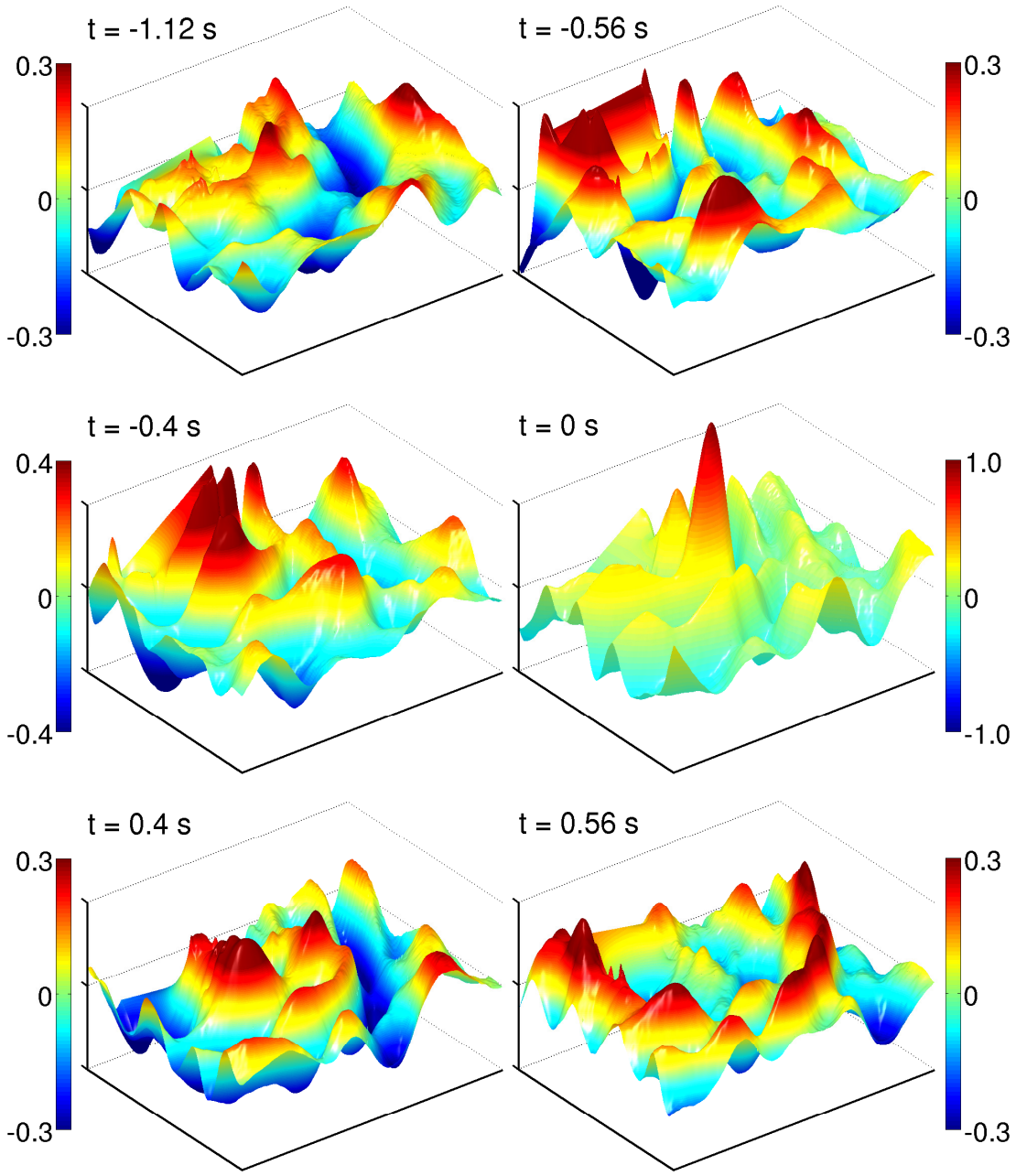

Figure 3.6: Space-time resolved experimental measurements of the surface elevation $\eta(\mathbf{r},t)$ during the refocusing of the time reversed wave. In this case, only one channel (point R_2) re-emits the time reversed signal. The recompression time is at $t = 0$ s. Converging and diverging cylindrical wavefront for negative and positive time are less visible and much more noisy than in the case of $N = 6$ channels (see Fig. 4 in the above article). Wavefronts do not come from all directions surrounding the refocalisation point. The spatial range around the refocusing point A is 34 x 26 cm^2. Amplitude is normalized with the maximum amplitude in the refocusing point at the recompression time.

CHAPTER 4

DIFFERENT REGIMES FOR WATER WAVE TURBULENCE

This chapter presents experimental results on simultaneous 3D space-time measurements (x,y,t) for gravity-capillary wave turbulence in a laboratory tank. It is composed of brief introduction into the wave turbulence (WT) and its recent studies and followed by an article published in *Physical Review Letters* [14], where behavior of wave energy density is inspected and compared to available theoretical predictions. Additionally, a more extensive exposition of the results obtained in this study is displayed in the last section.

4.1 Motivation

Turbulence is a non-equilibrium state where nonlinear processes and energy transport occur. In all turbulent systems kinetic energy is carried from the scales where it is injected down (or up) to scales where it is dissipated by viscous shear stress. In 1941 Kolmogorov made an assumption of self-similarity of the system and statistically described an energy cascade for classical 3D hydrodynamic turbulence. If we consider that the scales of energy injection and dissipation are separated, then the kinetic energy has to be distributed over the multiple scales between them (this range is called "inertial range" since inertial effects dominate over viscous effects). Dimensional analysis leads to the famous energy spectrum predictions proposed by Kolmogorov:

$$E(k) = CP^{2/3}k^{-5/3}, \tag{4.1}$$

where P stands for the energy flux, k is the wavenumber and C is a dimensionless constant. In reality, some processes occur sporadically and are not universal, thus they cannot be pre-

dicted by the averaged quantities. This gives rise to the discrepancies between theory and real turbulence observations. Such deviations from the theory are known as intermittency.

Despite the success of this model, which gives qualitative description of turbulence, it is based on scaling arguments and does not precise the exact mechanism by which the cascade occurs and furthermore it cannot describe the physics of intermittency. The lack of mathematical tractability in classical turbulence is the main constraint which limits the understanding and ability to predict its behavior. The underlying physics and the mathematical description of the problem is still an open subject and turbulence remains today one of the least understood (and at the same time, one of the most fascinating) phenomenon in physics.

4.2 Introduction

In contrast to the hydrodynamic turbulence, systems that can be described in terms of small parameters can have natural asymptotic closure and thus, can be solved mathematically. These systems allow for both linear and nonlinear interactions, but the nonlinear processes have to be weaker than the linear ones (while in hydrodynamic turbulence the nonlinear effects dominates). This kind of turbulence is called wave turbulence or weak turbulence (WT) and has been observed in many fields of physics, such as surface waves, waves in nonlinear optics [23], elastic bending waves in plates [12], Alfvén waves in solar winds [34, 63].

The power of WT comes from the fact, that the analytical solution of the kinetic equation describing WT leads to the solution which is familiar with the power law scaling of the energy density spectrum predicted by Kolmogorov for fully developed turbulence (and at the same time prescribes physical mechanism for the transfer of energy). Then, in the general context, the study of WT can be used to understand essential features of turbulence.

Our work concentrates on the WT on the surface of water. The first analytical studies on the mutual nonlinear interactions between surface waves began in the 1960's. Based on the assumption of weakly nonlinear waves with random phases propagating in the infinite system, Hasselmann derived, in 1962 [38], the kinetic equation (describing the temporal evolution of the spectral density of the wave action $n(\mathbf{k}, t)$) which reads:

$$\frac{\partial n(\mathbf{k}, t)}{\partial t} = S_{nl} + S_{in} + S_{ds}, \tag{4.2}$$

where S_{nl} represents the interaction between waves, S_{in} the energy injection and S_{ds} the energy dissipation. Zakharov and his co-workers [79, 80, 81] were first to find the finite-flux non-equilibrium solution to that equation (for the energy sources and sinks separated by the inertial range) and found the space energy cascade such as:

$$E(k) = CP^{1/(N-1)}k^{-\alpha}, \tag{4.3}$$

where all transport is carried by N-wave resonances. Thanks to the phenomenological similarities of WT with hydrodynamic turbulence this spectrum is called the Kolmogorov-Zakharov

(KZ) spectrum and the exact solution to that spectrum can be derived in many fields of physics dealing with wave dynamics (some listed above). In the case of surface water waves the gravity waves are dominated by 4-wave resonance, while capillary waves has been found to depend on 3-wave resonant interactions. The power space and frequency spectra of surface wave amplitude can be expressed as:

$$\begin{array}{ll} \left|\eta_\omega\right|^2 \propto P^{1/3}\omega^{-4}, & \left|\eta_k\right|^2 \propto P^{1/3}k^{-5/2} \quad \text{for gravity waves,} \\ \left|\eta_\omega\right|^2 \propto P^{1/2}\omega^{-17/6}, & \left|\eta_k\right|^2 \propto P^{1/2}k^{-15/4} \quad \text{for capillary waves.} \end{array} \tag{4.4}$$

4.3 Wave turbulence - a real experimental challenge

Since the first derivation of water wave turbulence, there had been many theoretical advances, however, only few experimental evidences are available. In addition, they reveal some inconsistencies with the developed theory (for recent review on WT see [62]).

These discrepancies can originate from the theoretical requirements, which are particularly difficult to meet experimentally. It is worthwhile to recall at this point the main assumptions of the WT theory. These are:

- weak-nonlinearities (small amplitudes, mild slopes).
- isotropic and homogeneous system.
- infinite size of the system.
- random waves phases.
- no fluctuations of the energy flux during the cascade through the scales.
- wave energy concentration on the renormalized linear dispersion relation, which remains close to the linear one.

Obviously, the third assumption cannot be fulfilled experimentally. This limitation has been analyzed by the group of Nazarenko [17, 54, 55]. They found the frequency energy cascade for gravity waves to be dependent on the forcing with ω-slopes varying from -6 to -4 (which is in agreement with other experimental observations [26, 28]). This effect has been attributed to the finite-size of the tank, which suppresses the resonant wave interactions, thus slowdowns the energy cascades from long to short waves. Surprisingly, they also found the space spectral exponent to be forcing dependent. They concluded that none of the existing theories can fully explain these results.

Moreover, in most cases measurements are restricted to a single-point surface elevation in time (to cite only the recent ones [17, 26, 28, 54]). In that case, the directly accessible quantity is the frequency spectrum. The space spectrum can be evaluated only via dispersion relation. The approach with a single-point measurement is highly limited and cannot bring any information about energy distribution in the ($\mathbf{k}$, ω) space. Newell and Rumpf [62] noticed a need to overcome previous experimental constraints and stated: "In particular, it would be valuable

to measure joint space-time power spectrum". This can be obtained by a measurement of surface elevation in time and in space with good lateral resolution.

Our group was first to report an experimental wave-vector-frequency ($\mathbf{k}$, ω) Fourier spectrum for wave turbulence in a case of vibrating plate [12]. The behavior of space-time wave energy density for water gravity wave turbulence has been recently published by the group of Falcon [40]. They reported that the transition from k space to ω space cannot be achieved according to the linear dispersion relation. Their work therefore, calls with question the validity of previous experimental results using this connection to change the variables. They have also shown that the energy is shared between resonant free modes and nonresonant slave modes (while its number depends on the injection power), thus the energy is not concentrated only on the linear dispersion relation manifold. Spatial spectrum exponent was found to be different than the one predicted by the theory. The isotropy of the spectra was also broken due to the forcing.

In addition to the listed theory-experiment discrepancies, none of the so far available experimental results reported consistency with theoretical energy cascade dependency from energy flux P, neither in the gravity regime, nor in the capillary regime. It is also discussed that the energy flux might have fluctuations much larger than the mean itself and furthermore, can take positive and negative values [62].

In this context, further analysis of the 3D spectra seems like a natural continuation to the previous experimental effort on understanding the physics of weak turbulence interactions, thus we used space-time resolved FTP method to study behavior of the wave energy density simultaneously in $\mathbf{k}$ and ω spaces. To have a deeper insight to the phenomenon, we report the results for two different forcing frequency bandwidths. The broad one, that could increase the intensity of the nonlinear interactions, and the narrow one, which allows one to enlarge the inertial range in the gravity regime.

The key result of this study is the determination of the 3D energy spectra. It gave a possibility to compare the results directly to the weak turbulence theory premises. These spectra were used to deduce weather the experiment is indeed weakly nonlinear - the energy density should be localized on the dispersion relation close to the linear counterpart. This has been confirmed for the narrowband experiments. The access to the Fourier space allows one also to compute independently, both, frequency and wave-vector energy spectra. Our results for narrowband experiments were found to be consistent with the theoretical predictions.

The precise determination of the statistical behavior is achieved by the calculation of the probability density function of the surface elevation velocity in the whole area of measurement. The Gaussian form is obtained for narrowband forcing, however, non-Gaussian statistics occur in the broadband one. The latter can result from third-order effects in wave field or existence of bound waves. As suggested in [74] the effects of third-order nonlinearities are suppressed due to the finite-depth effects. Indeed, bound waves have been observed for enough high forcing amplitude. This is then a poor candidate to study WT, however, for this regime the wave intensity is strong and the energy cascade can induce capillary waves, thus this broadband forcing was also a subject of our study.

The capillary range was not accessed in the previous 3D ($\mathbf{k}$, ω) space experiment presented in [40]. Here, the FTP method was also employed, but possibly white pigment with surface active materials was used, without taking into account the calming effect induced by the presence of the monomolecular slicks (the article reported surface tension on the level of 31 ± 1 mN/m, much lower than for the pure water). Indeed, as found in [1] the Marangoni damping leads to a deformation of the energy cascade and its faster dissipation. This can be a reason of inaccessibility of energy in the capillary range in the mentioned article.

The experimental study presented in the following article takes advantage of the possibility for the space-time measurement of pure water waves. The characterization of the wave-vector-frequency ($\mathbf{k}$, ω) Fourier spectrum for surface wave turbulence constitutes a significant advance on that subject and paved the way for first experimental agreement with theory for power law scaling.

Different Regimes for Water Wave Turbulence

P. Cobelli,* A. Przadka, and P. Petitjeans
Physique et Mécanique des Milieux Hétérogènes PMMH, UMR CNRS 7636–ESPCI–UPMC Univ. Paris 6–UPD Univ. Paris 7, Paris, France

G. Lagubeau and V. Pagneux
Laboratoire d'Acoustique de l'Université du Maine, UMR CNRS 6613, Avenue Olivier Messiaen, 72085 Le Mans, France

A. Maurel
Institut Langevin, LOA, UMR CNRS 7587, ESPCI, UPD Univ. Paris 7, 10 rue Vauquelin, 75231 Paris Cedex 05, France
(Received 20 July 2011; published 18 November 2011)

We present an experimental study on gravity capillary wave turbulence in water. By using space-time resolved Fourier transform profilometry, the behavior of the wave energy density $|\eta_{\mathbf{k},\omega}|^2$ in the 3D $(\mathbf{k}, \omega)$ space is inspected for various forcing frequency bandwidths and forcing amplitudes. Depending on the bandwidth, the gravity spectral slope is found to be either forcing dependent, as classically observed in laboratory experiments, or forcing independent. In the latter case, the wave spectrum is consistent with the Zakharov-Filonenko cascade predicted within wave turbulence theory.

DOI: 10.1103/PhysRevLett.107.214503 PACS numbers: 47.27.−i, 47.35.Bb

Nonlinear wave interactions are ubiquitous in all domains of physics [1]. Among these, weak nonlinear random waves are especially interesting since they are able to experience an energy cascade through different scales. This has been described in the framework of wave turbulence theory, which, in contrast to classical hydrodynamic turbulence, possesses analytical predictions for the power law scaling of the energy density spectrum [2–4]. Note also the work of [5] on the interaction of bulk hydrodynamic turbulence and free surface. There is still debate about whether the physics of ocean waves is described well by the wave turbulence theory (WT) even though this appears to fit the spectra measured for ocean waves in many cases [6,7]. To gain deeper insight into the concordance between the theory and measurements, well-controlled laboratory experiments have been developed in recent years [8–13]. These experiments have raised the question of whether or not the conditions for the applicability of WT theory can be in place in such finite systems. Indeed, this theory assumes weak nonlinearities, low attenuation, and small finite size effects, and meeting these requirements is particularly difficult in a laboratory tank [13–16].

In the present Letter, we present space-time resolved experimental results of different regimes of wave turbulence.

The joint space-time power spectrum,

$$|\eta_{\mathbf{k},\omega}|^2 \equiv \int d\mathbf{r}dt\langle\eta(\mathbf{r}', t')\eta(\mathbf{r}+\mathbf{r}', t+t')\rangle e^{i(\omega t+\mathbf{k}\cdot\mathbf{r})}, \quad (1)$$

shows how the nonlinear interactions spread the wave energy in the 3D $(\mathbf{k}, \omega)$ space. This quantity fills the gap between the k-space point of view of WT theory and the ω space which is usually more accessible in experiments (even though the link between the wave action variables used in the theory and the observable measurable quantities is not obvious [17]). Note that several attempts have previously been made to directly compute the wave number spectra [8,11,18]. The joint space-time power spectrum allows us to test the validity of the premise of WT theory that assumes the concentration of the wave energy on the renormalized dispersion relation (which remains close to the linear dispersion relation) and it allows us to evaluate the isotropy of the energy distribution. We obtained different turbulence regimes by varying the forcing frequency range $[0, \omega_m]$. In one case, the wave field is shown to be composed only of resonant free modes whose energy is concentrated on the dispersion relation and the spectra appear to be in good agreement with the Zakharov-Filonenko (ZF) spectra [19]. In the other case, the wave field is shared between the free modes and the nonresonant slave modes [17] (also called bound waves [20]) and our observations are similar to those of most of the laboratory experiments, with the existence of an inertial range that is dependent on the forcing amplitude [10,12,13].

In our experiments, water waves are generated by two piston-type wave makers (20 cm large and 1 cm immersed) in a (177×61) cm^2 tank filled with water with depth at rest $h_0 = 5$ cm. The wave maker motions are controlled by a random signal within a broadband frequency range $[0, \omega_m]$ with maximum amplitude A. We use excitations with typically A between 1 and 30 mm and $\omega_m = 25.1$ s^{-1} (4 Hz, the experiment is hereafter referred to as experiments I) and $\omega_m = 9.44$ s^{-1} (1.5 Hz, hereafter experiments II). Note that the transition between gravity and capillary waves corresponds to a wave number $k_c \equiv \sqrt{\rho g/\gamma} = 369$ m^{-1} ($\omega_c = 85$ s^{-1}).

Waves were measured by an optical method (Fourier transform profilometry) that we recently adapted for free surface characterization [21,22] and previously used in the context of wave turbulence in an elastic plate [23] (see also [24]). A full space-time characterization of the velocity field is performed. In the direct space, our spatial resolutions in both directions are the size of the projected pixel (0.2 or 0.4 mm in our experiments) and the temporal resolution is $1/F$, with F the acquisition frequency of the high-speed camera ($F = 250$ Hz in experiments I and 40 Hz in experiments II). The inspected field is 45×45 cm^2, with 968^2 pixels and the measurements are performed over 6000 successive time steps. The resulting resolutions in the spectral space are $\Delta k = 4.44\pi$ m^{-1} and $\Delta\omega = 0.42$ or 2.61 s^{-1} (with 600 successive time steps in order to permit 10 averages). Finally, the accessible range of wave numbers is limited by the phase demodulation by $k/2\pi < 1/\lambda_F = 200$ m^{-1}, with λ_F the wavelength of the projected fringes. The sensitivity is improved by treating the phase shifts between two successive images (rather than the phase shift with a reference to unperturbed free surface), resulting in the measurement of the velocity of the surface elevation $\dot{\eta}(\mathbf{r}, t)$. Typical fields and the corresponding renormalized probability density functions are shown in Fig. 1 for both experiments I and II. In order to evaluate if it is close to a Gaussian distribution [25], we calculate the skewness $S \equiv \langle \dot{\eta}(\mathbf{r})^3 \rangle / \sigma^3$ and the kurtosis $K \equiv \langle \dot{\eta}(\mathbf{r})^4 \rangle / \sigma^4$ [with $\sigma \equiv \sqrt{\langle \dot{\eta}(\mathbf{r})^2 \rangle}$ the variance]. In experiments I, the field is typically non-Gaussian with $S = 0.15$ and $K = 3.54$. On the other hand, in experiments II, it is fairly Gaussian with $S = 0.023$ and $K = 2.95$. This makes *a priori* experiments II a better candidate to satisfy the assumption of WT theory, but the full space-time characterization of the fields will give us deeper insight into the differences between the two experiments.

We first report the results obtained for experiments I, where the forcing is between 0 and 4 Hz. The space-time power spectra of the velocity $|\dot{\eta}_{\mathbf{k},\omega}|^2$ (and $|\dot{\eta}_{\mathbf{k},\omega}|^2 = |\eta_{\mathbf{k},\omega}|^2/\omega^2$) are computed by a multidimensional Fourier transform [Eq. (1)]. The isotropy of $|\dot{\eta}_{\mathbf{k},\omega}|^2$ in the (k_x, k_y) space is illustrated in inset (ii) of Fig. 2 (and it has been checked that the isotropy is preserved at all frequencies. By averaging over the direction θ_k of $\mathbf{k}$, one obtains the wave energy spectrum $|\eta_{k,\omega}|^2 = \int d\theta_k k |\eta_{\mathbf{k},\omega}|^2$ (main plot of Fig. 2), where the wave energy appears to be mainly concentrated on the linear dispersion relation $\omega(k)$,

$$\omega^2(k) = gk \tanh(kh_0)(1 + \gamma k^2/\rho g). \tag{2}$$

Nevertheless, as shown in inset (i) of Fig. 2, the wave energy is shared between the resonant part of the wave field on the linear dispersion relation $\omega(k)$ and a nonresonant part composed of slave modes (with $\omega \to N\omega$, $k \to Nk$) [17]. These latter modes, also called bound waves,

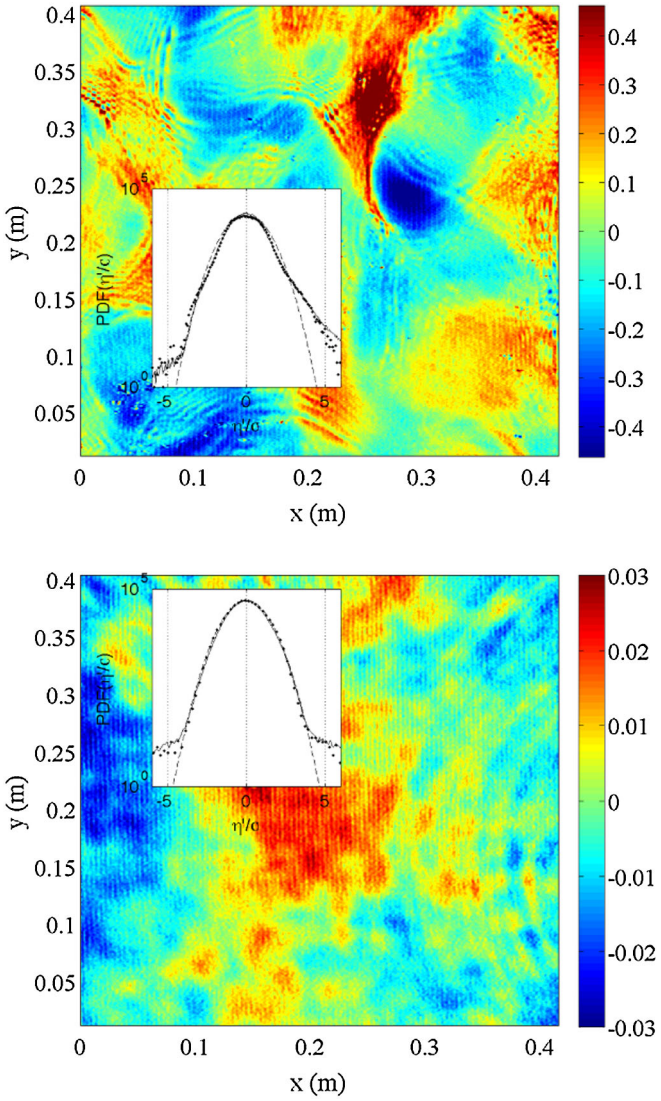

FIG. 1 (color online). Typical instantaneous velocity fields $\dot{\eta}(\mathbf{r}, t)$ (color scale is in m/s). Top: Experiments I ($A = 22$ mm), the variance $\sigma \equiv \sqrt{\langle \dot{\eta}(\mathbf{r})^2 \rangle} = 0.16$ m/s, skewness $S \equiv \langle \dot{\eta}(\mathbf{r})^3 \rangle / \sigma^3 = 0.15$ and kurtosis $K \equiv \langle \dot{\eta}(\mathbf{r})^4 \rangle / \sigma^4 = 3.54$. Bottom: Experiments II ($A = 28$ mm), $\sigma = 0.012$ m/s, $S = 0.023$, $K = 2.95$. The insets show the probability density functions of the normalized wave velocity $\dot{\eta}(\mathbf{r})/\sigma$: circles for the presented field, solid line when averaged over six fields at different times, and dotted line the Gaussian fit with mean zero and unit variance.

have already been observed numerically [16] and experimentally [11,20].

The (k, ω) power spectra give the usual energy density spectra $|\eta_\omega|^2 = \int dk |\dot{\eta}_{\mathbf{k},\omega}|^2/\omega^2$ and $|\dot{\eta}_k|^2 = \int d\omega |\dot{\eta}_{\mathbf{k},\omega}|^2$. WT theory for water waves predicts spectra for gravity waves,

$$|\eta_\omega|^2 \propto P^{1/3}\omega^{-4}, \qquad |\eta_k|^2 \propto P^{1/3}k^{-5/2}, \tag{3}$$

and for capillary waves,

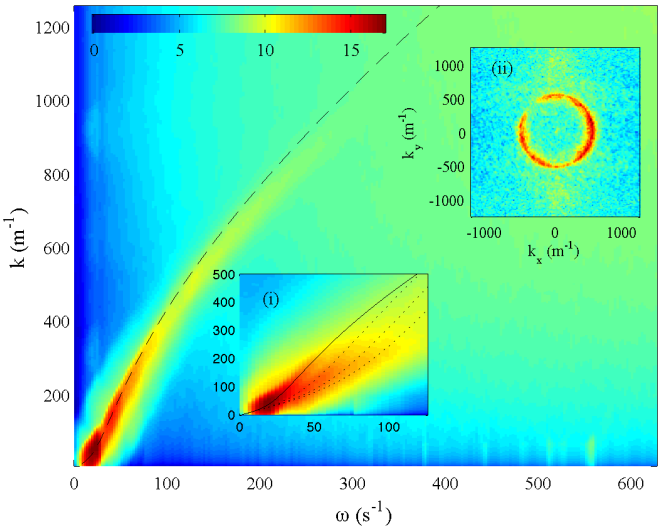

FIG. 2 (color online). Experiments I: Typical spectrum $|\eta_{k,\omega}|^2$ at low forcing ($A = 3$ mm). Inset (i) shows a zoom of $|\eta_{k,\omega}|^2$ in the gravity wave regime at high forcing ($A = 22$ mm). The solid line shows the linear dispersion relation $\omega(k)$ and the dotted lines the dispersion relation of the slave modes $N = 2, 3, 4$. Inset (ii) illustrates the isotropy in the (k_x, k_y) space by plotting $|\eta_{\mathbf{k},\omega}|^2$ for $\omega = 138$ s^{-1} ($A = 3$ mm).

$$|\eta_\omega|^2 \propto P^{1/2}\omega^{-17/6}, \qquad |\eta_k|^2 \propto P^{1/2}k^{-15/4}, \qquad (4)$$

where P is the injected energy. Figure 3 displays the energy density spectra for experiments I. The inertial ranges for capillary waves ($k > k_c$) are forcing independent, with a spectral slope close to the $-17/6$ value predicted by WT [Eq. (4)]. For gravity waves ($k < k_c$), the spectral slope is forcing dependent, with values from -6 to -5 when increasing the forcing amplitude. Our results are consistent with most of the results of laboratory experiments: indeed, similar tendency, with increasing spectral slope values when increasing the forcing amplitude, has been observed recently by several authors [10,12,13].

As suggested in [16], it is attractive to make the low frequency forcing bandwidth as narrow as possible to try (i) to enlarge the inertial range in the gravity regime and (ii) to reduce the strong nonlinearities produced near the injection scale. Therefore, we reduce the frequency bandwidth in the series of experiments II with the maximum frequency $\omega_m = 9.4$ s^{-1}.

Figures 4 and 5 show the same quantities as for experiments I (Figs. 2 and 3). Clear differences between the two wave systems appear: the most significant is the existence of a forcing independent inertial range with scaling laws in agreement with the ZF predictions $|\eta_\omega|^2 \propto \omega^{-4}$. The spectra in the k space are shown in the inset of Fig. 5, where the ZF prediction $|\dot{\eta}_k|^2 \propto k^{-3/2}$ is displayed for comparison.

Another clear different feature is the absence of nonlinear branches in Fig. 4, where nonlinear shifts with respect to the linear dispersion relation are not measurable. That means that the wave fields are only composed of resonant harmonics that cascade through smaller scales remaining on the dispersion relation manifold.

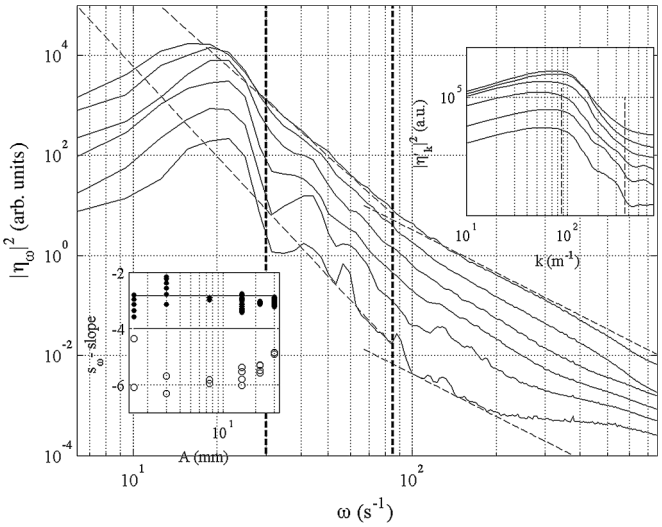

FIG. 3. Spectra $|\eta_\omega|^2$ in experiments I for $A = 1.5$, 3, 7.5, 15, 22, and 30 mm. Vertical dotted lines at 30 s^{-1} and at $\omega_c = 85$ s^{-1} delimitate the inertial range of the gravity regime. Top inset: Corresponding spectra $|\dot{\eta}_k|^2$. Bottom inset: Spectral exponent as a function of A; open circles in the gravity regime and plain circles in the capillary regime (multiple symbols correspond to multiple fits in a moving window within the inertial range).

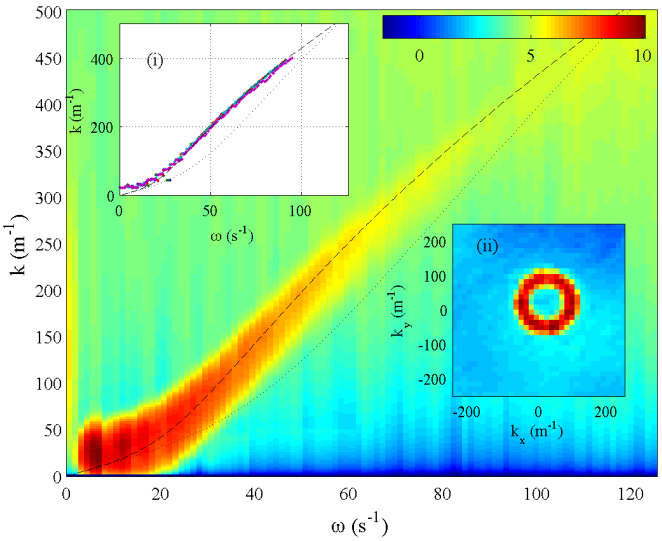

FIG. 4 (color online). Experiments II: Typical spectrum $|\eta_{k,\omega}|^2$ at forcing amplitude $A = 20$ mm. Inset (i) shows the collected dispersion relations for $A = 1$, 6, 12, 20, and 28 mm. The dashed line shows the linear dispersion relation and the dotted line the first nonlinear mode. Inset (ii) illustrates the isotropy in the (k_x, k_y) space by plotting $|\eta_{\mathbf{k},\omega}|^2$ for $\omega = 27.64$ s^{-1}.

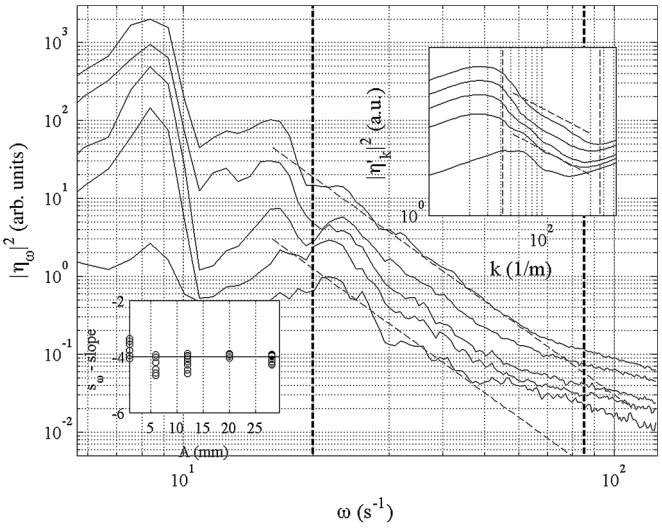

FIG. 5. Experiments II: Spectra $|\eta_\omega|^2$. Same representation as in Fig. 3 (only the gravity regime is accessible in these experiments).

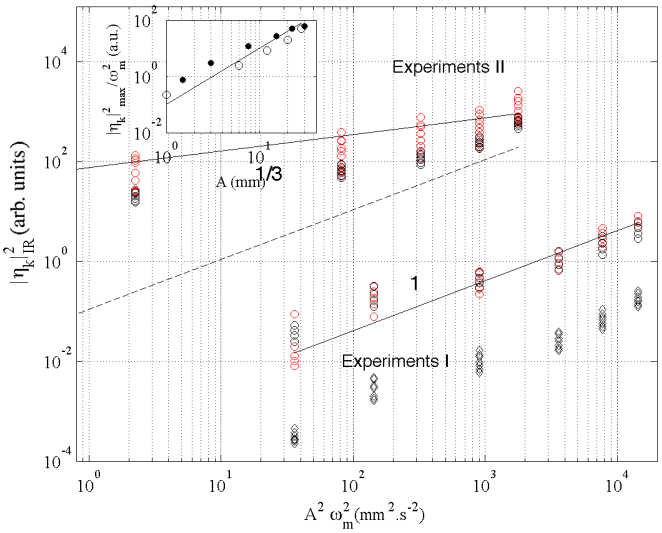

FIG. 6 (color online). Scaling laws of $|\eta_k|^2$ in the inertial range as a function of the forcing amplitudes $\omega_m^2 A^2 \propto P$. Black symbols come from $|\dot{\eta}_k|^2$ and gray (red) symbols are deduced from $|\dot{\eta}_\omega|^2 d\omega/dk$ with $d\omega/dk$ determined from the linear dispersion relation. In experiments I, results are shown for both the gravity (circles) and capillary (diamond) regimes, and in experiments II, for the gravity regime. Solid and dotted lines have slope 1 and 1/3. The inset shows $|\eta_k|^2_{max}/\omega_m^2$ as a function of A (solid line has a slope 2), suggesting that the injected power is proportional to A^2 in our experiments.

WT theory [Eqs. (3) and (4)] predicts power laws in ω and k as previously discussed and also power laws in the injected power P. A direct measurement of P can be done in decaying turbulence, as in [12]. Otherwise, an estimate is given by the scaling $P \propto \omega_m^2 A^2$ obtained in [10]. Another estimate is the maximum of the energy spectrum $|\eta_k|^2_{max}$ that is shown to be proportional to $\omega_m^2 A^2$ in the inset of Fig. 6; therefore, we use this latter estimate for P. Figure 6 shows typical values of the spectral amplitudes in the inertial ranges $|\eta_k|^2_{IR}$ as a function of P for both experiments I and II. In experiments I, we observe the same behavior as in previous experiments of the literature [10], with a linear power law with respect to P, both in the gravity and in the capillarity regimes. More interestingly, in experiments II, the power law with $P^{1/3}$ is a better fit than the power law with P^1, in agreement with WT theory.

Our work exemplifies the complexity of determining the parameters relevant to describe the weak or strong nonlinearities of turbulent wave fields in finite systems as used in laboratory experiments. Evidently, the loss of sensitivity to k-space discreteness and the associated resonance broadening necessary for the approximate four free waves interaction are expected to occur for large wave intensities. On the other hand, at large wave intensities, the appearance of bound modes may produce deviations with respect to the WT theory. In our experiments, we have changed the wave intensity for two forcing frequency ranges, and we observed two different regimes of wave turbulence. In experiments I, with broader forcing bandwidth, the presence of bound waves at large intensities indeed produce a deviation with respect to WT theory, but decreasing the wave intensity to eliminate the bound waves does not permit us to approach the WT prediction. In experiments II, with narrow forcing bandwidth, no bound waves are generated for the intensities accessible experimentally, and the wave system appears to be in good agreement with WT theory, but we have not been able to further increase the wave intensity to see the appearance of bound waves. The difference between these two regimes remains an open question. Further works are needed to better understand the transition between both regimes, for instance, by changing continuously the forcing frequency bandwidth.

The authors thank the Agence Nationale de la Recherche for its funding under Grant No. Tourbillonde ANR-08-BLAN-0108-02.

*Present address: Departamento de Fisica, FCEN, UBA and IFIBA, CONICET, Ciudad Universitaria, 1428 Buenos Aires, Argentina.

[1] G. B. Whitham, *Linear and Nonlinear Waves* (John Wiley & Sons, New York, 1974).
[2] V. E. Zakharov, V. S. Lvov, and G. Falkovich, *Kolmogorov Spectra of Turbulence* (Springer-Verlag, Berlin, 1992).
[3] S. Nazarenko, *Wave Turbulence*, Lecture Notes in Physics Vol. 825 (Springer, New York, 2011).
[4] A. C. Newell and B. Rumpf, Annu. Rev. Fluid Mech. **43**, 59 (2011).
[5] R. Savelsberg and W. van de Water, Phys. Rev. Lett. **100**, 034501 (2008).

[6] V. E. Zakharov, Direct and Inverse Cascades in the Wind-Driven Sea, http://math.arizona.edu/~zakharov/1Articles/Cascades.pdf.
[7] L. Cavaleri *et al.* (WISE Group), Progr. Oceanogr. **75**, 603 (2007).
[8] W. B. Wright, R. Budakian, and S. J. Putterman, Phys. Rev. Lett. **76**, 4528 (1996).
[9] G. V. Kolmakov *et al.*, Phys. Rev. Lett. **93**, 074501 (2004).
[10] E. Falcon, C. Laroche, and S. Fauve, Phys. Rev. Lett. **98**, 094503 (2007); E. Falcon, Discrete Contin. Dyn. Syst., Ser. B **13**, 819 (2010).
[11] E. Herbert, N. Mordant, and E. Falcon, Phys. Rev. Lett. **105**, 144502 (2010).
[12] P. Denissenko, S. Lukaschuk, and S. Nazarenko, Phys. Rev. Lett. **99**, 014501 (2007).
[13] S. Lukaschuk, S. Nazarenko, S. McLelland, and P. Denissenko, Phys. Rev. Lett. **103**, 044501 (2009); S. Nazarenko, S. Lukaschuk, S. McLelland, and P. Denissenko, J. Fluid Mech. **642**, 395 (2009).
[14] E. Kartashova, *Nonlinear Resonance Analysis* (Cambridge University Press, Cambridge, England, 2010).
[15] E. Kartashova, S. Nazarenko, and O. Rudenko, Phys. Rev. E **78**, 016304 (2008); V. S. Lvov and S. Nazarenko, Phys. Rev. E **82**, 056322 (2010).
[16] Y. V. Lvov, S. Nazarenko, and B. Pokorni, Physica (Amsterdam) **218D**, 24 (2006).
[17] V. E. Zakharov, Phys. Scr. **T142**, 014052 (2010).
[18] P. A Hwang *et al.*, J. Phys. Oceanogr. **30**, 2753 (2000); D. W. Wang and P. A. Hwang, J. Atmos. Ocean. Technol. **21**, 1936 (2004); M. V. Kosnik and V. A. Dulov, Meas. Sci. Technol. **22**, 015504 (2011).
[19] V. E. Zakharov and N. N. Filonenko, Sov. Phys. Dokl. **11**, 881 (1967); J. Appl. Mech. Tech. Phys. **8**, 37 (1971).
[20] W. J Plant, J. Geophys. Res. **109**, C10002 (2004); H. E. Krogstad and K. Trulsen, Ocean Dynam. **60**, 973 (2010).
[21] A. Maurel, P. Cobelli, V. Pagneux, and P. Petitjeans, Appl. Opt. **48**, 380 (2009); P. Cobelli, A. Maurel, V. Pagneux, and P. Petitjeans, Exp. Fluids **46**, 1037 (2009).
[22] Recent improvements of the technique for the signal processing and the choice of the painting particles can be found in G. Lagubeau *et al.* (to be published) and A. Przadka *et al.* (to be published).
[23] P. Cobelli *et al.*, Phys. Rev. Lett. **103**, 204301 (2009).
[24] P. Cobelli, V. Pagneux, A. Maurel, and P. Petitjeans, Europhys. Lett. **88**, 20006 (2009); J. Fluid Mech. **666**, 445 (2011).
[25] Y. Choi *et al.*, Phys. Lett. A **339**, 361 (2005).

4.5 Supplementary results

The presented results show forcing dependent spectra for the gravity range in the case of broad bandwidth. Since these results are obtained experimentally, it should be useful to check if it is not the effect of the wave generation. By measuring the amplitude of the wavemaker's motion, we can obtain frequency spectra injected to the system. Fig. 4.1 shows such spectra for different forcing amplitudes. The observed injected energy spectra (blue lines) are close to the expected one (red line), for the whole range of used amplitudes. Similar results, confirming the correctness of experimental wave intensity injection, have been obtained for fixed amplitude while varying frequency bandwidth (Fig. 4.2). The observed spectra do not inject unintended frequencies.

The additional material on the evolution of the energy distribution in the wavenumber-frequency domain in the function of forcing amplitude should be given also along with the one presented in the article. In the Fig. 4.3 and 4.4 this evolution is presented for narrowband and broadband forcing, respectively. As stated in the article, for the narrowband forcing the energy is distributed close to the linear dispersion manifold. The increase of the forcing amplitude results only in the broadening of the energy distribution. For broadband forcing, the nonlinear branches appear firstly only in the low frequency region, and expands with increasing forcing amplitude. It has to be recalled, that even for the low forcing amplitudes, where the energy seems to be localized close to the linear dispersion relation (meeting the requirement of the theory), the gravity spectra do not agree with the WT predictions.

As discussed in the conclusions in the above article, the understanding of the differences between both regimes might be obtained by continuously changing the frequency bandwidth. First experimental investigations were performed to explain this effect. Fig. 4.5 and 4.6 show space energy cascade for surface velocity deformation and frequency energy cascade for surface deformation. The forcing frequency bandwidth varies from [0, 1] Hz to [0, 5] Hz. Both figures give similar conclusions. The transition from the spectra, which are in agreement with theory, is not rapid, but rather smooth. It indicates that the effects responsible for discrepancies with the theory are gradually involved in our system, however, the physical explanation of that effect cannot be yet given.

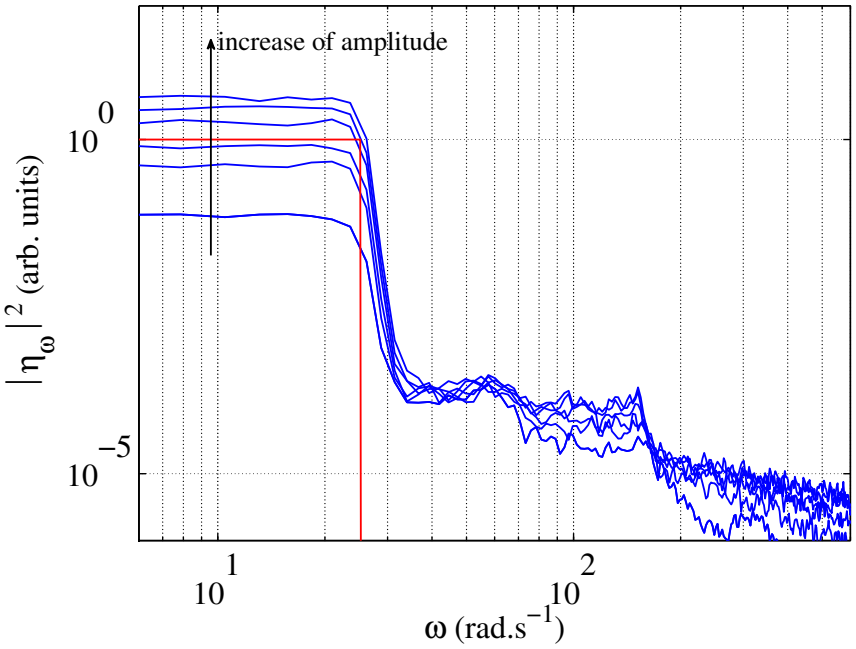

Figure 4.1: Frequency spectra injected by the wavemaker for different amplitude values (blue lines). Red line indicates the frequency spectrum of the signal imposed to the wavemaker.

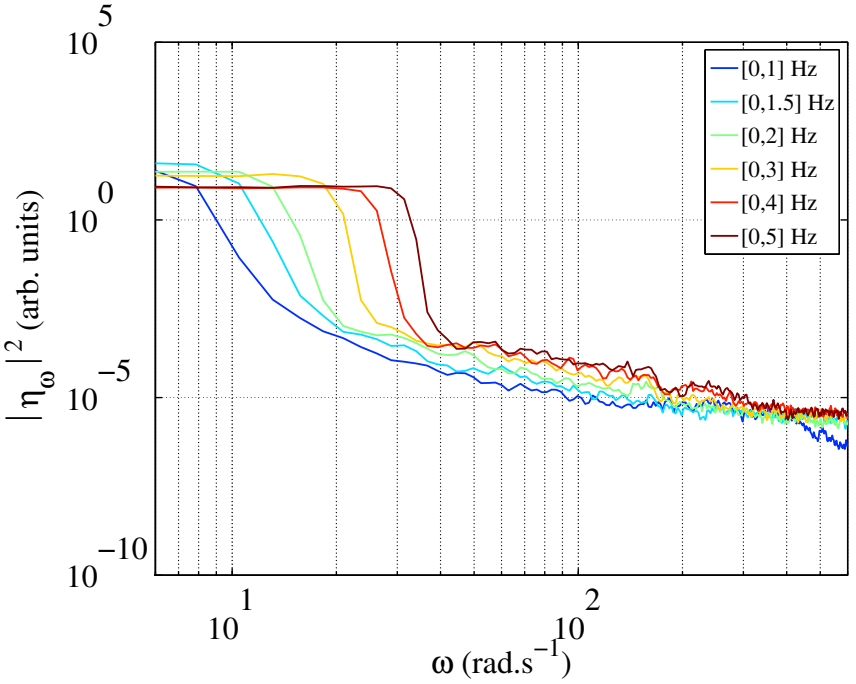

Figure 4.2: Frequency spectra injected by the wavemaker for different forcing frequency bandwidth values. The spectra are calculated from the temporal displacement of the wavemaker.

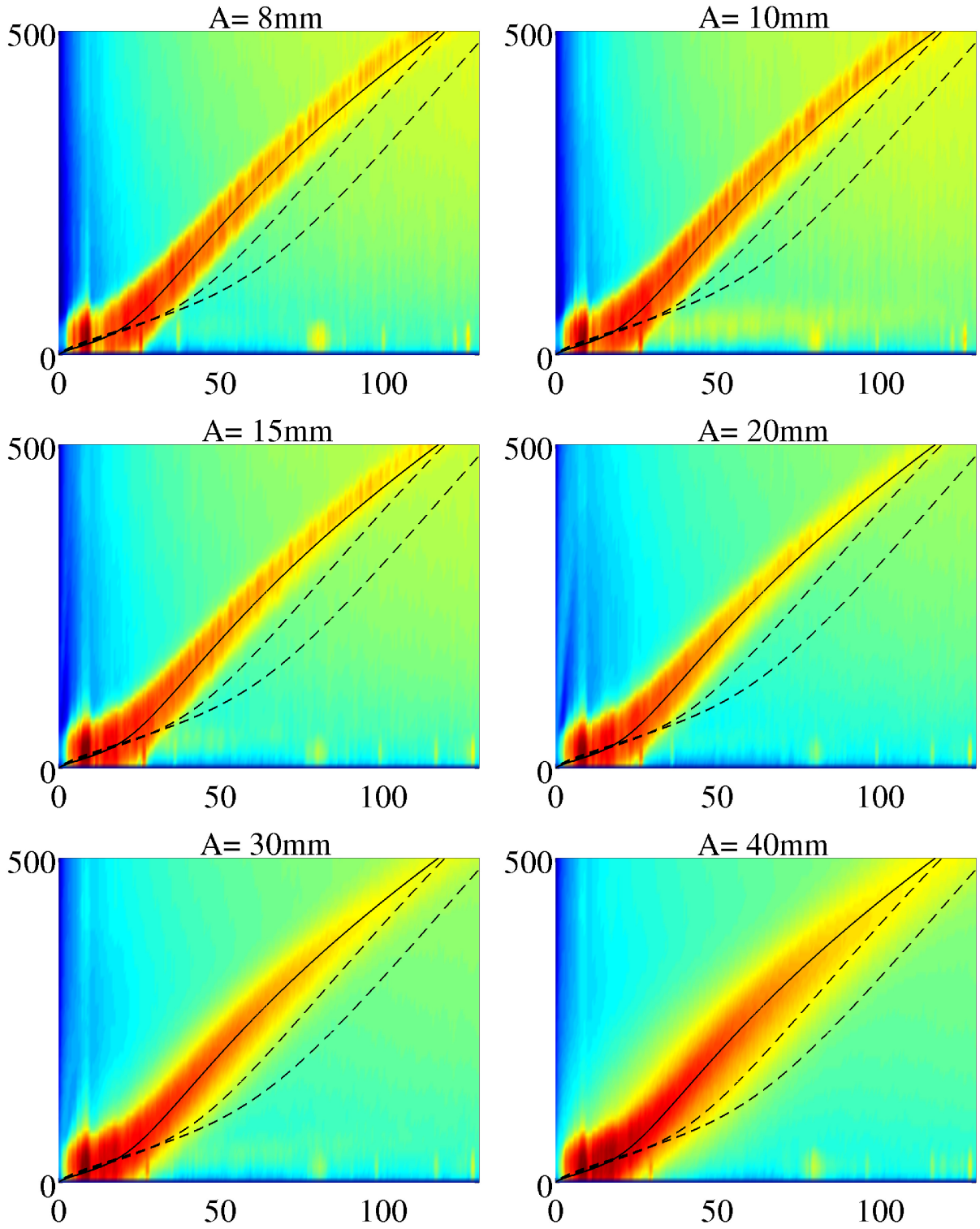

Figure 4.3: Spectra $\left|\eta_{k,\omega}\right|^2$ for narrowband forcing for different forcing amplitudes A. Solid line shows the linear dispersion relation and the dashed lines the dispersion relation for slave modes (2,3). Horizontal axis shows frequency ω (rad/s) and vertical axis - wavenumber k (1/m).

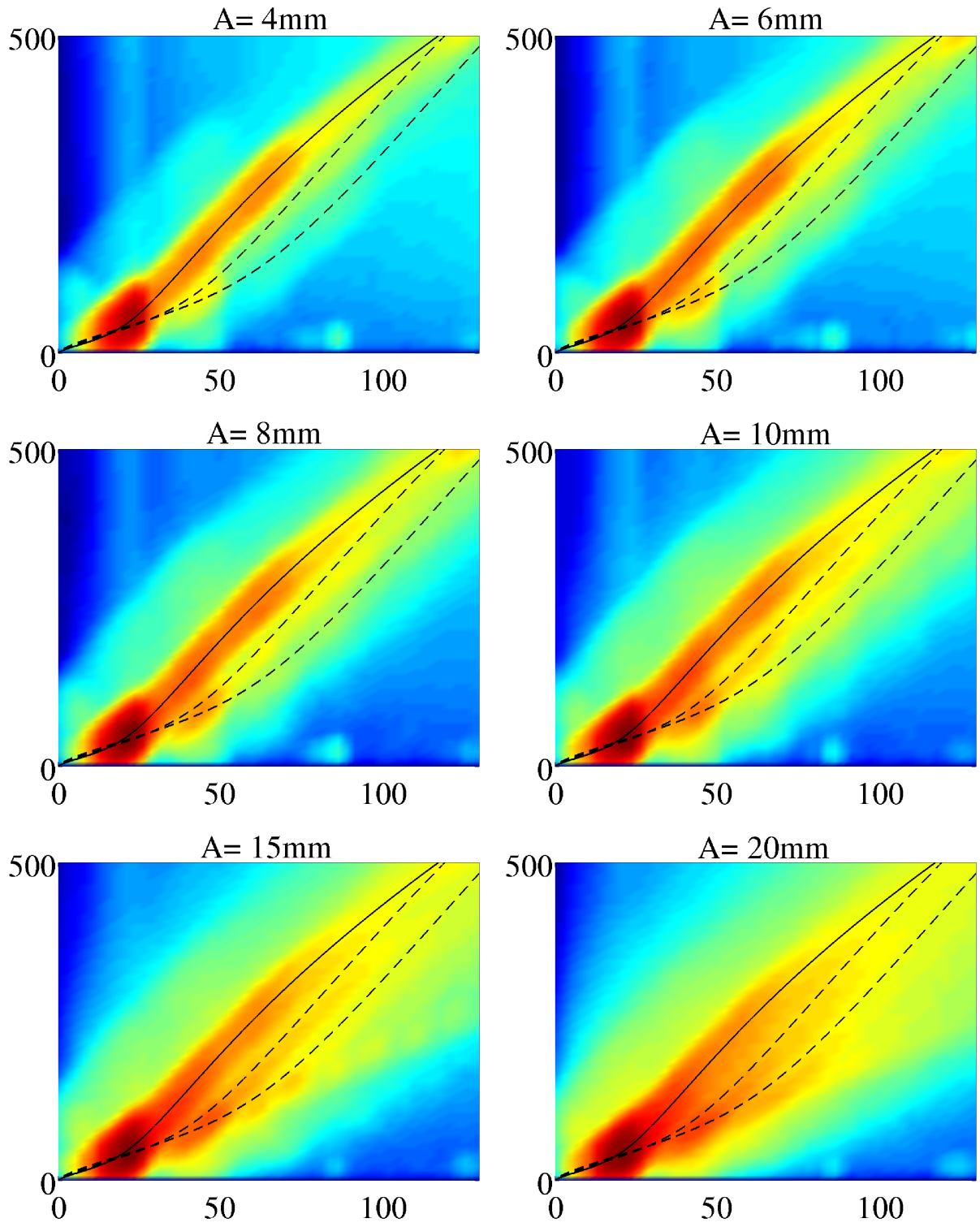

Figure 4.4: Spactra $\left|\eta_{k,\omega}\right|^2$ for narrowband forcing for different forcing amplitudes A. Solid line shows the linear dispersion relation and the dashed lines the dispersion relation for slave modes (2,3). Horizontal axis show frequency ω (rad/s) and vertical axis - wavenumber k (1/m).

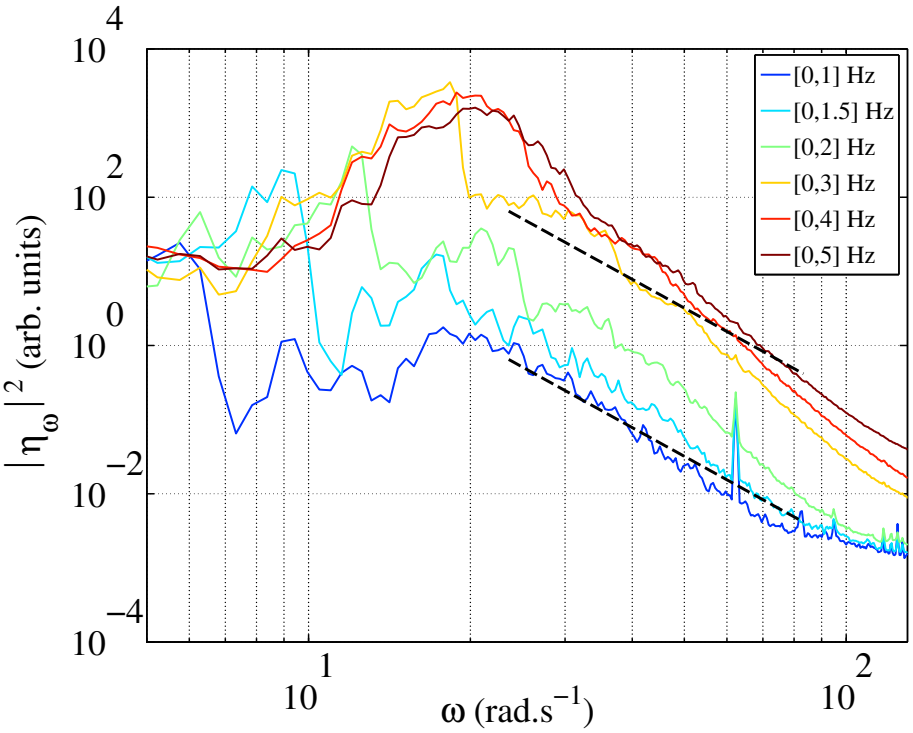

Figure 4.5: Spectra $|\eta_\omega|^2$ for fixed forcing amplitude 20 mm and different forcing frequency bandwidths. Dashed lines indicate theoretical predictions with slope −4.

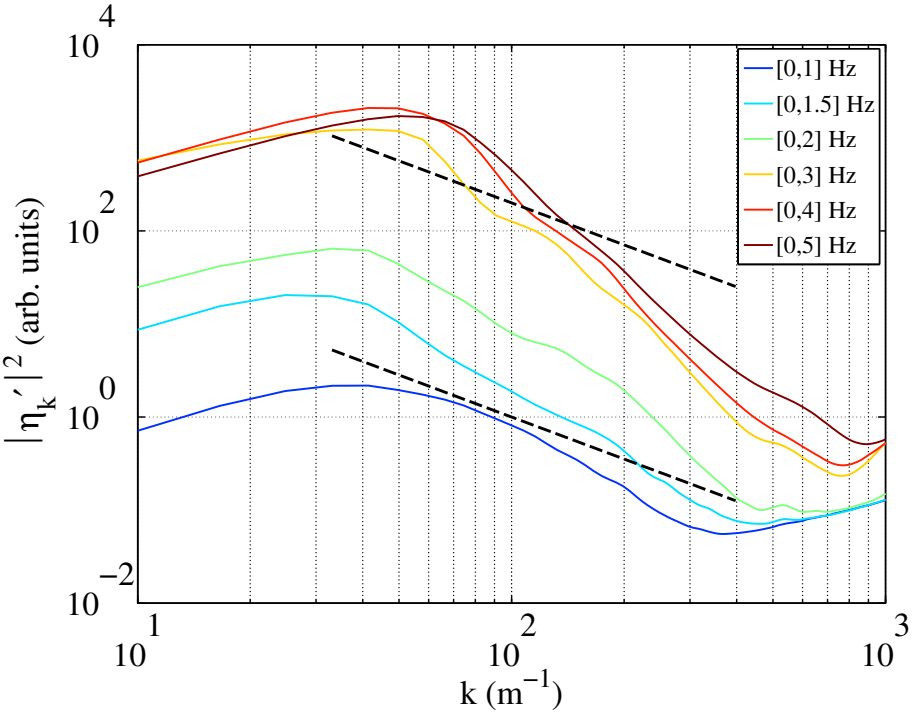

Figure 4.6: Spectra $|\dot{\eta}_k|^2$ for fixed forcing amplitude 20 mm and different forcing frequency bandwidths. Dashed lines indicate theoretical predictions with slope −3/2.

CHAPTER 5

LOCAL MEASUREMENT OF LIQUID DEPTH

This chapter presents an experimental study of underwater depth reconstruction obtained with circle method. The theory of this method is given. The results for three different bottom configurations are presented and discussed. This study has been carried out in the frame of a joint collaboration with Ros Kiri Ing.

We also compare the circle method to the one that deduces the water depth directly using Helmholtz equation and linear dispersion relation.

5.1 Introduction

The underwater depth detection has gained the attention of engineers and sailors over the decades due to their practical applications - the ship transport through the inland waterways and close to the shore or coast (eg. entrance to the harbor). There, water depth is often shallow and contains obstacles, such as rocks. The knowledge of the bottom characteristic and surface navigational informations in these regions is crucial to avoid accidents.

First method, from 1920s onwards, used a lead-line to measure the water depth. It was replaced in the 1950s by a single beam echo sounder, which allowed a continuous recording of depth along track of the ship. Later on, the real-time seabed relief measurement from meter to kilometer was applied. Multibeam systems provided the shape of the seafloor measurements beyond a single-point. This method can be also applied in the domain different than bathymetry. For instance, backscattered signals from different incidence angles can reveal geological history of the seabed and its classification [61].

Modern techniques allow the bottom characterization from the airborne systems (so-called LIDAR methods). Water depth is calculated based on the time difference of light or sound reflected from the water surface and the bottom [36]. The review of the bathymetry methods has been given in 2012 by Blondel [4].

The following sections propose a new technique based on the water waves properties combined with circle method, that has been recently succesfully adapted to study velocity and thickness of the plates [43, 24].

5.2 Circle method principles

First, let us for clarity recall a set of fundamental equations (already presented in Chapter 1 and 2). Let's consider wave propagating on the water surface with wavenumber $k = \|\mathbf{k}\|$ linked to the pulsation ω by the linear dispersion relation:

$$\omega^2 = (gk + \frac{\gamma}{\rho}k^3)\tanh(kH), \tag{5.1}$$

where g denotes the gravity acceleration, ρ water density and H water depth. Note that in general k is a complex number where the real part is related to the wavelength λ and the imaginary part describes the attenuation. In this study we are interested only in the real value. In an area of constant water depth H the surface elevation perturbation is a solution of the Helmholtz equation:

$$(\triangle + k^2)\hat{\eta} = 0, \tag{5.2}$$

In the above equation $\hat{\eta}$ stands for the time Fourier transform of the measured transient height $\eta(x, y, t)$:

$$\hat{\eta}(x, y, \omega) = \int_{-\infty}^{\infty} \eta(x, y, t) \cdot e^{-i\omega t} dt \tag{5.3}$$

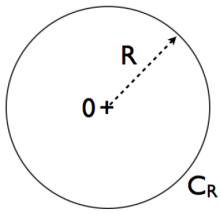

Figure 5.1: Geometry of the circle.

Now, we can define a circle (Fig. 5.1) where these equations are verified and explain the circle method principles. The surface elevation η along the circle can be expressed as:

$$\eta(R, \theta) = \sum_{n=-\infty}^{n=+\infty} a_n J_n(kR) e^{in\theta} \tag{5.4}$$

The average of the surface elevation over the circle is denoted as:

$$\langle \eta \rangle_R = \frac{1}{2\pi} \int_{C_R} \eta(R, \theta) d\theta = a_0 J_0(kR) \tag{5.5}$$

and the value of the surface elevation at the center of the circle $\eta(0) = a_0$. Consequently, the ratio of the average over the circle to the value at the center is:

$$\frac{\langle \eta \rangle_R}{\eta(0)} = J_0(kR) \tag{5.6}$$

This equation forms the basis of the method. In the time domain (when surface waves are generated in the liquid basin), the surface elevation is measured along a circular path and at the center of the circle. The measurement along the circular path is an averaged measurement. Both signals must be simultaneously acquired. After Fourier transform, the signal ratio $\langle \eta \rangle_R / \eta(0)$ is computed and determined as a function of the frequency. The depth of the liquid H is deduced by determining the right dispersion function as defined by eq. (5.1) that allows the Bessel function defined in eq. (5.6) to fit at best experimental data.

To calculate the averaged signal along the circular path, N positions regularly distributed along a circle are chosen and signals at these points are linearly interpolated from previous data and then averaged. In general N is chosen big enough to have an averaged surface elevation signal close to that really measured along a circle. Results shown in this chapter are achieved using $N = 90$.

One can doubt whether the capillary action should be taken into account in the dispersion relation (5.1). Wave should "feel" the bottom, though it is needed to excite rather low frequencies f (long wavelengths λ) for which capillary forces are usually negligible. It is a misleading impression, because one has to take into account a laboratory scale, where depth of few millimeters to few centimeters is usually used. Indeed, for fixed frequency, while a water depth decreases, a wavelength also decreases and the capillary forces become stronger. Red curves in the Fig. 5.2 indicates the full dispersion relation (5.1) for different water depths. Blue lines correspond to the dispersion relation when only gravity action is taken into account. It can be observed that while decreasing water depth, the detachment of the red curves from blue ones is visible for lower and lower values of frequency f, though for very shallow water waves the surface tension action should be included in the model, even for the intermediate frequency values.

It can be also noticed that the curves rejoin at certain frequency and for certain water depth. In that region finite water depth effect becomes negligible (wave does not "feel" the bottom any more), ergo, using this frequency superior water depths cannot be distinguished by looking on the waves. It is a limitation of our method - it demands to operate on such frequencies that change their wavelengths due to the bottom presence.

Fig. 5.3 presents a frequency f in the function of water depth H, for which, due to the bottom presence, the linear dispersion relation is deviated by 10% ($\sqrt{\tanh(kH)} = 0.9$) from its infinite-depth case ($\sqrt{\tanh(kH)} = 1$). It indicates that all frequencies below that curve "feel" the bottom, thus the wavelength is shortened. Fig. 5.3 shows corresponding graph for the wavelength λ versus water depth H. In the latter case the wavelength values above the presented curve are affected by the finite-depth effect and these wavelength are good candidates to determine the water depth. Note that the wavelength of 6 times higher value than the water depth results in only 10% variation of the dispersion relation.

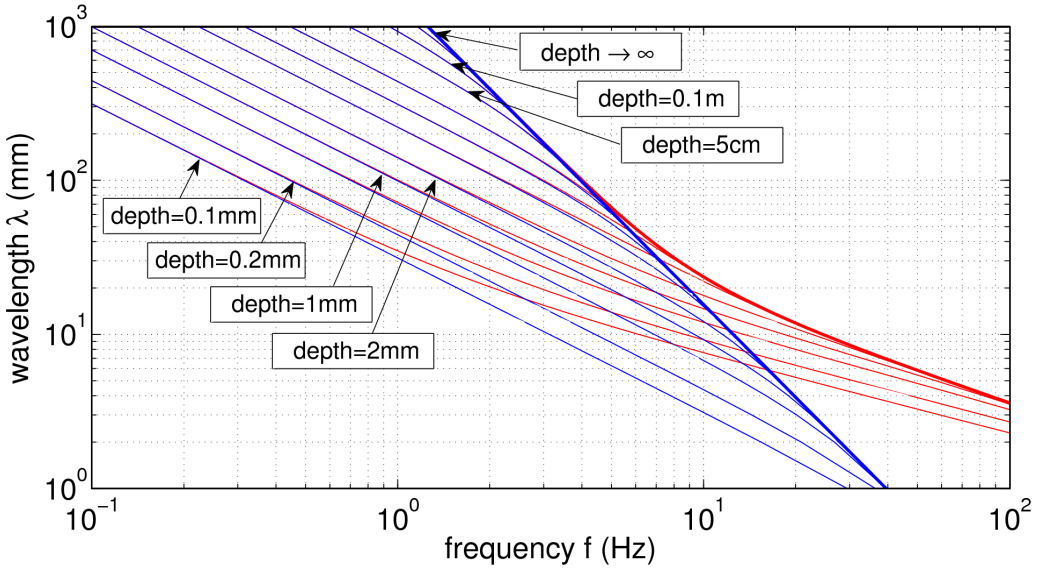

Figure 5.2: Dispersion relation for different water depths. Blue curves: only gravity term is taken into account, red curves: both gravity and capillary terms are included (see eq. (5.1)).

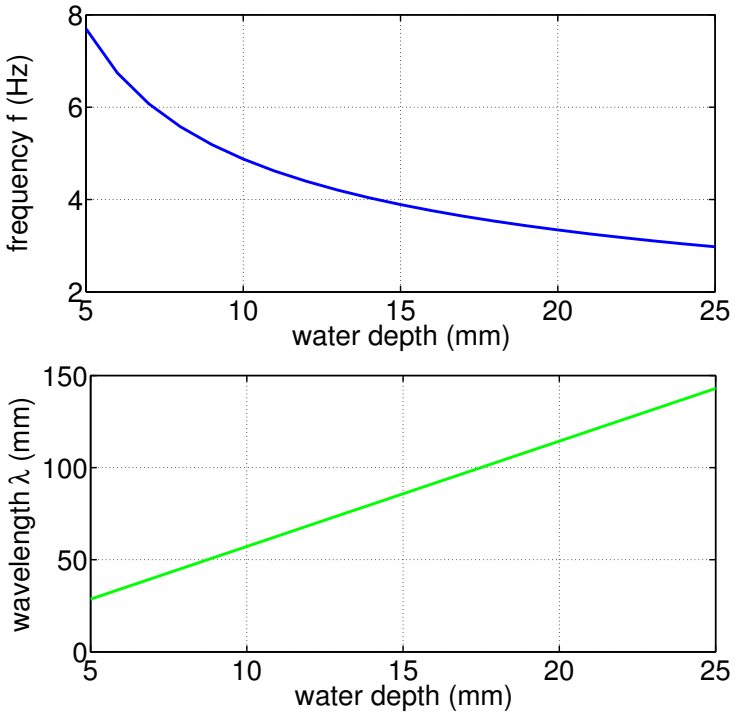

Figure 5.3: Frequency f (top) and wavelength λ (bottom) in the function of water depth H calculated from the dispersion relation (5.1) for $\sqrt{\tanh(kH)} = 0.9$. It corresponds to the 10% deviation from its infinite-depth case ($\sqrt{\tanh(kH)} = 1$).

5.3 Experimental setup

The experiments have been carried out in the tank with dimensions 53x38 cm^2 filled with water with non-negligible attenuation and varying depth $H(x,y)$. The surface elevation $\eta(x,y,t)$ was measured with a good accuracy in time and in space during the wave propagation using a Photron SA4 high-speed camera with the acquisition frequency of 125 fps.

The experiment consists in recording the transient waves produced by a broadband wavepacket signal, generated by the conical vibrator, that can be considered as a source point. A one-period sinusoidal pulse centered at $f_0 = 4$ Hz was imposed, exciting a wave packet propagating with the linear dispersion relation (5.1). The perturbation $\eta(x,y,t)$ is measured during 50 s till the total attenuation of the wave.

Three different geometrical configurations have been studied:

- **C1**: basin with constant liquid depth $H_0 = 12$ mm.
- **C2**: a conical, step pyramid is placed in the middle of the bottom of the configuration C1. The geometry of the pyramid is show in the Fig. 5.4. The total pyramid height is 10 mm, thus is 2 mm below the liquid free surface.
- **C3**: different objects of different heights are immersed inside the basin of $H_0 = 47$ mm liquid depth (Fig. 5.9(a)).

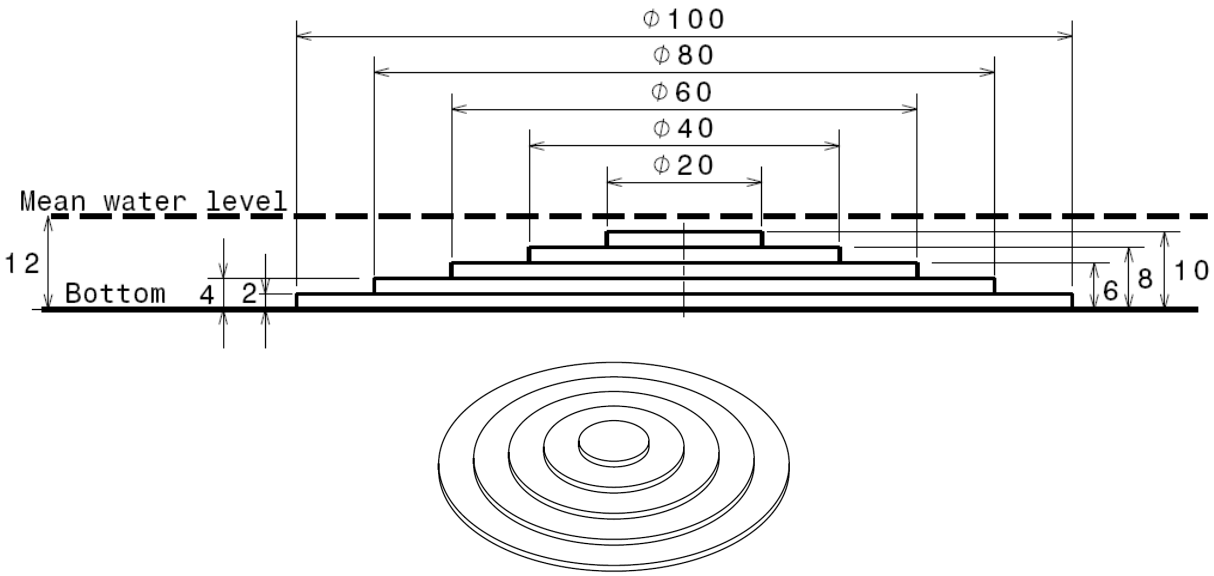

Figure 5.4: Geometrical configuration C2: side view with dimensions and a 3D view.

5.4 Results - circle method depth reconstruction

As afore-mentioned in the circle method description - to obtain water depth one has to fit the right Bessel function $J_0(kR)$ (which depends on the dispersion relation though also on the water depth) to the signal ratio $\langle\eta\rangle_R/\eta(0)$ obtained from the experimental measurements.

In the Fig. 5.5 the typically obtained ratio $\langle\eta\rangle_R/\eta(0)$ in the function of frequency for water depth $H = 2$ mm and $R = 5$ mm is shown by the blue points. It is fitted with $J_0(kR)$ function considering only gravity forces (black continuous curve) and considering both - gravity and capillary forces (black dotted curve). As expected, the capillary wave action has to be considered. This fit gives the expected water depth. The red curves are given for the comparison and present $J_0(kR)$ functions, while considering water depth $H = 20$ mm. They are found to be far from the experimental points. This fitting procedure is repeated in the recorded image zone giving a water depth map.

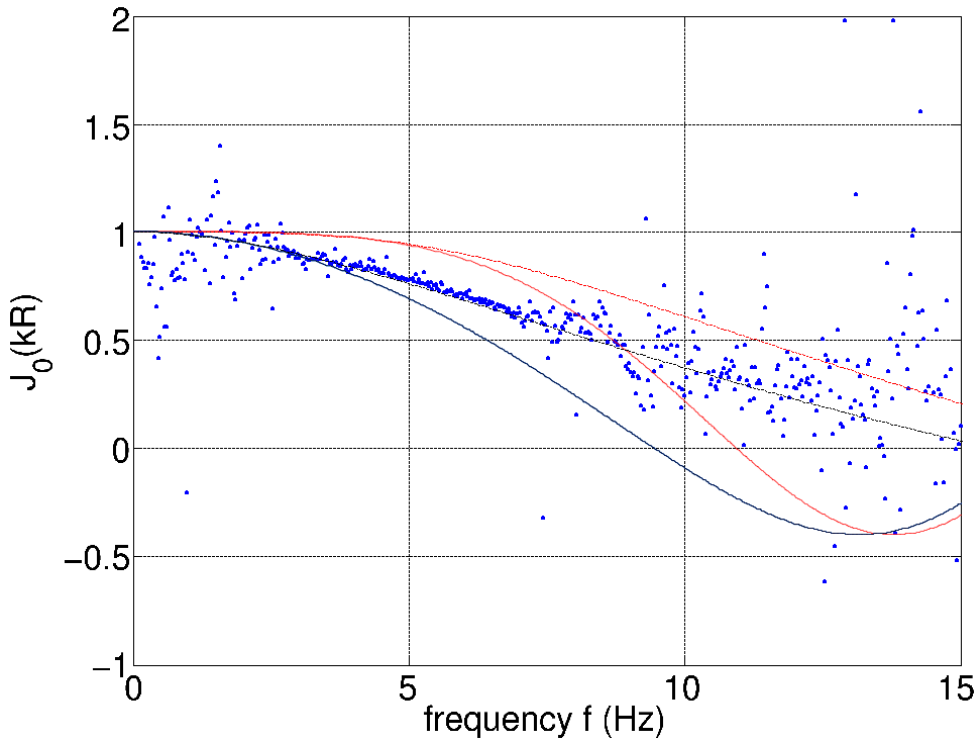

Figure 5.5: Experiment with water depth $H = 2$ mm: blue points show obtained ratio $\langle\eta\rangle_R/\eta(0)$ for $R = 5$ mm (see eq. (5.5) and (5.6)). Continuous and dotted lines present Bessel functions $J_0(kR)$ considering only gravity and both - gravity with capillary effects, respectively. Red lines are plotted assuming water depth on the level of 20 mm, while the black ones on the level of 2 mm.

Configuration C1

The first geometrical configuration C1 with constant depth was used to characterize accuracy level and resolution of the circle method for water waves. The wavelength λ_0 corresponding to f_0 for $H_0 = 12$ mm is equal to 8 cm and water can be treated as shallow. Fig. 5.6 shows the real part of the signal ratio as a function of the product kR for different values of R. It can be observed that kR variations fit well Bessel function even for low values of R. For these values however, the fitting process is not expected to be accurate, because the Bessel curve is not well enough defined. Therefore a biased value of the liquid depth H parameter is expected. The used frequency bandwidth is 0.1 Hz-5.5 Hz.

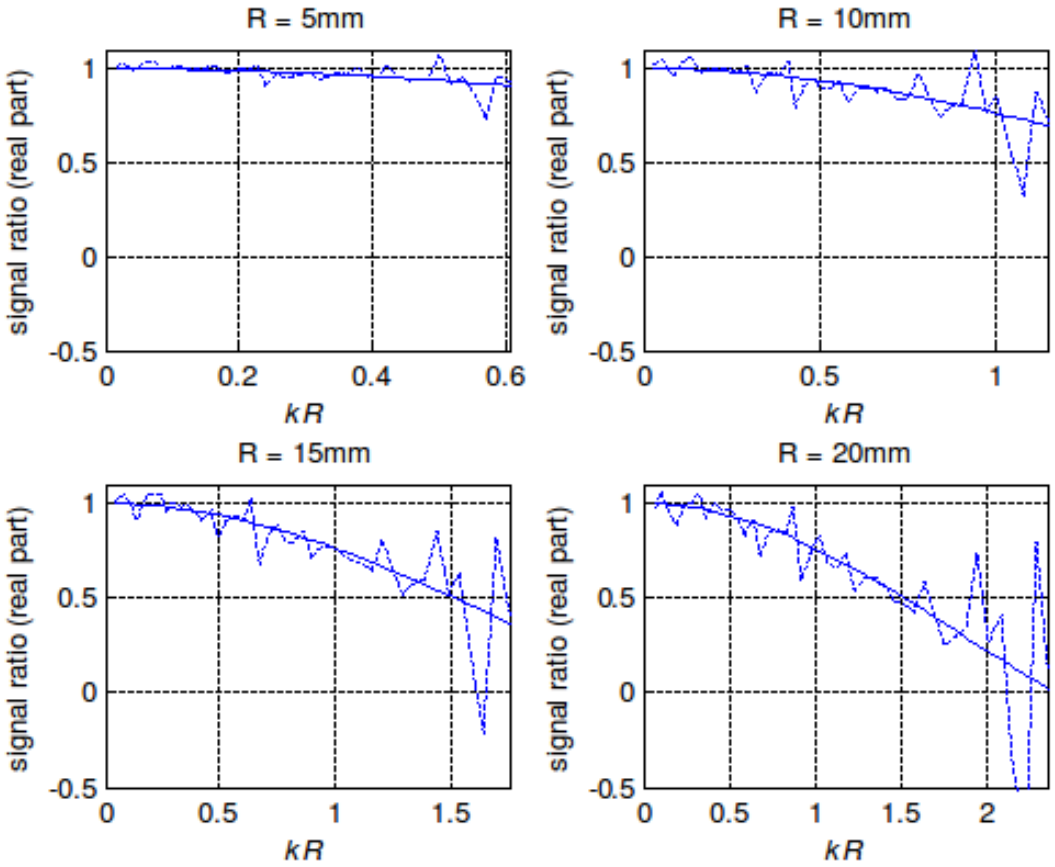

Figure 5.6: Configuration C1 with constant water depth $H = 12$ mm. Signal ratio $\langle \eta \rangle_R / \eta(0)$ versus kR for different values of R. Dotted lines: experimental data. Solid lines: Bessel $J_0(kR)$ fitting function.

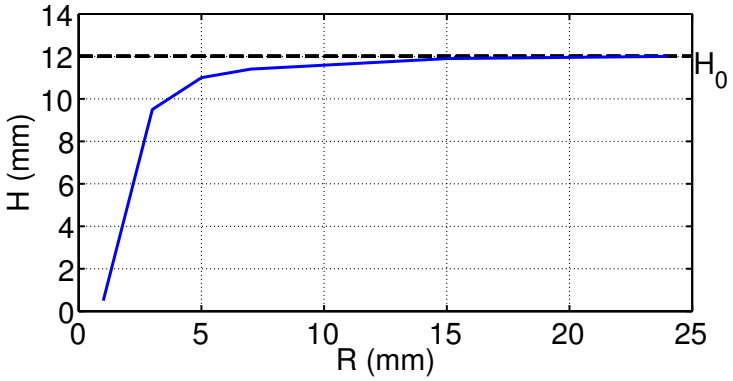

Figure 5.7: Liquid depth H versus circle radius R for configuration C1.

Fig. 5.7 shows variation of the liquid depth parameter H (after fitting process) versus radius circle R. The fitting process is based on the minimization of the quadratic error. It is observed that H parameter evolves toward an asymptotic value. The final value to within 5% is reached when the radius R is greater than 10 mm. At 5.5 Hz, the surface elevation wavelength λ_{min} is equal to 52 mm. The final value to within 5% is achieved when the circle radius is approximately higher than $\lambda_{min}/4$.

Configuration C2

Since the depth of the liquid without obstacles H_0 is known for each configuration we can introduce a value $s(x,y)$, which stands for a local shape of the bottom (bathymetric map) and can be calculated as the difference between known constant liquid depth without obstacles H_0 and locally obtained liquid depth H:

$$s(x,y) = H_0 - H(x,y) \tag{5.7}$$

The representation by the variable $s(x,y)$ is more natural, because we can directly compare the theoretical geometry of the bottom with experimentally obtained shape $s(x,y)$.

In the case of configuration C2, Fig. 5.8 represents $s(x,y)$ computed with two different radii R = 10 mm and R = 20 mm. As expected, for low values of R,the liquid depth values are biased. In this case, resolution is however better. For larger values of R, $s(x,y)$ are less chaotic, but the conical pyramid is also less defined. In the neighborhood of the obstacle, constant bottom was found to be deeper than it was in real and becomes more accurate while moving away from the obstacle.

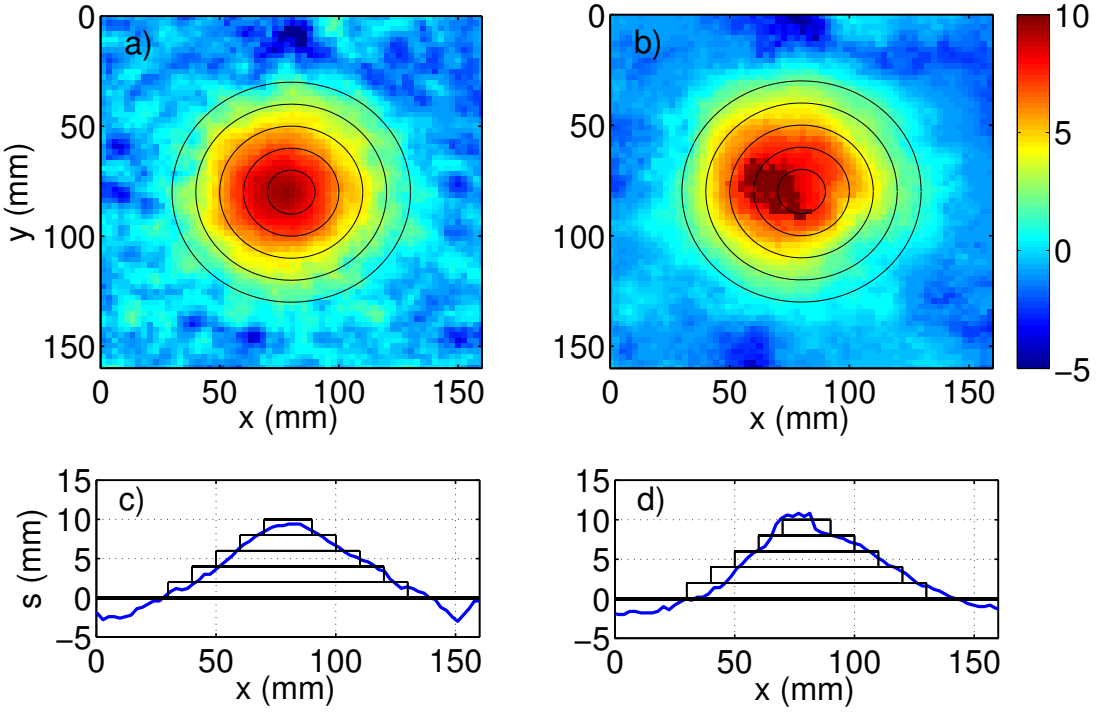

Figure 5.8: Bathymetric maps $s(x,y)$ obtained experimentally by means of the circle method for two different values of R = 10 mm (a) and R = 20 mm (b). The color scale of the local bottom shape $s(x,y)$ is given in millimeters. Plots (c) and (d) correspond to the horizontal cut at y = 80 mm (center of the obstacle).

Configuration C3

In configuration C3 several objects are immersed inside the basin. The geometrical configuration is shown in the Fig. 5.9(a). Each value shown on the top of each object corresponds to its height. The liquid level in the basin is $H_0 = 47$ mm.

Experimentally determined bottom shape distribution $s(x, y)$ is presented in the Fig. 5.9(b). All the obstacles (except the one with lowest height) are reconstructed by the method. The obstacles are found to be broader then in reality (the influence of the radius R). The bottom of the tank is in agreement with the theory. The obstacle with lowest height (3 mm) cannot be found due to the small deviation in the Bessel function between the depth of the liquid over the bottom of the tank and over the obstacle. Cylinders with height 25 mm and 30 mm can be observed, but the reconstructed height is around 20% lower then the real one. The black cylindrical obstacle (even being enough high to be correctly detected) has small diameter and due to the circle radius R its height has been found to be lower than the expected one. Positions and heights of the other obstacles are correctly reconstructed.

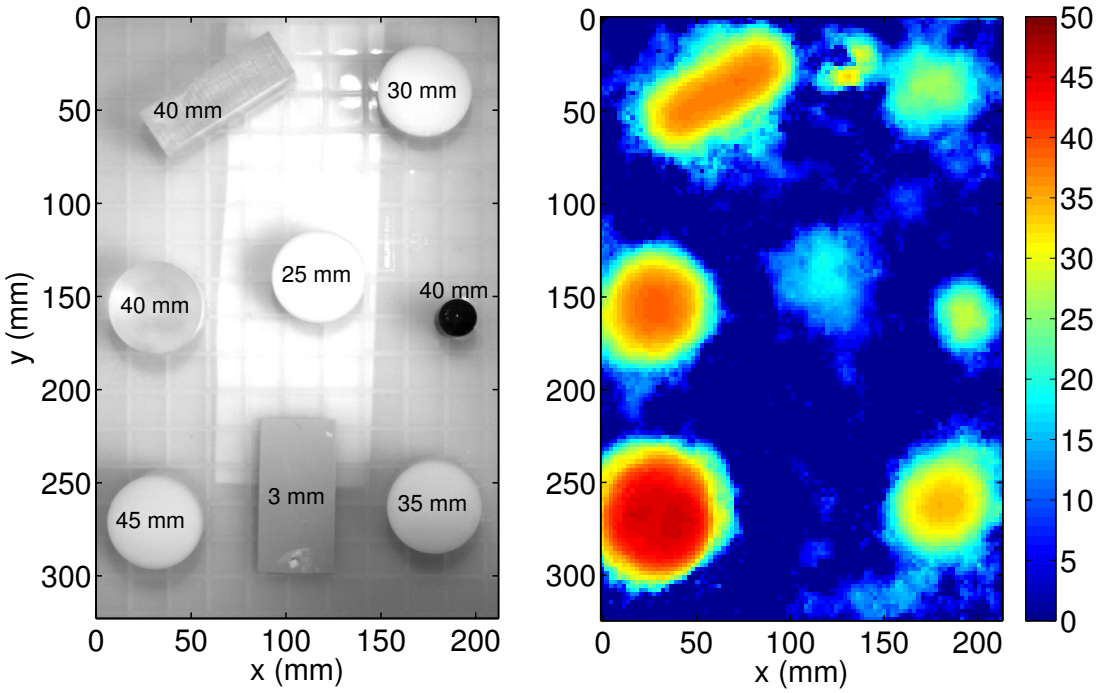

Figure 5.9: Configuration C3: real geometry of the bottom (left) and corresponding bathymetric maps $s(x, y)$ (right) obtained experimentally by means of the circular method ($R = 20$ mm) for liquid depth $H_0 = 47$ mm. The color scale of the local bottom shape $s(x, y)$ is given in millimeters

5.5 Results - depth reconstruction by use of Helmholtz equation

Configuration C2 has been also tested by another method, that used directly Helmholtz eq. (5.2) to reconstruct the bottom shape.

Since we operate in the shallow water and waves are governed by the linear dispersion relation (5.1) and Helmholtz eq. (5.2) we can make use of the method developed in the Chapter 2 and find the local value of k. For fixed frequency, the information about the local k gives us the information about the local water depth H, *ergo*, the form of the bottom $s(x,y)$. In the extreme case, the local region can be defined as a pixel size. In that case (instead of minimizing the norm on the complex plain as it was in Chapter 2), it can be written that:

$$k(x,y,\omega) = \sqrt{\frac{-\triangle\hat{\eta}(x,y,\omega)}{\hat{\eta}(x,y,\omega)}} \tag{5.8}$$

Obviously, in the presence of obstacles - that value will not be constant! The examples of the measured $\hat{\eta}$ fields and corresponding laplacians $(-\Delta\hat{\eta})$ for frequency 4 Hz and 6 Hz are shown in the Fig. 5.10 and Fig. 5.11, respectively. Two observations are evident on that figures. Firstly, as expected, in contrary to the results obtained in the Chapter 2, the patterns of $\hat{\eta}$ and $(-\Delta\hat{\eta})$ are not identical. Secondly, in the case of 6 Hz they resemble much more than for 4 Hz. For 4 Hz one can observe a notable difference of the color contrast between the center of the obstacle (center of the image) and its surrounding. Indeed, lower frequency has longer wavelength, thus the 4 Hz wave "feels" bottom more than the wave of 6 Hz and thus k is stronger scaled.

This procedure gives a result of water depth (obtained from every frequency!) by simple use of the linear dispersion relation (5.1) in the form:

$$H(x,y,\omega) = \operatorname{atanh}\left(\frac{\omega^2}{gk+\frac{\gamma}{\rho}}\right)/k \tag{5.9}$$

The FTP measurements of the transient η allowed to obtain the $\hat{\eta}$ fields for a broad range of frequencies with 0.2 Hz step. Then, we can average the obtained H fields over the possible pulsations. The averaging process here is very important - note the denominator in the eq. (5.9) can take the values close 0 and thus this division is very sensible to noise. The results of $s(x,y)$ are given in the Fig. 5.12 for averaged frequencies in the range from 3 to 5 Hz and from 5 to 7 Hz. The minimum depth is reconstructed properly. The step-like shape of the pyramid has not been found, like as it was for the circle method. The bottom of the tank in both cases is found to be shifted upwards compared to the real one. It is due to the penetration depth of the wave. The Fig. 5.10 suggested that 4 Hz is a better candidate to measure water depth. Indeed, the result obtained for the frequency range from 3 to 5 Hz reconstructed more precise shape of the bottom.

Unfortunately, this method did not allow to obtain results for lower values of frequency than 3 Hz. Noise becomes too strong. Note that noise is not dependent from k, thus when k decreases, computation of k from eq. (5.9) drastically reduces.

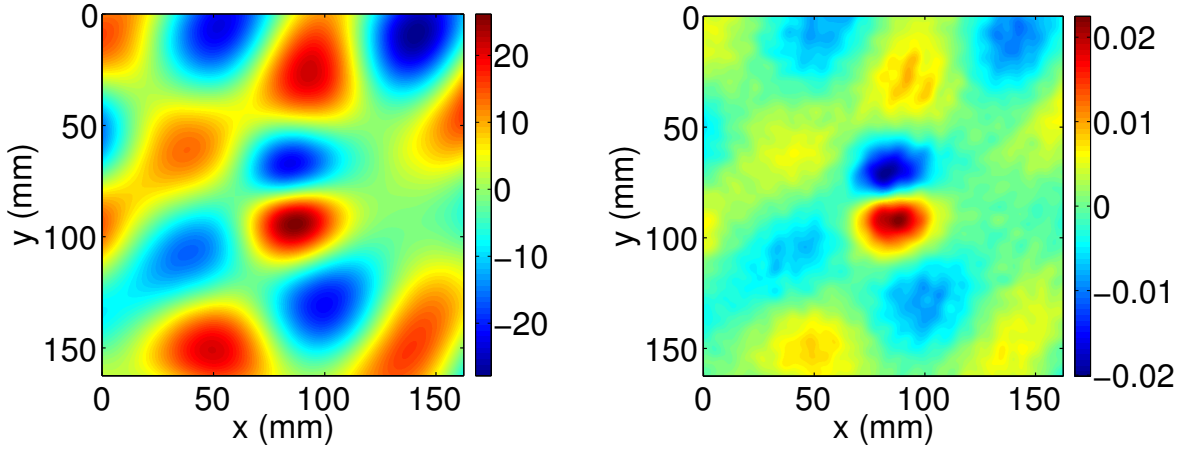

Figure 5.10: Typical real value of the complex signal $\hat{\eta}$ (left) and corresponding real value of its laplacian with a negative sign: $-\Delta\hat{\eta}$ (right) for 4 Hz.

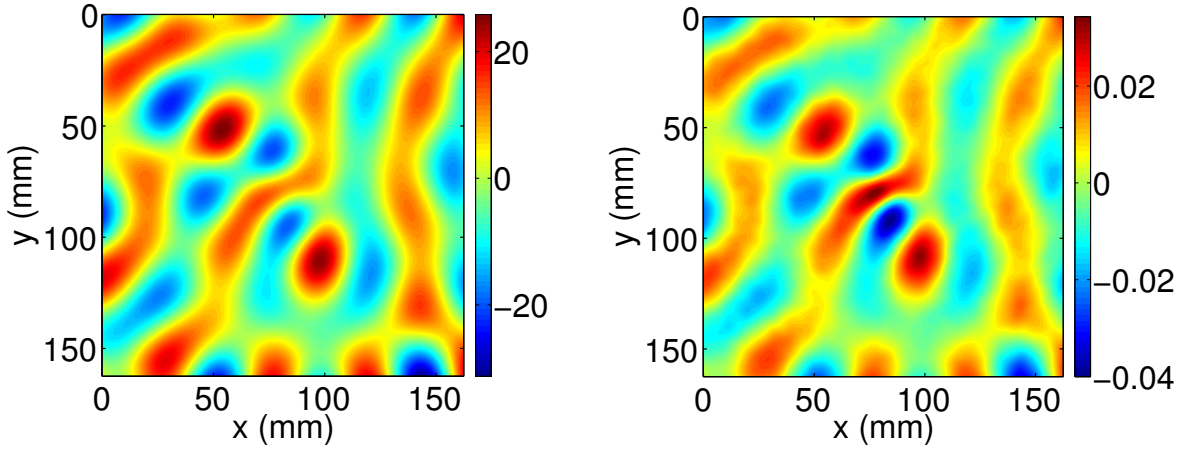

Figure 5.11: Typical real value of the complex signal $\hat{\eta}$ (left) and corresponding real value of its laplacian with a negative sign: $-\Delta\hat{\eta}$ (right) for 6 Hz.

5.6 Conclusions

The presented experimental results showed a feasibility of the local detection of liquid depth by circle method for surface waves. The assumptions are that the wave obeys the wave equation in linear regime and the measurement area is far from the boundaries where evanescent waves or nonlinear effects should exist. It has been shown that the liquid depth can be determined locally and quantitatively under the circle area with the limitation that no sharp edges can be reconstructed and the smooth transition of the liquid depth is obtained in all cases. The method is found to be robust and not very sensitive to noise, since it integrates the wave dynamics on a broad range of frequencies. Besides, the integral on the circle is another step that reduces the noise effect. Wave excitation due to windy environment is sufficient for the presented method and the measurements could be done without any vibrator.

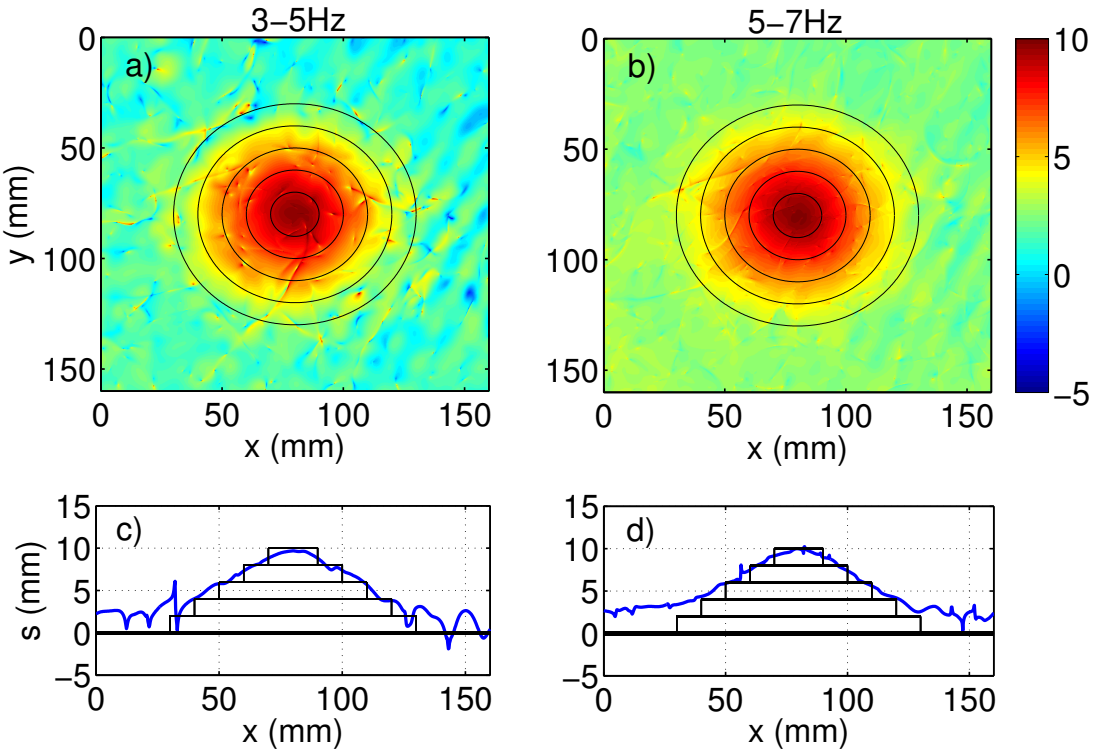

Figure 5.12: Experimental bathymetric maps $s(x,y)$ obtained from eq. 5.9 for two different frequency ranges: $3-5$ Hz (a) and $5-7$ Hz (b). The color scale of the local bottom shape $s(x,y)$ is given in millimeters. Plots (c) and (d) correspond to the horizontal cut at $y = 80$ mm (center of the obstacle). Singular lines can be observed in the areas where $\hat{\eta}(x,y,\omega)$ is close to 0 (see eq. 5.8)

Along with the circle method, the local bottom detection by Helmholtz equation has been performed. This method was found to be robust but only for very shallow water due to high noise for low wavenumber values.

CHAPTER 6

CONCLUSIONS AND PERSPECTIVES

6.1 Summary and conclusions

This thesis presents advances in the understanding of current water waves challenges. The experimental investigations concentrated on time-reversal and wave turbulence phenomenon as well as resonance-type damping of surface waves and underwater depth reconstruction.

The first prominent study concerned the development of the measuring system. It raised from the need of free-surface deformation measurement. Previously, techniques were usually limited to one-point measurements or synchronized array-points measurements, which could not cover an extensive area of surface with good lateral resolution. Fourier Transform Profilometry (FTP) method, recently adapted for surface waves, has been used for high-resolution global measurements of surface deformation. This optical method uses fringe projection and thus requires a diffusive reflection of light on the liquid surface. It was previously obtained by diluting white paint in water. This procedure was found to unintentionally change the properties of the surface resulting in the dramatically increased wave damping compared to pure water.

It is found that the presence of film at the surface of water is responsible for that spurious attenuation. Standard paints contain surfactants which create monolayer on the surface, which results in the appearance of Marangoni waves accompanying surface waves. These waves are strongly attenuative and the film can induce the resonance-type wave damping between Marangoni and capillary-gravity waves.

The presented study confirms, experimentally, the Marangoni-surface wave resonance damping. The theoretical prediction of the relative damping of water covered by a thin viscoelastic surface is successfully fitted to the experimental results obtained for water colored by plain paint. The maximum damping enhancement was found to be 25 times larger than the attenuation of pure water and occurred around 4 Hz, which was shown to coincide with

the intersection of the dispersion relation branches for the surface and Marangoni waves.

The elimination of that attenuation demanded an extensive physico-chemical study of different coloring pigments, including the measurements of zeta-potential, particles size and surface tension. Finally, the anatase (TiO_2) pigment was found to make the water surface light diffusive while avoiding any surface film effects, which has been confirmed by the measurement of wave attenuation.

This investigation was crucial for further experimental studies and allowed the performing of space-time resolved FTP measurements of water waves with a damping equivalent to the clean surface case.

Next, an attention turned to the phenomenon of time-reversal, commonly studied in the other fields of wave science. Refocusing back the energy could be accomplished because of the time-reversal invariance of the wave equation. The linear wave packet was mechanically generated by the conical wavemaker. To take advantage of the multiple reflections, the water tank cavity of the size not larger than a dozen wavelengths of the central frequency was used. Surface elevation was measured during direct propagation by the FTP method. In a second step, the signal recorded was time reversed and re-emitted separately at 6 different positions, making use of the system linearity. The attenuation was that the wave could propagate roughly 10 to 20 times the lengthscale of the cavity.

The results show that the effect of viscous attenuation damps the excited high frequencies. Though, due to the dispersion of water waves, one-channel experiment was sufficient to focus wave spatially and temporally (for every of the re-emitting channel), however, in this case converging wavefronts are not clearly visible (not enough information from every angle). In a time-reversal experiments with multiple channels, the quality of refocusing has been found to be linearly dependent on the number of the re-emitters. It is in the agreement with the theory. Quality of refocusing should increase linearly with the number of excited modes. Considering that the re-emitting channels are random and uncorrelated, they should in general excite a similar number of modes. In the case of 6 re-emitting channels, the converging and diverging wavefronts can be easily observed.

The effect of damping was found to limit the quality of refocusing, but could not suppress it, however, a relatively short time-reversal window has been used. The increase of that window did not result in a focusing quality increase. Numerical simulations corresponding to water waves at larger scales with negligible damping indicate the possibility of very high quality refocusing.

As a closing remark, it should be noted that the results obtained in the frame of this study represent a significant advance in time-reversal phenomenon. To our knowledge, it is a first quantitative experimental evidence for time-reversal focusing of surface waves.

Further experiments concentrated on wave turbulence (WT). It is an out-of-equilibrium state of nonlinear wave-wave interactions. The analytical solution of the kinetic equation predicts that the energy is transfered through different wavelengths from the injection scale

to the scale where it is dissipated. This solution is similar to the power law scaling of the energy density spectrum predicted by Kolmogorov for fully developed turbulence. The WT is present in different wave fields such as vibrations on elastic sheets, Alfvén waves in solar winds or waves in nonlinear optics.

Only few experimental results have been performed in the field of surface WT. Moreover, most of these measurements are restricted only to one point measurement and cannot be directly compared to the theory which predicts the statistics in the space-time dimensions. Prior to the presented investigations, only one experimental study for surface WT with the access to the Fourier space has been published.

Our experiments were performed in the laboratory water tank and surface waves were generated by two piston-type wavemakers. Two different forcing frequency bandwidths for various forcing amplitudes were analyzed. The aim of the use of narrow bandwidth was to maximally increase inertial range and of broad bandwidth to increase the wave intensity.

The departure point for further analysis was the study of wavevector-frequency energy spectra for surface elevation, which constitute the major result of that investigations. The narrowband forcing confirmed the persistence of the energy density close to the linear dispersion relation, whatever the forcing amplitude. It gives the evidence that for this forcing bandwidth our system was indeed weakly nonlinear. For this bandwidth, the power density function for surface velocity takes a Gaussian form. Frequency spectra slope and space spectra slope for gravity regime approach the WT predictions. The power law scaling in the function of the injected power is also in the agreement with the theory.

For broadband forcing, the appearance of bound modes produces deviations with respect to the theory. Increasing wave intensity, increases the energy carried by the bound modes. In that case, frequency spectra were found to be forcing dependent. Surprisingly, decreasing the wave intensity did not result in the elimination of the bound waves and did not permit to approach the WT predictions for gravity regime. Despite that fact, the capillary regime showed a good accord with the theory.

This experimental study revealed, for the first time, the 3D spectra for surface elevation with the agreement with the theory. Overcoming the previous inconsistencies between experimental results and theoretical predictions, the turbulent energy cascade obtained for narrow forcing bandwidth confirmed the weakly nonlinear behavior of waves assumed by the theory. The disagreement with theory for broad forcing bandwidth has been shown to be similar to the one observed in the previous experimental studies. The difference between these two regimes remains an open question.

The final experiments carried out during my thesis concentrated on the underwater depth reconstruction. The practical interest come from the coastal engineering and inland transport. In the case of shallow water surface wave, deformation can reflect the information about water depth. This property has been used in this study to deduce the form of the bottom.

The surface elevation is measured and averaged along a circular path and at the center of the circle. After a time Fourier transform, the ratio of that quantities is fitted with the appropriate Bessel function. The one that fits the best experimental data while adjusting the water

depth was selected. This procedure is done for broad range of frequencies, which reduces the noise.

It is shown that for different water depths, different working frequencies should be used. After inspecting three geometrical configurations it has been proved that the liquid depth can be determined locally and quantitatively. The limitations here are the sharp edges that could not be determined in any of the analyzed configurations and the obtained bottom shape was smooth. In addition, the immersed object were found to be larger than in the reality. It is also the effect of the edges and of drastic change of the water depth, which cannot be perfectly reflected in the water surface (waves do not support discontinuities).

6.2 Perspectives

The improvement to the already existing optical profilometric method for free-surface measurements opened the possibilities of more precise and detailed analysis of the phenomena that were not accessible before. This development has been used to study some of the currently important wave problems. Here, I would like to propose further experiments that arise from the performed studies and advances applied to the measuring technique.

The study of the freak waves constitutes an experimental challenge and is of great interest to the physical communities. In a manner similar to the wave turbulence, energy can be imposed to the system with a high amplitude, giving rise to the strong nonlinearities. The random interactions could finally result in the rogue wave creation. This wave could be captured by the optical method and later studied in terms of time and spatial evolution. This would give a quantitative evidence of a freak wave that is not synthetically created, but is a spontaneous event.

Moreover, once the rogue wave appears and is measured, it could be extremely interesting to try to recreate its form using the time-reversal phenomenon. This would give a possibility to test this phenomenon in terms of nonlinearities and, eventually, to systematically study the interactions leading to the freak wave appearance. In addition, different time-reversal points and time-reversal windows could be used.

Encouraged by the promising results obtained for water wave turbulence, further effort should be directed towards the characterization of the difference between narrowband forcing and broadband forcing. It can cast a light on the features responsible for that difference and can give the reason of the observed discrepancies between the theory and experiments.

The next problem proposes for future experimental investigations is the detailed study of

underwater depth reconstruction. The limits for water depth, object size, lateral and depth resolution in the function of analyzed frequencies should be further studied. The comparison of cost and time consumption with recently existing bathymetry methods should be performed to validate the applicability of this technique in the fields of engineering.

Finally, I would like to discuss another significant wave phenomenon, which results from the recent scientific and technological progress, that demands a precise experimental research. Wave focusing by use of unconventional materials with negative refractive index (metamaterials) received a worldwide attention from the wave science communities after Pendry's breakthrough paper published in 2000 [65]. He showed that waves converging through the flat metamaterial lens can beat the diffraction limit. Furtheremore, in 2006, metamaterials were found to have another impressive application - concealing the objects from electromagnetic waves [66], thus creating an "invisibility cloak". Since then, research in many fields such as acoustics or thermodynamics has been focused on creating metamaterials for different kinds of waves

In the case of water waves, the metamaterial effect can be obtained when water wave propagates over a periodic structure with a subwavelength size. The behavior of surface waves in the presence of metamaterials have been recently studied [7, 29, 30, 41] for different aspects (antenna, cloaking, lensing), but there is still much to be done theoretically, numerically and experimentally. An accurate technique for experimental analysis will move forward this field of wave science. The notable motivation here for further research is the cloaking of floating structures that can be used for coastline protection. Our group recently designed and tested a surface water wave deviators obtaining very optimistic results [64].

BIBLIOGRAPHY

[1] W. Alpers and H. Huehnerfuss. The damping of ocean waves by surface films: A new look at an old problem. *J. Geophysical Research*, 94(5):6251–6265, 1989.

[2] F. Behrozzi. Fluid viscosity and the attenuation of surface waves: a derivation based on conservation of energy. *Eur. J. Phys*, 25:115–122, 2004.

[3] P. Behrozzi, K. Cordray, W. Griffin, and F. Behrozzi. The calming effect of oil on water. *Am. J. Phys.*, 75(5):407–414, 2007.

[4] P. Blondel. Bathymetry and Its Applications. INTECHWEB.ORG, online edition, 2012.

[5] M. G. Brow and A. Jensen. Experiments on focusing unidirectional water waves. *J. Geophys. Res.*, 106(16):917–928, 2001.

[6] D. Cassereau and M. Fink. Time Reversal of Ultrasonic Fields-Part III: Theory of the Closed Time-reversal Cavity. *IEEE Trans. Ulatrason. Ferroelectr. Freq. Control*, 39:579–592, 1992.

[7] H. Chen, J. Yang, J. Zi, and C.T. Chan. Transformation media for linear liquid surface waves. *Europhys. Lett.*, 85:24004, 2009.

[8] R. Cini and P.P. Lombardini. Experimental evidence of maximum in the frequency domain of the ratio of ripple attenuation in monolayered water to that in pure water. *J. Colloid Interface Sci.*, 81 (1):125–131, 1981.

[9] R. Cini, P.P. Lombardini, C. Manfredi, and E. Cini. Ripples damping due to monomolecular films. *J. Colloid Interface Sci.*, 119:74–80, 1987.

[10] P. Cobelli, A. Maurel, V. Pagneux, and P. Petitjeans. Global measurement of water waves by Fourier transform profilometry. *Exp. Fluids*, 46:1037–1047, 2009.

[11] P. Cobelli, V. Pagneux, A. Maurel, and P. Petitjeans. Experimental observation of trapped modes in a water wave channel. *Euro Phys. Letters*, 88:20006, 2009.

[12] P. Cobelli, P. Petitjeans, A. Maurel, V. Pagneux, and N. Mordant. Space-Time Resolved Wave Turbulence in a Vibrating Plate. *Phys. Rev. Lett.*, 103:204301, 2009.

[13] P. Cobelli, V. Pagneux, A. Maurel, and P. Petitjeans. Experimental study on water-wave trapped modes. *J. Fluid Mech.*, 666:445–476, 2011.

[14] P. Cobelli, A. Przadka, P. Petitjeans, G. Lagubeau, V. Pagneux, and A. Maurel. Different Regimes for Water Wave Turbulence. *Phys. Rev. Lett.*, 107:214503, 2011.

[15] C.S. Cox. Measurement of slopes of high-frequency wind waves . *J. Mar. Res.*, 16(9):199–225, 1958.

[16] J.T. Davies and R.W Vose. On the damping of capillary waves by surface films. *Proc. Roy. Soc., Ser A*, 286:218–234, 1965.

[17] P. Denissenko, S. Lukaschuk, and S. Nazarenko. Gravity Wave Turbulence in a Laboratory Flame. *Phys. Rev. Lett.*, 99:014501, 2007.

[18] A. Derode, P. Roux, and M. Fink. Robust Acoustic Time Reversal with High-Order Multiple Scattering. *Phys. Rev. Lett.*, 75(23):4206–4210, 1995.

[19] R. Dorrenstein. General linearized theory of the effect of surface films on water ripples. *Proc. K. Ned. Akad. Wet. Ser. B*, 54:260–272, 350–356, 1951.

[20] C. Draeger and M. Fink. One-Channel Time Reversal of Elastic Waves in a Chaotic 2D-Silicon Cavity. *Phys. Rev. Lett.*, 79(3):407, 1997.

[21] C. Draeger and M. Fink. One-Channel Time-reversal in chaotic cavities: Theoretical Limits. *J. Acoust. Soc. Am*, 105(2):611–617, 1999.

[22] C. Draeger, J-C. Aime, and M. Fink. One-Channel Time-reversal in chaotic cavities: Experimental Results. *J. Acoust. Soc. Am*, 105(2):618–625, 1999.

[23] S. Dyachenko, A. C. Newell, A. Pushkarev, and V. E.Zakharov. Optical turbulence: weak turbulence, condensates and collapsing filaments in the nonlinear Schrödinger equation. *Physica D*, 57:96–160, 1992.

[24] N. Etaix, A. Leblanc, M. Fink, and R. K. Ing. Thickness or phase velocity measurements using the Green's function comparison method. *IEEE Trans. Ulatrason. Ferroelectr. Freq. Control*, 57(8): 1804–1812, 2000.

[25] C. Falcon, E. Falcon, U. Bortolozzo, and S. Fauve. Capillary wave turbulence on a spherical fluid surface in zero gravity. *Europhys. Lett.*, 86:14002, 2009.

[26] E. Falcon. Laboratory experiments on wave turbulence. *Discrete Contin. Dyn. Syst. B*, 13:819–840, 2010.

[27] E. Falcon, S. Fauve, and C. Laroche. Observation of intermittency in wave turbulence. *Phys. Rev. Lett.*, 98:154501, 2007.

[28] E. Falcon, C. Laroche, and S. Fauve. Observation of gravity-capillary wave turbulence. *Phys. Rev. Lett.*, 98:154503, 2007.

[29] M. Farhat, S. Enoch, S. Guenneau, and A. B. Movchan. Broadband cylindrical acoustic cloak for linear surface waves in a fluid. *Phys. Rev. Lett.*, 101:134501, 2008.

[30] M. Farhat, S. Guenneau, S. Enoch, G. Tayeb, A. B. Movchan, and N. V. Movchan. Analytical and numerical analysis of lensing effect for linear surface water waves through a square array of nearly touching rigid square cylinders. *Phys. Rev. E*, 77:046308, 2008.

[31] M. Fink. Time Reversal of Ultrasonic Fields-Part I: Basic Principles. *IEEE Trans. Ulatrason. Ferroelectr. Freq. Control*, 39:555–566, 1992.

[32] M. Fink. Time-Reversal Acoustics. *J. Phys.: Conf. Ser.*, 118:012001, 2008.

[33] M. Fink, D. Cassereau, A. Derode, C. Prada, P. Roux, M. Tanter, J.-L. Thomas, and F. Wu. Time-reversed acoustics. *Rep. Prog. Phys.*, 63:1933, 2000.

[34] S. Galtier, S. V. Nazarenko, A. C. Newell, and A. Pouquet. A weak turbulence theory for incompressible magnetohydrodynamics. *J. Plasma Phys.*, 63:447–488, 200.

[35] S. S. Gorthi and P. Rastogi. Fringe Projection Techniques: Whither we are? *Optics and Lasers in Engineering*, 48(2):133–140, 2010.

[36] G. C. Guenther, A. G. Cunningham, P. E. LaRocque, and D. J. Reid. Meeting the accuracy challenge in airborne LIDAR bathymetry. *Proceedings of EARSeL-SIG-Workshop LIDAR*, Dresden/FRG, 2000.

[37] E. Guerber, M. Benoit, S.T. Grilli, and C. Buvat. A fully nonlinear implicit model for wave interactions with submerged structures in forced or free motion. *Eng. Analysis with Boundary Elements*, 36:1151–1163, 2012.

[38] K. Hasselmann. On the nonlinear energy transfer in a gravity-wave spectrum. Part 1. General Theory. *J. Fluid Mech.*, 12:481–500, 1962.

[39] D.M. Henderson and J.W. Miles. Surface-wave damping in a circular cylinder with a fixed contact line. *J. Fluid Mech.*, 275:285–299, 1994.

[40] E. Herbert, N. Mordant, and E. Falcon. Observation of the nonlinear dispersion relation and spatial statistics of wave turbulence on the surface of a fluid. *Phys. Rev. Lett.*, 105:144502, 2010.

[41] X. Hu, C.T. Chan, K.M. Ho, and J. Zi. Negative effective gravity in water waves by periodic resonator arrays. *Phys. Rev. Lett.*, 106:174501, 2011.

[42] H. Huehnerfuss, W. Alpers, W.L. Jones, P.A. Lange, and K. Richter. The damping of ocean surface waves by monomolecular film measured by wave staffs and microwave radars. *J. Geophysical Research*, 86:429–438, 1981.

[43] R. K. Ing, N. Etaix, A. Leblanc, and M. Fink. Measurement of thickness or plate velocity using ambient vibrations. *J. Acoust. Soc. Am.*, 127(6):EL252–257, 2000.

[44] P. Kosmas and C. Rappaport. Time reversal with the FDTD method for microwave breast cancer detection. *IEEE Trans. on Microwave Theory and Tech.*, 53(7):2317 –2323, 2005.

[45] G. Lagubeau, M.A. Fontelos, C. Josserand, A. Maurel, V. Pagneux, and P. Petitjeans. Flower patterns in drop impact on thin liquid films . *Phys. Rev. Lett.*, 105:184503, 2010.

[46] C. Larmat, J.-P. Montagner, M. Fink, Y. Capdeville, A. Tourin, and E. Clévédé. Time-reversal imaging of seismic sources and application to the great Sumatra earthquake. *Geophys. Reaserch Lett.*, 33:L19312, 2006.

[47] V.G. Levich. The damping of waves by surface active materials. *Acta Physicochim.*, 14:307–328, 1941.

[48] J. Lighthill. *Waves in fluids.* Cambridge University Press, Great Britain, 1978.

[49] G. Loresoy, J. de Rosny, A. Tourin, A. Derode, G. Montaldo, and M. Fink. Time Reversal of Electromagnetic Waves. *Phys. Rev. Lett.*, 92(19):193904, 2004.

[50] J. Lucassen. Longitudinal capillary waves. Part 1. - Theory. *Trans. Faraday Soc.*, 64:2221–2229, 1968.

[51] J. Lucassen. Effect of surface-active material on damping of gravity waves: a reappraisal. *J. Colloid Interface Sci.*, 85(1):52–58, 1982.

[52] J. Lucassen and R. Hansen. Damping of waves on monolayer-covered surfaces, I, Systems with Negligible Surface Dilational Viscosity. *J. Colloid Interface Sci.*, 22:32–44, 1966.

[53] J. Lucassen and M. van den Tempel. Longitudinal Waves on Visco-Elastic Surfaces. *J. Colloid Interface Sci.*, 41:491–498, 1972.

[54] S. Lukaschuk, S. Nazarenko, S. McLelland, and d P. Denissenko. Gravity Wave Turbulence in Wave Tanks: Space and Time Statistics. *Phys. Rev. Lett.*, 103:044501, 2009.

[55] S. Lukaschuk, S. Nazarenko, S. McLelland, and P. Denissenko. Statistics of surface gravity wave turbulence in the space and time domains. *J. Fluid Mech.*, 642:395–420, 2009.

[56] Y. Ma, G. Dong, M. Perlin, M. Ma A., X. Wang, and J. Xu. Laboratory observations of wave evolution, modulation and blocking due to spatially varying opposing currents. *J. Fluid Mech.*, 661: 108–429, 2010.

[57] C. Marangoni. Sul principio della viscosita superficiale dei liquidi stabili. *Nuovo Cimento, Ser. 2*, 5–6:239–276, 1872.

[58] A. Maurel, P. Cobelli, V. Pagneux, and P. Petitjeans. Experimental and theoretical inspection of the phase-to-height relation in Fourier transform profilometry. *Applied Optics*, 48(2):380–392, 2009.

[59] J. Miles. A note on surface films and surface waves. *Wave Motion*, 13:303–306, 1991.

[60] J.W. Miles. Surface-wave damping in closed basins. *Proceedings of the Royal Society of London. Series A, Mathematical and Physical Sciences*, 297(1451):459–475, 1967.

[61] N. C. Mitchell and M. L. Somers. Quantitative backscatter measurements with a long-range side-scan sonar. *IEEE J. Oceanic Engineering*, 14:368–374, 1989.

[62] A. C. Newell and B. Rumpf. Wave Turbulence. *Annu. Rev. Fluid Mech.*, 43:59–78, 2010.

[63] C. S. Ng and A. Bhattacharjee. Interaction of shear-Alfvn wave packets: implication for weak magnetohydrodynamic turbulence in astrophysical plasmas. *Astrophysical Journal*, 465:845, 1996.

[64] C. Palacios. *Water wave metamaterials*. Master Thesis: ESPCI ParisTech & Imperial College London, 2012.

[65] J. B. Pendry. Negative refraction makes a perfect lens. *Phys. Rev. Lett.*, 85:3966–3969, 2000.

[66] J. B. Pendry, D. Schurig, and D. R. Smith. Negative refraction makes a perfect lens. *Science*, 312: 1780–1782, 2006.

[67] D.H. Peregrine. Interaction of water waves and current. *Adv. Appl. Mech.*, 16:9–117, 1976.

[68] A. Przadka, B. Cabane, V. Pagneux, A. Maurel, and P. Petitjeans. Fourier Transform Profilometry for water waves: how to achieve clean water attenuation with diffusive reflection at the water surface? *Exp. Fluids*, 52(2):519–527, 2012.

[69] A. Przadka, S Feat, P. Petitjeans, V. Pagneux, A. Maurel, and M. Fink. Time-reversal of water waves. *accepted for publication in Phys. Rev. Lett.*, 2012.

[70] L. Shemer, K. Goulitski, and E. Kit. Evolution of wide-spectrum unidirectional wave groups in a tank: an experimental and numerical study. *Europ. J. Mech. B/Fl.*, 26:193, 2007.

[71] B. T. Taddese, J. Hart, T. M. Antonsen, E. Ott, and S. M. Anlage. Sensor based on extending the concept of fidelity to classical waves. *Appl. Phys. Lett.*, 95:114103, 2009.

[72] M. Takeda and K. Mutoh. Fourier transform profilometry for the automatic measurement of 3-D object shapes. *Applied Optics*, 22:3977–3982, 1983.

[73] M. Takeda, H. Ina, and S. Kobayashi. Fourier-transform method of fringe-pattern analysis for computer-based topography and interferometry. *Journal of the Optical Society of America*, 72(1): 156–160, 1982.

[74] A. Toffoli, M. Benoit, M. Onorato, and E.M. Bitner-Gregersen. The effect of third-order nonlinearity on statistical properties of random directional waves in finite depth. *Nonlinear Processes in Geophysics*, 16:131–139, 2009.

[75] A. Toffoli, L. Cavaleri, A.V. Babanin, M. Benoit, E.M. Bitner-Gregersen, J. Monbaliu, M. Onorato, A. R. Osborne, and C. T. Stansberg. Occurrence of extreme waves in three-dimensional mechanically generated wave fields propagating over an oblique current. *Natural Hazards and Earth System Sci.*, 11:895–903, 2011.

[76] W.B. Wright, R. Budakian, and S.J. Putterman. Diffusing light photography of fully developed isotropic ripple turbulence . *Phys. Rev. Lett.*, 76:4528–4531, 1996.

[77] F. Wu, J.L. Thomas, and M. Fink. Time Reversal of Ultrasonic Fields-Part II: Experimental Results. *IEEE Trans. Ulatrason. Ferroelectr. Freq. Control*, 39:567–578, 1992.

[78] V. E. Zakharov. Stability of periodic waves of finite amplitude on the surface of deep wate. *J. App. Mech. Tech. Phys.*, 2:190–194, 1968.

[79] V.E. Zakharov and N.N. Filonenko. Energy spectrum for stochastic oscillations of the surface of a liquid. *Sov. Phys. Dokl.*, 11:882–884, 1967.

[80] V.E. Zakharov and N.N. Filonenko. Weak turbulence of capillary waves. *J. App. Mech. Tech.*, 8: 37–42, 1967.

[81] V.E. Zakharov, V. L'vov, and G. Falkovich. *Kolmogorov Spectra of Turbulence I*. Berlin: Springer-Verlag, 1992.

[82] Q.-C. Zhang and X.-Y. Su. An optical measurement of vortex shape at a free surface . *Opt. Laser Technol.*, 34:107–113, 2002.

[83] X. Zhang and C.S. Cox. A novel technique for free-surface elevation mapping . *Phys. Fluids*, 6(9): s11, 1994.

[84] X. Zhang and C.S. Cox. Measuring the two-dimensional structure of a wavy water surface optically: a surface gradient detector. *Exp. Fluids*, 17:225–237, 1994.

Acknowledgments

First and foremost, I would like to express my sincere gratitude to my supervisors, Philippe Petitjeans, Vincent Pagneux and Agnès Maurel for their support, help and valuable guidance. Their sympathy, flexibility and professional approach contributed tremendously to my project. I am grateful for both our academic and personal discussions, which motivated me throughout my thesis. I would also like to thank Sophie Goujon-Durand for her invaluable assistance during my project. My gratitude goes to my colleagues from PMMH laboratory for their help and the pleasant atmosphere they created.

I am grateful to my friends, Vera Asvanyi, Guadalupe Couto, József Orbán, Robert Somogyi and Thomas Pujol for the happy and unforgettable time we shared together. I would also like to take this opportunity to thank my friends from Cité Universitaire, for being my surrogate family during the years I stayed there. Special thanks are extended to my polish friends for their understanding during my exile.

Lastly, none of this would have been possible without the love, patience and support of my wife Julia and my family.